

THE DIGITAL HADRON CALORIMETER: ANALYSIS OF THE NOVEMBER 2011 FERMILAB DATA

Benjamin Freund
Department of Physics
McGill University, Montreal
Quebec, Canada

July 2015

A thesis submitted to McGill University in partial fulfillment of the requirements of the
M.Sc. degree

©Benjamin Freund 2015

Acknowledgements

I would like to thank Burak Bilki for all his help to obtain the best simulations possible. Jose Repond was a huge help and provided much needed guidance for my research, without his help, this work would not have been possible. I would also like to thank my Supervisor Francois Corriveau who was always willing to help me and to provide feedback. Many thanks to Coralie Neubüser, who invested a lot of time proofreading this thesis. The most important person, who helped me complete this thesis, is with no doubt my beloved Cynthia Martel. She had to endure my stress and bad moods during the final stages of this thesis and was always there to encourage me to keep working.

Abstract

The future electron-positron International Linear Collider (ILC) is a high precision machine requiring high resolution detectors. It has a broad physics program covering topics such as precision measurements of the Higgs Boson and possible detection of Dark Matter or supersymmetric particles. New detector concepts have to be developed to meet the very stringent requirements. For optimised event reconstruction innovative Particle Flow algorithms will have to be applied to all detector systems. The international CALICE collaboration is developing highly granular calorimeter detectors for that purpose. Within this collaboration, several physical prototypes have been constructed, including a Digital Hadron Calorimeter (DHCAL) physical 1m^3 prototype, using the Resistive Plate Chamber technology, which is developed at Argonne National Laboratory. It is a high granularity sampling calorimeter with $1\times 1\text{ cm}^2$ digital read-out, making it the first digital imaging calorimeter ever. The DHCAL prototype was tested with different absorber materials, such as steel and tungsten, at different test beam facilities (Fermilab and CERN). Additionally in November 2011, data was taken without the additional absorber structures. Data collected with minimal absorber material provides unprecedented insight into the inner structure of both electromagnetic and hadronic showers. The data set is ideal for detailed comparisons with GEANT4 based simulations. This thesis presents a full detector analysis of electromagnetic and hadronic showers in the DHCAL without additional absorber plates. It includes calibration, event selection and particle identification. The single particle energy resolution and other parameters are compared to GEANT4 simulations and different hadronic models implemented in GEANT4 are validated against the data.

Abrégé

Le futur collisionneur linéaire international électron-positron (ILC) est un accélérateur de grande précision nécessitant des détecteurs de haute résolution. Son vaste programme de physique inclut par exemple des mesures précises des propriétés du boson de Higgs et d'éventuelles particules supersymétriques. Ainsi de nouveaux concepts de détection doivent être développés. Pour optimiser la reconstruction des événements, une approche basée sur le suivi de particules ("Particle Flow") doit être appliquée dans toutes les parties du détecteur. La collaboration internationale CALICE développe ces calorimètres à haute segmentation qui satisfont aux exigences de la résolution. Dans ce cadre, plusieurs prototypes ont été développés et construits, y compris un calorimètre hadronique digital (DHCAL) développé à Argonne National Laboratory, dont le volume est d'un mètre cube, utilisant des chambres à plaques résistives de verre en tant qu'élément sensible. C'est un calorimètre à échantillonnage de segmentation latérale d'un centimètre carré. Le DHCAL a été testé à plusieurs reprises dans des lignes de faisceaux de particules (Fermilab et CERN) avec différents matériaux d'absorption (acier et tungstène). En novembre 2011 des données ont été prises sans matériaux d'absorption supplémentaires. Ces données fournissent des détails sans précédent sur des cascades électromagnétiques et hadroniques et forment ainsi qu'une base idéale pour des comparaisons avec des simulations basées sur GEANT4. Dans ce mémoire une analyse complète de ces données est effectuée, incluant la calibration, la sélection d'événements et l'identification des particules. La résolution en énergie des particules ainsi que d'autres mesures sont comparées à des simulations. Pour conclure des modèles hadroniques implémentés dans GEANT4 ont été validés.

Contents

Acknowledgements	i
Abstract	ii
Abrégé	iii
1 Introduction	1
2 Theory	3
2.1 The Standard Model	3
2.1.1 Gauge Bosons	4
2.1.2 Fermions	4
2.2 Beyond the Standard Model	6
3 International Linear Collider	8
3.1 Overview	8
3.2 Accelerator Design	9
3.3 Physics at the ILC	10

3.4	Detectors	11
3.4.1	SiD detector	14
3.4.2	ILD Detector	15
4	Calorimetry	16
4.1	Interaction of Charged Particles with Matter	16
4.1.1	Energy Loss by Ionisation	17
4.1.2	Bremsstrahlung	18
4.1.3	Electron-Pair Production	19
4.2	Interaction of Photons	20
4.3	Hadronic Interactions	20
4.4	Electromagnetic Showers	21
4.5	Hadronic Showers	23
4.6	Calorimeters	24
4.7	Resolution	25
4.8	Imaging Calorimeter	25
4.9	Particle Flow Algorithm	26
4.10	Clustering	28
5	CALICE Detectors	29
5.1	Electromagnetic Calorimeter	29

5.2	Hadron Calorimeter	30
5.2.1	Analogue Hadron Calorimeter	31
5.2.2	Digital Hadron Calorimeter	31
6	DHCAL and Test Beam Set-up	33
6.1	Design of the DHCAL prototype	33
6.1.1	RPC Design	33
6.1.2	Readout Electronics and Cassette Structure	34
6.2	DHCAL with Minimal Absorber	35
6.3	Fermilab Test Beam Setup	36
7	Analysis	39
7.1	Collected Data	39
7.2	Hit and Event Selection	40
7.2.1	Noise Hits and Dead Chambers	40
7.2.2	Timing	41
7.2.3	Event Selection	42
7.3	Particle Identification	43
7.4	Calibration of the Min-DHCAL	49
7.4.1	Equalisation Procedure	49
7.4.2	Track Fits	51

7.4.3	Test of the Equalisation Procedure	52
7.5	Monte Carlo Simulation	54
7.6	Systematic Errors	57
8	Results	62
8.1	DHCAL Test Beam with Steel Absorber Structure	62
8.2	Results of the Min-DHCAL analysis	68
8.2.1	Response to Positrons	68
8.2.2	Linearisation of the Electromagnetic Response	80
8.2.3	Response to Muons	84
8.2.4	Response to Pions	88
9	Discussion and Conclusion	101
	Acronyms	108

Chapter 1

Introduction

Particle physics is a branch of physics that studies the nature of particles and their interactions. Different detectors are used to investigate the properties of particles. The energy of particles is measured with calorimeters, which are designed to completely stop the particles and measure the energy depositions in the detector.

This thesis presents an analysis of special data taken with the active layers of the Digital Hadron CALorimeter (DHCAL) prototype at the Fermilab Test Beam Facility. The DHCAL is developed at Argonne National Laboratory and was constructed as part of the CALICE efforts in developing calorimeter detector components for the proposed International Linear Collider (ILC).

A short introduction to the Standard Model of particle physics (SM) is presented in chapter 2. The model forms the theoretical framework of particle physics allowing accurate predictions for current and future particle physics experiments. Despite the huge success of the theory, open questions and some discrepancies between experimental data and theory predictions remain. The ILC will allow precision measurements of the Higgs Boson and other particles, which are not possible at the Large Hadron Collider due to large backgrounds. It is a complementary project which could fill gaps in the SM. A description of the proposed collider, with its two detectors ILD and SiD, is given in chapter 3.

In chapter 4 the particle interactions relevant for calorimetry are presented as well as

how these can be used to detect and measure a variety of particles. The DHCAL is only one sub-system of the proposed detector and enables the energy measurement of incident hadrons. Thanks to its extremely high granularity, the DHCAL is a so-called imaging calorimeter. Such detectors are specifically designed for the application of the Particle Flow Algorithms, which allows vast improvements in the energy resolution. Imaging calorimeters have many advantages over traditional calorimeters, which are also presented in this chapter.

The CALICE (CALorimeter for LInear Collider Experiment) collaboration is developing calorimeters for e^+e^- experiments at the TeV scale. This thesis is done in conjunction with this group. Different prototypes are developed by the collaboration for every calorimeter part of the detectors. A short description of the various prototypes is given in chapter 5.

The functioning of the DHCAL and the details of the physical prototype are presented in detail in chapter 6. This prototype collected special test beam data taken with minimal absorber structure at Fermilab in November 2011. My analysis is based on this data. Its details are presented in chapter 7 followed by the results in chapter 8. The response to positrons, muons and pions are investigated. The study includes resolution measurements and shower analysis, along with comparisons to Monte Carlo simulations. A discussion of the results and a conclusion can be found in chapter 9.

Chapter 2

Theory

The Standard Model of particle physics (SM) is an advanced and well tested theory describing the interaction of fundamental particles. It has been developed in the 1960s and 1970s and has been confirmed at an extraordinary level by numerous experiments, e.g. at the Large Electron-Positron Collider (LEP) or the Large Hadron Collider (LHC). This chapter is dedicated to this model which plays such a crucial role in particle physics.

2.1 The Standard Model

Effective field theories build the theoretical framework of the SM. Effective means that the SM is an accurate description of physics at the low-energy limit, but for high-energy processes, more fundamental theories are needed. The SM is a quantum field theory describing the behaviour of particles.

Existing fundamental particles can be grouped by their quantum numbers such as the spin. All non-gravitational experiments seem to be describable by particles with spins zero through one. Particles with half-integer spins are called *fermions* and particles with integer spins are called *bosons*.

2.1.1 Gauge Bosons

All interactions of particles are the results of four fundamental forces: the strong, weak, electromagnetic and gravitational force. The SM does not have a verified theory of gravity so only three of the four fundamental forces are treated here. The strong, weak and electromagnetic interactions arise due to the exchange of so-called gauge bosons. The spin-one particles associated with the strong force are called *gluons*. There are eight different gluons carrying the colour charge of the strong interaction. Any particle which couples to the gluons is strongly interacting. As the gluons are themselves carriers of the colour charge, they can self-interact. They are thought to be massless.

There are four spin one bosons associated with the next group. The weak interaction is mediated by three particles, the W^\pm and Z^0 . The W 's have unity charge whereas the Z^0 is charge neutral. The electromagnetic force is mediated by the photon. Both the electromagnetic and weak forces have been unified in a single force called the electroweak force [1].

In addition to the above mentioned bosons the SM predicts another boson, which has just recently been observed by both the ATLAS and CMS experiments, the so-called Higgs particle. The masses of quarks and leptons are generated by interaction with the Higgs field. Without the Higgs boson, all particles in the SM would be massless. An overview of the elementary particles with their properties can be found in Figure 2.1.

2.1.2 Fermions

Fermions are spin-half particles, they come in three generations. Each generation couples identically to the bosons, but in general, each is more massive than the previous one. Fermions are furthermore divided into two sectors: leptons and quarks. Six leptons are known: the electron e , the muon μ , the tau τ and three associated neutrinos: ν_e , ν_μ and ν_τ . Leptons are subject to all fundamental forces except the strong force. Neutrinos are very light and they do not carry any charge and therefore only interact via the weak force. For every fermion there exists a particle with the same mass but opposite quantum number, these particles are referred to as anti-particles.

2.2 Beyond the Standard Model

Even if the current SM can successfully describe most of all particle physics experiments, there are still observations where this model fails to provide a good explanation; e.g. neutrino oscillation. The SM predicts massless and stable neutrinos. Several experiments, for example experiments observing solar neutrinos, have shown however that neutrinos oscillate between flavours [3]. An oscillation would only be possible in the SM, assuming key aspects such as particle content or renormalisability still being valid, if the neutrinos were in fact not massless as predicted [4].

The concept of dark matter has been introduced to explain several cosmological observations, for example discrepancies between the mass of galaxy clusters determined by their gravitational effect compared to the visible mass [5]. However there is no dark matter candidate in the SM. Dark matter does not interact via the electromagnetic force, hence the name "dark" matter, however it interacts gravitationally. There are several theoretical models predicting particles which could play the role of dark matter, e.g. sterile neutrinos [6]. None of these models has been experimentally proven yet.

Current astronomical observations show that the expansion of the universe is accelerating. This can only be explained in the current model by including a non-zero vacuum energy in Einstein's gravitational field equations [7]. In principle this could be explained in the framework of the SM by a non-zero vacuum energy of scalar and fermionic fields [8]. But when doing the calculations the predictions differ from observations by some 122 orders of magnitude! This is the biggest discrepancy known between predictions and observations. Several models, for example Supersymmetry, try to address this problem by adding additional symmetries between bosons and fermions [9].

The SM is not able to unify the electro-weak and strong force with the gravitational force. It is expected that all SM gauge couplings take a common value at very high energies of the order of 10^{16} GeV and that all fundamental forces are just different manifestations of the same unified interaction [10]. This happens at the Planck scale. At this energy it is theorised that the gravitational force, which in general is very small compared to the other forces, will become as strong as the other SM interactions. Therefore at these energies the gravitational force has to be incorporated into the SM.

The SM has therefore evident shortcomings and is incomplete. It can at best be an effective theory describing particle physics below a few hundred GeV. These open questions are an important reason to construct new and more powerful colliders which could enable the detection of new particles and could in turn provide hints of a possibly more general theory.

Chapter 3

International Linear Collider

The International Linear Collider (ILC) is a proposed linear electron-positron collider, with a centre-of-mass energy between 200-500 GeV and is upgradable to 1 TeV. It is based on superconducting radiofrequency accelerating technology at a frequency of 1.3 GHz. The proposed luminosity for the 500 GeV runs is $1.8 \times 10^{34} \text{ cm}^{-2}\text{s}^{-1}$ [11].

3.1 Overview

All the specifications are taken from the Technical Design Report published in 2013 [11]. A layout of the accelerator and all its major sub-systems can be seen in figure 3.1.

The layout includes the following systems:

- a polarised electron source
- a polarised positron source obtained from electron-positron pairs converted from photons which are produced by passing the electron beam through an undulator
- a 5 GeV electron and positron damping ring with a circumference of 3.2 km
- beam transport and a two-staged bunch-compressor system

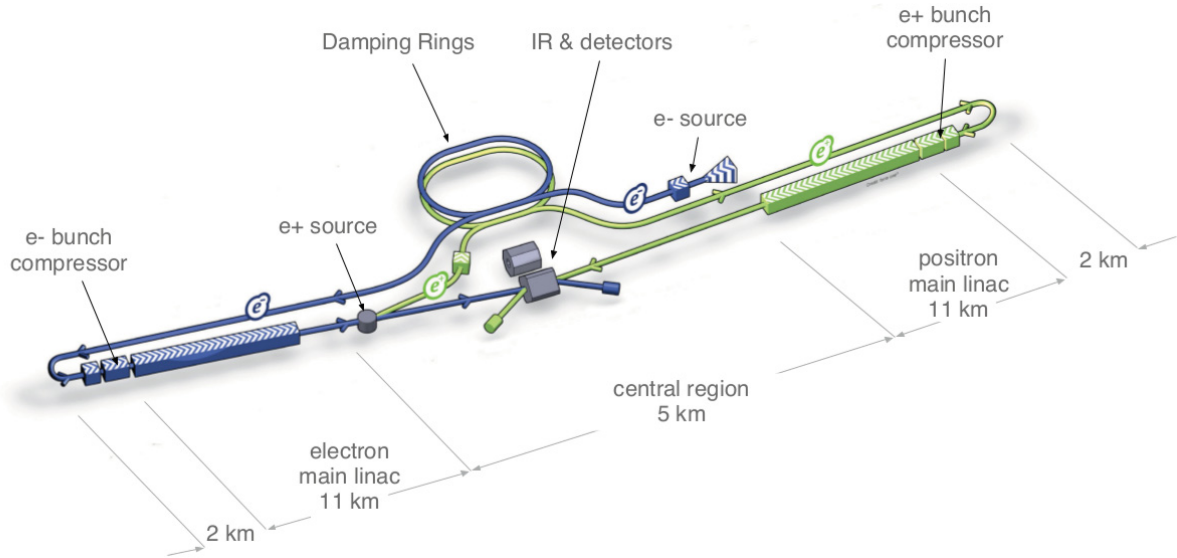


Figure 3.1: Schematic layout of the ILC. [11]

- two 11 km main A linear accelerator (LINAC) with 1.3 GHz SCRF cavities
- two beam-delivery systems, each 2.2 km long, bringing the beams into collision at a single interaction point which can be occupied by two detectors in a "push-pull" configuration

In total the accelerator would be approximately 31 km long.

3.2 Accelerator Design

In the main LINAC of the ILC, each beam will initially be accelerated from 15 GeV to a maximum achievable energy of 250 GeV. This is done with superconducting niobium cavities with an average accelerating gradient of 31.5 MV/m. These cavities are integrated in cryomodules which cool them with liquid helium. The cavities are modifications of existing modules currently used and developed at DESY for the FLASH accelerator and the European X-Ray FEL and have to be operated at 2 K.

3.3 Physics at the ILC

As described in chapter 2.2, despite the overwhelming success of the Standard Model, there are some gaps and inconsistencies to be analysed and discovered by studying the interactions of known and new particles. The most obvious gaps are the inability to include gravity in the Standard Model and the absence of candidates for the dark matter, strongly suggested by astronomic observations. The Higgs field and the quantum of this field, the Higgs Boson, play a crucial role in these questions, as any model of fundamental physics for high energies must include the Higgs field or its generalisation. The ILC was specifically designed to study the detailed properties of the Higgs Boson, for example the decay modes, branching ratios and cross sections, as well as the discovery of new particles which might be associated with it.

The initial program of the ILC will be performed at a center of mass energy of 250 GeV. 250 GeV is the peak cross section of a 125 GeV Higgs boson in the reaction $e^+e^- \rightarrow Zh$, allowing high precision measurements of the Higgs Boson. It is possible that the recently discovered particle by ATLAS and CMS is only one of several Higgs bosons. If a different boson makes contributions to the W and Z boson mass than it would be discovered at the ILC.

In a second stage the center of mass energy will be tuned to 500 GeV where the process $e^+e^- \rightarrow \nu\bar{\nu}h$ will be investigated. This will provide the normalisation of the Higgs coupling strength and the strength of the self-interaction. The ILC will constrain or discover new interactions at higher mass scales through the production of quarks, leptons, the W and Z bosons and the top quark. These measurements rely on efficient tagging of the W , Z and Higgs bosons as new particles will often decay via these bosons. This leads to demanding requirements for the detectors in the ILC, mainly a high energy-resolution and exceptional di-jet mass performance. The ILC will allow precision measurements of the top quark mass, to a level which can not be reached at a hadron collider due to the large background from hadronic interactions.

The ILC will also make important contributions to the fundamental questions mentioned above, e.g. the dark matter search and the discovery of new particles. It will either find or exclude new particles up to masses at least as high as the energy of ILC; this is in most cases not possible at the LHC, as electro-weak processes are completely shadowed by

the large strong-interaction background. An overview of the physics at the ILC can be seen in table 3.1.

ILC	Energy	Reaction	Physics Goal
Stage 1	91 GeV	$e^+e^- \rightarrow Z$	ultra-precision electroweak
	160 GeV	$e^+e^- \rightarrow WW$	ultra-precision W mass
	250 GeV	$e^+e^- \rightarrow Zh$	precision Higgs couplings
	350-400 GeV	$e^+e^- \rightarrow t\bar{t}$	top quark mass and couplings
$e^+e^- \rightarrow WW$		precision W couplings	
$e^+e^- \rightarrow v\bar{v}h$		precision Higgs couplings	
Stage 2	500 GeV	$e^+e^- \rightarrow f\bar{f}$	precision search for Z'
		$e^+e^- \rightarrow t\bar{t}h$	Higgs coupling to top
		$e^+e^- \rightarrow Zhh$	Higgs self-coupling
		$e^+e^- \rightarrow \tilde{\chi}\tilde{\chi}$	search for supersymmetry
		$e^+e^- \rightarrow AH, H^+H^-$	search for extended Higgs states
Stage 3	700-1000 GeV	$e^+e^- \rightarrow v\bar{v}h\bar{h}$	Higgs self-coupling
		$e^+e^- \rightarrow v\bar{v}VV$	composite Higgs sector
		$e^+e^- \rightarrow v\bar{v}t\bar{t}$	Composite Higgs and top
		$e^+e^- \rightarrow \tilde{t}\tilde{t}^*$	Composite Higgs and top

Table 3.1: Major physics processes to be studied by the ILC at various energies. [11]

The ILC is therefore an essential tool that could provide answers to the most fundamental problems in particle physics and the Standard Model.

3.4 Detectors

Both the rate and the complexity of events at an electron-positron collider are much lower than those of a proton-proton collider. This allows the development of particle detectors featuring higher resolution and higher granularity and to have less blocking material between the interaction point and the detector.

As mentioned in section 3.3 high-energy-resolution and di-jet mass performance are of high importance. A precision in the reconstruction of jets of 3 to 4 percent for 100 GeV jets is needed. To achieve this, techniques like Particle Flow Algorithm (PFA) (see 4.9) have been developed. PFA is currently used in other detectors like the Compact Muon Solenoid (CMS) [12]. In the case of the ILC however, detectors will be specifically optimised for the first time towards the application of this technique. The requirements on momentum resolution for charged particles will be of the order of $\frac{\Delta p}{p^2} \approx 5 \cdot 10^{-5}(\text{GeV}/c)^{-1}$, to enable e.g. the reconstruction of a Higgs boson recoiling from the Z boson decay in the Higgsstrahlung process. To meet the requirements, high granularity electromagnetic and hadronic calorimeters and high efficient tracking systems have to be developed. Particle identification is done in the highly granular calorimeters and muon identification is helped by the instrumented iron return yoke, used to contain the magnetic field in the detector.

The ILC will have one millisecond bunch trains arriving at a frequency of 5 Hz. This is a rather sparse filling compared to the Large Hadron Collider (LHC), allowing the detector systems to be switched off between bunch trains, in the so-called power pulsing operation. The power-pulsing will bring costs down by reducing the heat production and therefore the need for cooling inside of the detector.

The ILC is designed to have two experiments, the Silicon Detector (SiD) and International Large Detector (ILD) at the same interaction point using a so-called push and pull approach (see figure 3.2). Both detectors are multi-purpose detectors, optimised for the broad range of physics at the ILC. This is motivated by the experience of past collider experiments, where a two-detector design with complementary strengths allowed cross-checking, result confirmation and competition between collaborations enhanced scientific productivity. The push and pull operation allows great cost reductions compared to a set-up with two interaction points, where energy losses by Bremsstrahlung would be an issue.

The push-pull operation allows one to take data with one detector while doing maintenance on the other, at regular intervals the data-taking detector is pushed laterally and the other detector pulled into the interaction region. This should be done in the order of one day, to optimise the ILC integrated luminosity.

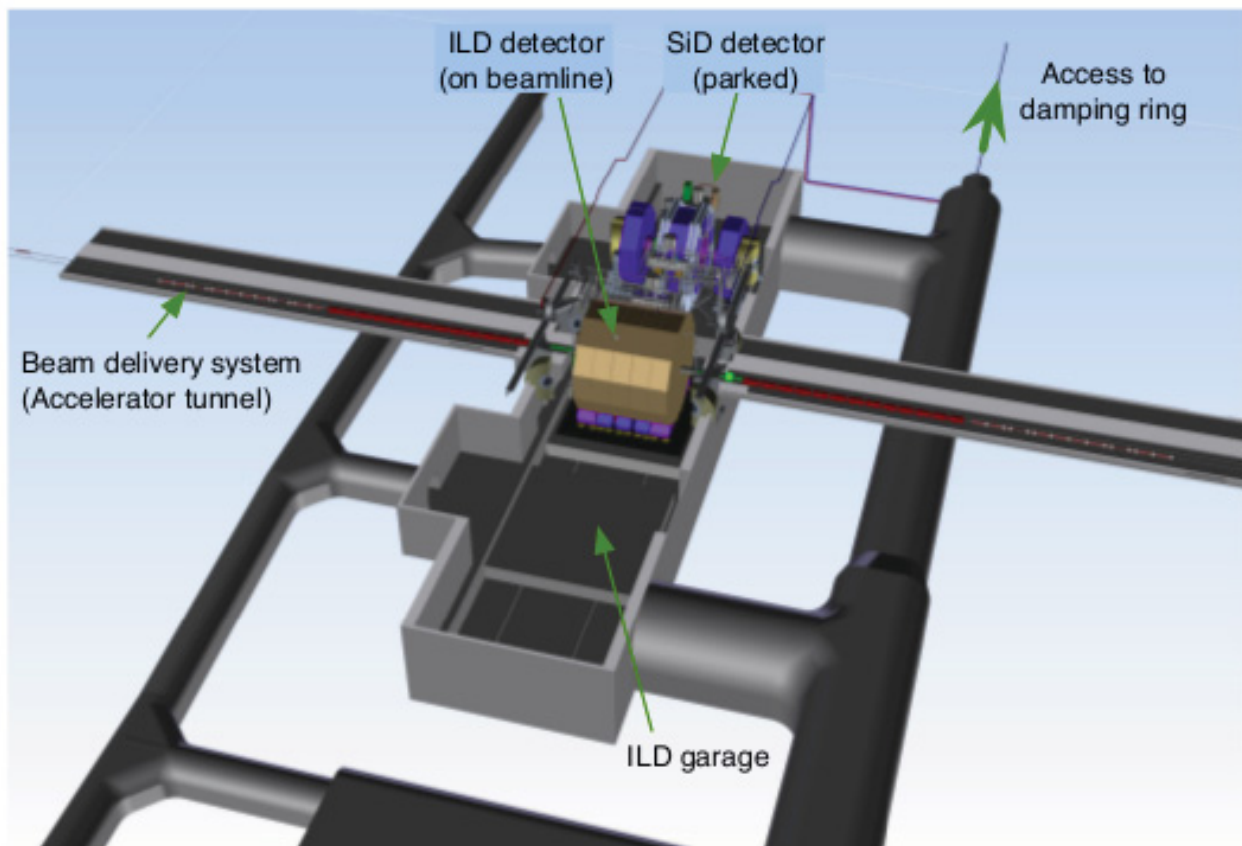


Figure 3.2: Schematic layout of the ILC. [11]

3.4.1 SiD detector

The SiD detector is a compact detector with a pixel vertex detector, silicon tracking, silicon-tungsten electromagnetic calorimeter, a highly granular hadronic calorimeter and a muon identification system. See figure 3.3 for a schematic view of the detector.

The tracking detector and calorimeters will operate in the power-pulsing mode and the calorimeters are optimised for jet-energy measurements using PFA. The vertex detector, which allows highly efficient tracking, uses a barrel and disk layout. It has 5 layers and a pixel size of $20 \times 20 \mu\text{m}^2$. The main tracker consists of silicon-strip sensors with an outer radius of 1.25 m and four layers in the endcap region.

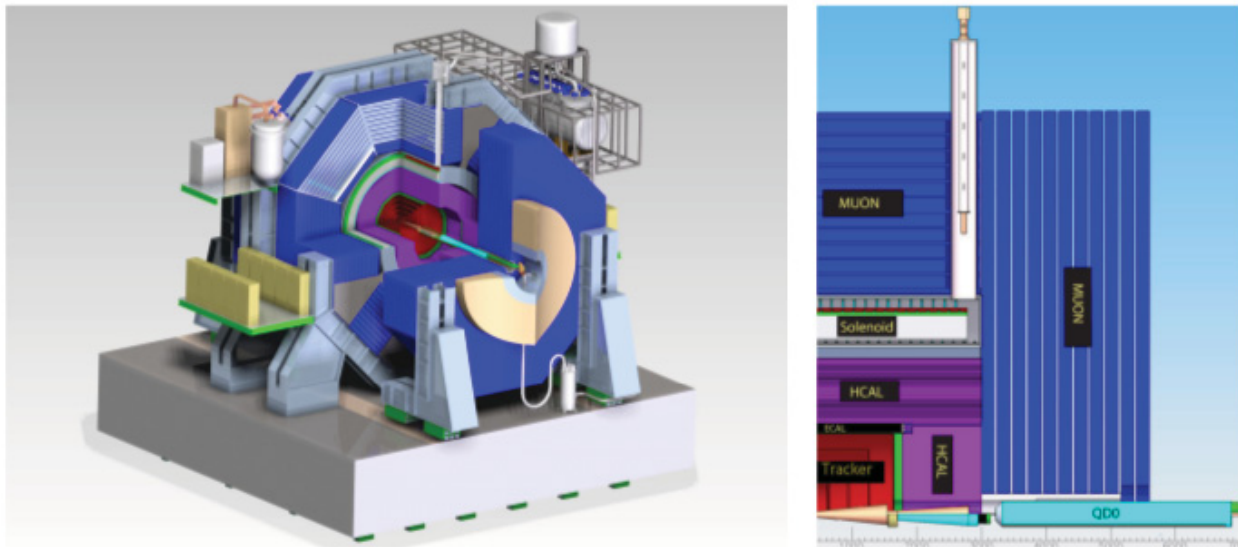


Figure 3.3: Schematic layout of the SiD detector showing the tracking in red, ECAL in green, HCAL in violet and the flux return in blue. [11]

The electromagnetic (ECAL) and hadronic calorimeter (HCAL) are both contained inside a central barrel inside of the superconducting solenoid producing a 5-Tesla magnetic field. The solenoid is based on the CMS solenoid design [13]. Outside of the solenoid is the muon system, it uses scintillator readout. Studies show that nine or more layers yield adequate energy measurement and enough muon-detection efficiency.

3.4.2 ILD Detector

The ILD is a multi-purpose detector with a vertex detector followed by a hybrid tracking system, a combination of a silicon tracking and a time-projection chamber (TPC), and a calorimeter system. An iron yoke serves as a muon system and a tail-catcher calorimeter. A sketch of the detector design can be seen in figure 3.4.

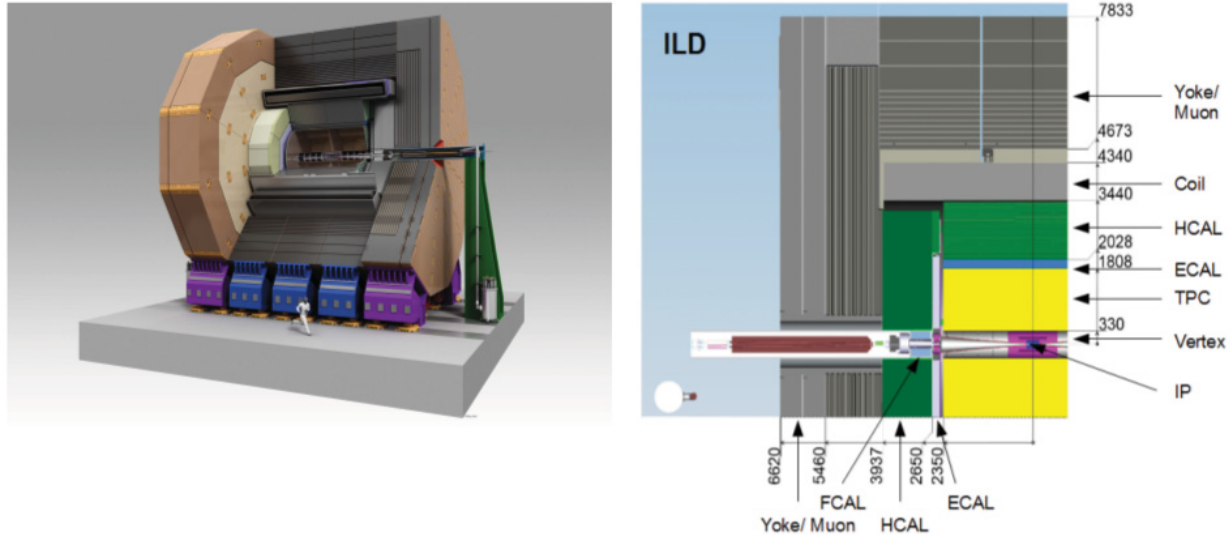


Figure 3.4: View of the ILD detector. [11]

The vertex detector has three layers of pixel detectors followed by two layers of silicon strips. The TPC [14] consists of two chambers filled with gas, with a high voltage applied across the length of the TPC. It will provide up to 224 points per track, providing 3-dimensional point resolution and particle identification capabilities.

The ECAL will have up to 30 layers with small cell size which is split into a barrel and an end-cap system. It is designed to be 20 cm thick with a radiation depth of $24 X_0$. Tungsten was chosen as the absorber. The HCAL will have up to 48 layers and a total nuclear interaction length of 5λ . Both analogue and digital readouts are considered. The detectors are contained in a 3.5 T magnetic field. An iron yoke returns the magnetic flux and is equipped with scintillator strips to serve as a muon detector. Canadian universities are involved in both the development of calorimeter as well as the tracking system of the detector.

Chapter 4

Calorimetry

A calorimeter is a device that measures energy depositions of a particle passing through the detector in order to determine its original energy. To know the energy of every particle in a collision is a requirement which is essential for event reconstruction.

There are two different types of calorimeter, *homogeneous calorimeters* and *sampling calorimeters*. Furthermore in many detectors the calorimeter is divided into an electromagnetic calorimeter, measuring in large part the energy of electrons and photons, and a hadronic calorimeter, measuring most of the energy of hadrons. In this chapter, first the interaction of particles and photons with matter is reviewed, followed by a description of the general principles of detection. The different types of calorimeters are discussed at the end of this chapter.

4.1 Interaction of Charged Particles with Matter

Particles and radiation are detected through their interaction with matter. The main processes used for measurements are ionisation, excitation and Bremsstrahlung especially for relativistic particles. Neutral particles can only be detected if they produce charged particles in an interaction, which are then detected via the mentioned interactions.

4.1.1 Energy Loss by Ionisation

When charged particles pass through matter, they ionise and excite atoms on their way. Excited atoms produce low energy photons, which are of great importance for many detectors recording this luminescence. The charged particles can also scatter from bound electrons in atoms. Energy is transferred from the charged particles to the electrons, which are liberated leaving an ionised atom behind. The average energy loss by ionisation and excitation can be approximated by the famous Bethe and Bloch formula [15], which calculates the average energy loss dE per length dx :

$$-\frac{dE}{dx} = 4\pi N_A r_e^2 m_e c^2 z^2 \frac{Z}{A} \frac{1}{\beta^2} \left(\ln \frac{2m_e c^2 \gamma^2 \beta^2}{I} - \beta^2 - \frac{\delta}{2} \right). \quad (4.1)$$

This equation has the following parameters:

z - charge of the incident particle

Z, A - atomic number and atomic weight of the absorber

M_E - electron mass

r_e - classical electron radius

N_A - Avogadro number

I - mean excitation energy

δ - is a parameter describing how much the transverse electric field of the incident relativistic particle is screened by the atomic electrons.

The energy loss is usually given in units of MeV/(g/cm²). This approximation is precise up to a few % up to energies of several hundred GeV, but is not a good description for particles with energies close to the binding energy of atomic electrons. In the low energy domain the energy loss decreases like $\frac{1}{\beta^2}$ as the incident particle energy increases and reaches a minimum near $\beta\gamma \approx 4$, as can be seen in figure 4.1 which shows the stopping power for positive muons in copper as a function of momentum. Particles which have an energy loss corresponding to this minimum are called *minimum – ionising particles* (MIPs). After this minimum the energy loss increases again, in the so-called relativistic rise.

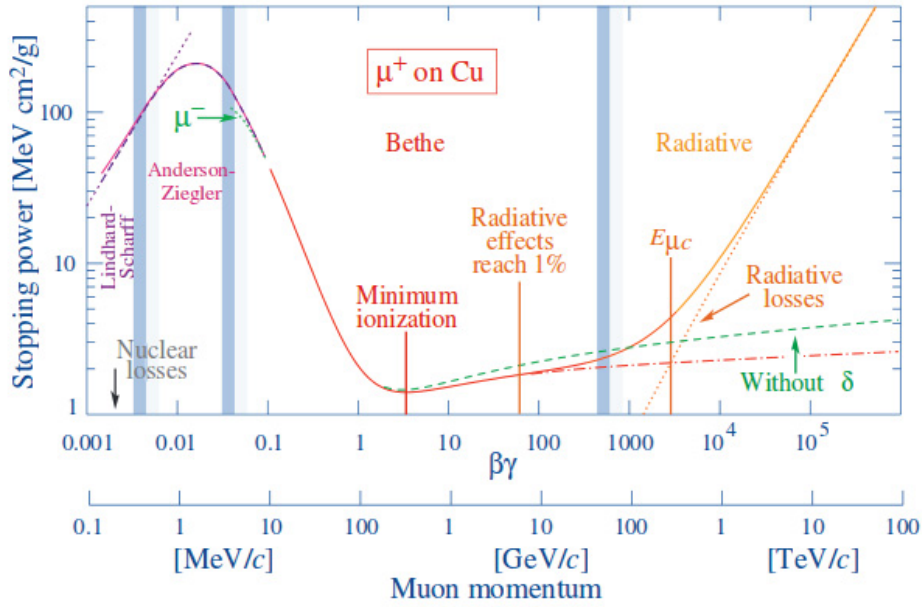


Figure 4.1: Stopping power for positive muons in copper as a function of momentum $p = M\beta c\gamma$, where M is the rest mass of the particle. [16]

4.1.2 Bremsstrahlung

In addition to their ionisation loss, fast charged particles lose energy by interacting with the Coulomb field of the nuclei of the traversed medium. Charged particles will decelerate and emit energy in form of photons (Bremsstrahlung). The energy loss by Bremsstrahlung for high energies can be described empirically by [15]:

$$-\left. \frac{dE}{dx} \right|_{\text{Brems.}} \approx 4\alpha \cdot N_A \cdot \frac{Z^2}{A} \cdot z^2 \left(\frac{1}{4\pi\epsilon_0} \cdot \frac{e^2}{mc^2} \right)^2 \cdot E \ln \frac{183}{Z^{1/3}} ; \quad (4.2)$$

where:

Z, A - atomic number and weight of the medium

z, m, E - charge, mass and energy of the incident particle.

The energy loss due to Bremsstrahlung is proportional to the particle energy and inversely proportional to the mass squared of the incident particle. Therefore due to the small electron mass, energy losses due to Bremsstrahlung dominates for highly energetic electrons. For electrons, equation 4.2 can be rewritten as:

$$-\left. \frac{dE}{dx} \right|_{\text{Brems. } e^-} = \frac{E}{X_0} . \quad (4.3)$$

In this equation X_0 is the radiation length which is a scaling unit defined as:

$$X_0 = \frac{A}{4\alpha N_A Z^2 r_e^2 \ln(183Z^{-1/3})}; \quad (4.4)$$

where Z and A are the atomic number and the atomic weight of the absorber. This length corresponds to the mean distance over which highly energetic electrons loses all but $\frac{1}{e}$ of its energy via Bremsstrahlung.

Equation 4.3 can be integrated which leads to

$$E = E_0 e^{-x/X_0} . \quad (4.5)$$

This function describes the exponential attenuation of the energy of charged particles by radiation losses.

Energy losses due to Bremsstrahlung are proportional to the energy whereas ionisation losses are proportional to the logarithm of the energy. The energy where both processes lead to equal energy losses is called the critical energy E_c .

4.1.3 Electron-Pair Production

Besides energy losses due to Bremsstrahlung and ionisation, pair production plays an important role for high energies. Electron-positron pairs can be produced by virtual photons in the proximity of the Coulomb field produced by nuclei. For muons, due to their greater mass compared to electrons, this energy loss is more important than Bremsstrahlung losses. The energy loss of charged particles is proportional to the energy and can be parametrised by [15]

$$-\left. \frac{dE}{dx} \right|_{\text{pair prod.}} = b_{\text{pair}}(Z, A, E) \cdot E . \quad (4.6)$$

The b_{pair} parameter varies only slowly with energy. As an example, the energy loss in iron due to pair production by 100 GeV muons can be described by

$$-\left. \frac{dE}{dx} \right|_{\text{pair prod.}} = 0.3 \frac{\text{MeV}}{\text{g/cm}^2} . \quad (4.7)$$

4.2 Interaction of Photons

Photons are detected indirectly by their interaction with the medium of the detector. When photons interact, they produce charged particles which are recorded by their ionisation of the active medium of the detector. In an interaction, a photon is either completely absorbed or scattered via the Compton Effect. As these are statistical processes, it is impossible to define a penetration range for photons. A photon beam attenuates exponentially in matter according to [15]:

$$I = I_0 e^{-\mu x} . \quad (4.8)$$

The mass attenuation coefficient μ is related to the cross section for the various interaction processes of the photon. At low energies ($E_\gamma < 100$ keV) the photoelectric effect dominates. For medium energies ($E_\gamma \approx 1$ MeV) the Compton effect dominates and at high energies ($E_\gamma \gg 1$ MeV) the pair production dominates.

4.3 Hadronic Interactions

Strong interactions of hadrons obviously play an important role for hadronic calorimeter. In most cases hadrons will interact inelastically, which produces secondary particles in

the collision. The quantity that describes the inelastic processes is the average interaction length λ_I , which describes the absorption of hadrons similar to the losses due to Bremsstrahlung (see equation 4.5) according to [15]:

$$N = N_0 e^{-x/\lambda_I} . \quad (4.9)$$

Here λ_I , also a scaling variable as X_0 (see equation 4.4), is defined as:

$$\lambda_I = \frac{A}{N_A \cdot \rho \cdot \sigma_{inel}} ; \quad (4.10)$$

where σ_{inel} is the inelastic part of the cross section and N_A is the Avogadro constant. Hadrons can also interact electromagnetically with the detector as described in the previous sections.

4.4 Electromagnetic Showers

For high energies above 100 MeV electrons lose their energy almost exclusively by Bremsstrahlung (see equation 4.3). The characteristics of an electromagnetic shower development can be understood in a simplified model. A sketch of this model can be found in figure 4.2.

In this model an incident photon with an energy of E_0 produces an $e^+ e^-$ pair after travelling one radiation length X_0 through the detector. Both the electron and the positron emit one photon after one radiation length through Bremsstrahlung. The energy is symmetrically shared between the particles at each step. This process is repeated as long as $E_0/N > E_c$, where N is the number of particles at depth t (in units of X_0):

$$N(t) = 2^t . \quad (4.11)$$

When the energy of the particles falls below E_c , ionisation for electrons and Compton and photoelectric effects for photons dominate. The position of the shower maximum in

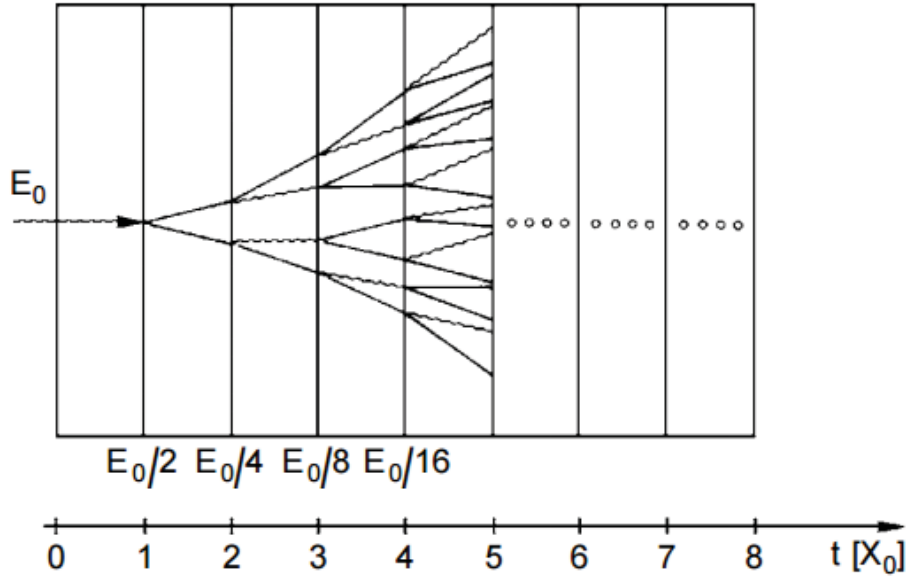


Figure 4.2: Sketch of a simple model for shower parametrisation. t is the depth and is given in units of X_0 . t is the depth in units of X_0 , the radiation length of the material. [17]

this model can be calculated as:

$$E_c = E_0 \cdot 2^{-t_{max}} . \quad (4.12)$$

This model, despite being overly simplified, is able to describe the most important characteristics of electromagnetic showers.

- Calorimeters need a thickness of about 10 to 15 X_0 to completely absorb an incident photon.
- The position of the shower maximum is logarithmically dependent on the energy.
- Leakage is mostly caused by soft photons escaping the detector.

In reality more complex shower models are needed. Monte Carlo simulations are used to give accurate descriptions. From these simulations an approximation of the longitudinal distribution of the energy deposition can be obtained. The so-called gamma distribution [18] provides a reasonable description,

$$\frac{dE}{dt} = E_0 \frac{\left(\frac{t-\mu}{\beta}\right)^{\gamma-1} e^{-\frac{t-\mu}{\beta}}}{\beta\Gamma(\alpha)} ; \quad (4.13)$$

where E_0 is the energy of the incident particle, Γ the Gamma function, γ a shape parameter, μ a location parameter related to the depth of the shower start, which shifts the distribution in t , and β a normalisation parameter. The shower maximum can then be obtained from the fit as

$$t_{max} = \gamma\beta - \beta + \mu . \quad (4.14)$$

The angular distribution is mainly determined by multiple scattering which can be best characterised by the Molière radius

$$R_M = \frac{21\text{MeV}}{E_c} X_0 . \quad (4.15)$$

95% of the shower energy is contained in a cylinder around the shower axis with a radius of $2R_M$, which is almost independent of the energy of the incident particle.

4.5 Hadronic Showers

When hadrons interact inelastically, a cascade of secondary particles is also produced. The description of hadronic showers is much more difficult than describing electromagnetic showers and no complete theory describing the development exists to date. The longitudinal development of an hadronic shower is described by the nuclear interaction length λ_I (see equation 4.10). In most detectors this quantity is much larger than the radiation length X_0 ; therefore hadronic calorimeters have to be significantly larger than electromagnetic calorimeters. Apart from the larger longitudinal extent, the lateral width of hadronic showers is also much larger. Instead of being determined by multiple scattering, the lateral size of hadron showers is dominated by large transverse energy transfers in nuclear interactions. The lateral distribution is initially very narrow but becomes wider

with increasing depth.

Secondary particles are produced by inelastic hadronic processes, mainly pions but also kaons and other hadrons. The average particle multiplicity depends logarithmically on the energy. A large fraction of the secondary particles are neutral pions, which in turn decay electromagnetically into two photons. These create electromagnetic subshowers inside the hadron showers.

In contrast to electromagnetic interactions where most of the energy can be recorded by the detector, hadronic showers have a substantial fraction of the energy remaining invisible, as part of the energy is used to break up nuclear bonds. Therefore a hadron signal in a calorimeter for the same particle is generally smaller than an electron signal, resulting in a ratio of electromagnetic over hadronic response larger than one ($\frac{e}{h} > 1$). Part of this invisible energy can be regained by equalising the response of electrons and hadrons. Calorimeters who achieve $e/h=1$ are called compensating calorimeter.

4.6 Calorimeters

As mentioned before, calorimeters can be divided into two categories, homogeneous and sampling calorimeters. In a homogeneous calorimeter the constituent material acts both as the absorber and as the active medium, in consequence basically the total volume of the detector is sensitive to the deposited energy. Measurements can be done by using scintillation light, ionisation or Cherenkov light. In general these kinds of calorimeters are characterised by a very good resolution but large volumes are needed as the effective absorption is generally very small compared to sampling calorimeters.

A more economical way to measure the energy is the deployment of a sampling calorimeter. This kind of detector has separate absorbing layers interspersed with sensitive layers measuring energy deposition. The absorber layers allow a more compact design, but the energy resolution is reduced as only a fraction of the energy deposition is measured. The energy resolution is affected by both energy-leakage and sampling fluctuations resulting in a worse energy resolution than for the homogeneous calorimeter. However for many experiments, due to cost and space requirements, sampling calorimeters are the only practical option.

In large collider experiments the calorimeters are usually divided into electromagnetic and hadronic calorimeters. As photons and electrons are stopped much earlier than hadrons, their energy is mostly measured in the electromagnetic calorimeter, featuring a good energy resolution. Hadronic showers pass through this first detector without losing much of their energy and their energy is mostly measured in the hadronic calorimeter, featuring in general thicker absorber plates.

4.7 Resolution

The quality of a detector is judged from its energy resolution, it is a measure of how precisely the energy of a given particle can be measured. The resolution is commonly approximated by the following parametrisation [19]:

$$\frac{\sigma_E}{E} = \frac{\alpha}{\sqrt{E}} \oplus \frac{b}{E} \oplus C ; \quad (4.16)$$

where α stands for the main stochastic term, b factorises the instrumental error and C is the constant term factorising calibration uncertainties. The letters were chosen to be consistent with previous published results [20]. The \oplus symbol means that the summation is in quadrature.

4.8 Imaging Calorimeter

Imaging calorimeters are calorimeters with high granularity. They are highly segmented both longitudinally and laterally. Such calorimeters therefore possess a large number of readout channels. The front-end electronics have to be placed directly on the surface of the active elements as there is not enough room to link all readout channels with the electronics via cables. Thus the readout is embedded in the calorimeter structure [21].

There are many possible candidates for imaging calorimeters; using for example silicon wafers, scintillator strips, Resistive Plate Chamber (RPC)s, Gas Electron Multipliers or

Micromegas as active medium.

Imaging calorimeters have several advantages over regular calorimeters, particularly for the application of the Particle Flow Algorithm (PFA), which is presented in the next section. Highly segmented calorimeters improve the measurements of individual hadronic jets. In multi-jet events energy deposits can be assigned to the reconstructed particles, leading to a better resolution on the mass of di-jets. Additionally the high segmentation allows particle identification inside the calorimeter.

Most sampling calorimeters are not compensating and have an electron over hadron ratio $\frac{e}{h} > 1$. In an imaging calorimeter, electromagnetic sub-showers can be identified in a hadron shower. The response can be compensated using so-called software compensation techniques thus improving the energy resolutions of single hadron events.

If particles are not completely stopped in the calorimeter, energy is leaking which degrades the energy resolution. Imaging calorimeters can use the detailed longitudinal shower information to correct for leakage and therefore further improve the energy resolution.

Imaging calorimeters give unprecedented insight into the spacial shape of hadronic showers. This can be used to validate hadronic shower models currently offered in Monte Carlo simulations like GEANT4.

4.9 Particle Flow Algorithm

In recent years imaging calorimeters have been developed for the ILC. These kind of detectors are optimised for the application of Particle Flow Algorithm (PFA) [22]. At the ILC many of the important physics processes will have multi-jet final states, accompanied by charged leptons and missing energies due to neutrinos. Precise mass reconstruction for multi-jets will allow much improved event reconstruction and identification. The goal is to reach an energy resolution sufficient to separate W and Z hadronic decay products.

In traditional calorimeters the jet energy is obtained from the sum of the energies deposited in the Electromagnetic CALorimeter (ECAL) and Hadronic CALorimeter (HCAL).

The resolution normally follows equation 4.16. For the hadronic calorimeter the stochastic term α is usually of the order 60 % and the constant term c is typically only a few per cent. For high energies there will be a contribution from energy leakage of the hadronic showers. To achieve the required energy resolution for multi-jets the stochastic term must be $\leq \frac{30\%}{\sqrt{E(\text{GeV})}}$, which is unlikely to be reached by the traditional approach [22].

Detailed measurements of jet fragmentation have shown that approximately 62 % of the jet energy is carried by charged particles, 27 % by photons, 10 % by neutral hadrons and 1 % by neutrinos [22]. Therefore around 70 % of the energy is measured in the HCAL, the detector with the worst energy resolution due to hadron shower fluctuations. Better resolution can be obtained by using a new kind of approach: the Particle Flow, which has already been successfully demonstrated by experiments like ALEPH and CMS.

Component	Detector	Energy Fraction	Energy Resolution	Jet-energy Resolution
Charged Particles (X^\pm)	Tracker	$\approx E_j$	$10^{-4} E_{X^\pm}^2$	$< 3.6 \cdot 10^{-5} E_j^2$
Photons (γ)	ECAL	$\approx 0.3 E_j$	$0.15 \sqrt{E_\gamma}$	$0.08 \sqrt{E_j}$
Neutral Hadrons (h^0)	HCAL	$\approx 0.1 E_j$	$0.60 \sqrt{E_\gamma}$	$0.17 \sqrt{E_j}$

Table 4.1: Contributions from the different particle components to the jet-energy resolution (in GeV). The table lists the approximate fractions of charged particles, photons and neutral hadrons in a jet of energy and the assumed single particle energy resolution. Whereas the tracker measures the momentum, for highly relativistic energies this is equivalent to the energy. [22]

The Particle Flow approach is believed to be the most promising candidate to reach the energy resolution goal at the ILC [23]. Calorimetry using this approach requires reconstructed four-vectors of all visible particles and the reconstructed jet-energy is the sum of the energies of the individual particles. The momenta of charged particles are measured in the tracker, energy of photons is measured in the ECAL and only the energy of neutral hadrons is measured mostly in the HCAL. Table 4.1 list the contributions to the energy resolutions for the different particles, assuming they have been correctly identified in the detector. This would result in a jet-energy resolution of $0.19/\sqrt{E(\text{GeV})}$ by combining the jet-energy contributions of the different detectors [22]. This level of performance cannot be achieved in practice, as it is not possible to always associate the energy deposit with the correct particle. This uncertainty is called 'confusion' and constitutes the limiting factor in detectors optimised for Particle Flow. The event reconstruction is done by a complex

pattern recognition software, the PFA. The Pandora PFA was developed to study Particle Flow calorimetry at the ILC, it is the best developed and sophisticated PFA to date [22].

4.10 Clustering

Clustering plays an important role in imaging calorimeter, it allows to associate hits with different particles in a same event. This is not only important for calibration but can be used furthermore for software compensation and particle identification. The algorithm used in this analysis is called nearest-neighbour algorithm; if two hits share a common side, they are assigned to the same cluster. For every cluster the simple mean x and mean y positions are calculated. The process is illustrated in figure 4.3.

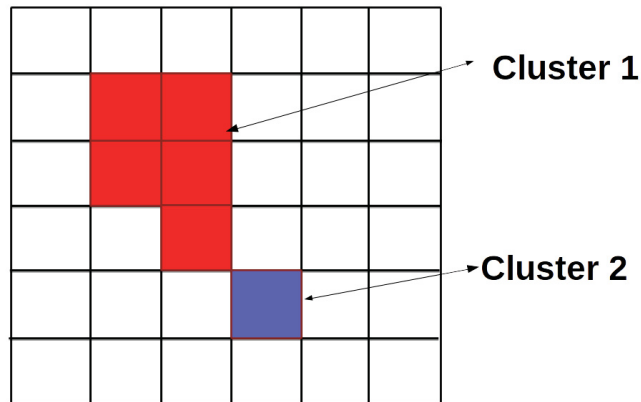


Figure 4.3: Schema of the clustering algorithm. Here the first cluster has 5 hits which share a common edge and a second cluster with only one hit.

Chapter 5

CALICE Detectors

The CALorimeter for LInear Collider Experiment (CALICE) collaboration is developing calorimeters for e^+e^- experiments at the TeV scale [24]. The collaboration consists of scientists and engineers from 57 institutes in 17 countries around the world. The detectors are optimised for Particle Flow Algorithm (see section 4.9). Therefore they have a high granularity. This is possible due to the low event rate at the ILC. CALICE is involved in the development of detectors that meet the performance requirements discussed in section 3.4, for all systems of a particle physics detector. CALICE has developed several prototypes to test and prove different concepts through test beams and simulations both for the SiD and ILD detectors [25]. Prototypes have been developed for the main subsystems of the detector: the ECAL and HCAL. The readout systems of the prototypes are either analogue, digital (1-bit), where a single threshold is applied, or semi-digital, featuring a 2-bits readout.

5.1 Electromagnetic Calorimeter

Several prototypes have been constructed by the collaboration. The Silicon Tungsten Electromagnetic CALorimeter (SiW ECAL) is a sampling calorimeter prototype based on tungsten absorber and silicon sensors. It was constructed and tested between 2006 and 2008. It uses silicon diode wafers as the active detector with pad sizes of $1 \times 1 \text{ cm}^2$ and an active area of $18 \times 18 \text{ cm}^2$ [26]. The physics prototype consists of 30 layers. The

prototype produced promising results, a nearly linear response to positrons was observed and a very good energy resolution was recorded for electrons, with a stochastic term a of $16.5 \pm 0.5\%$ and a small constant term c (see equation 4.16) [27]. A second prototype is currently being developed which aims to address issues connected with construction of a full detector, e.g. implemented front-end electronics and power pulsed readout.

Apart from the SiW ECAL, another prototype was constructed, a scintillator strip-based electromagnetic calorimeter (ScECAL), consisting of 26 layers of tungsten absorber plates interleaved with planes of $45 \times 10 \times 3 \text{ mm}^3$ plastic scintillator strips [28]. Such an ECAL has a smaller cost than alternative technologies using silicon sensors. Each layer features two rows of 9 scintillator strips. Scintillator layers are placed in two alternating orientations, with horizontally and vertically aligned strips. Each strip is individually read out by a Multi Pixel Photon Counter. A first ScECAL prototype consisting of 468 channels was constructed and then tested in February and March 2007 [28]. Similar to the SiW ECAL the ScECAL features a linear response and a stochastic term of 13 to 14% [28]. The physics prototype did not feature implemented front-end electronics and a non-uniform response of the strips was observed in the test beam. These issues will be addressed in a second prototype.

Yet another concept for the electromagnetic calorimeter is proposed by the CALICE MAPS group: the TeraPixel Active Calorimeter using Monolithic Active Pixel Sensors (MAPS) [29]. The size of a MAPS pixel is smaller by a factor of hundred compared to the proposed pad size of the SiW-ECAL. Therefore the number of pixels is highly increased and the MAPS detector would be operated as a digital detector, not recording energy but individual hits. No physical prototype has been constructed yet. The readout of the enormous number of readout channels of a full scale detector could be problematic.

5.2 Hadron Calorimeter

All hadron calorimeters will either use steel or tungsten as absorber.

5.2.1 Analogue Hadron Calorimeter

A physical prototype of the Analogue Hadron Calorimeter (AHCAL) was constructed in the years 2006 to 2007 [30]. The AHCAL prototype is a 38 layer sampling calorimeter. As the HCAL will be operated inside the magnet, the detector have to be operational in magnetic field and to be as small as possible to minimise the space. The AHCAL uses small scintillator pads, where traditional photomultiplier tubes (PMTs) are not an option. Instead Silicon Photomultipliers (SiPMs) are used, which operate in Geiger mode. They are constituted of around 1000 to 10,000 microcells and provide an analogue signal, which is proportional to the number of microcells fired. SiPM are operational in magnetic fields and have a gain of around 10^6 , similar to a standard PMT. The same readout is used for the ScECAL detector. However for SiPM the applied voltage is much lower which results in a lower energy consumption and less heating. The AHCAL prototype has 8,000 readout channels. The hadronic energy resolution of the AHCAL was measured to $\frac{58\%}{\sqrt{E/\text{GeV}}}$, with a constant term of 1.6% [31].

5.2.2 Digital Hadron Calorimeter

The DHCAL prototype was constructed in 2009-2010, after successful tests of a smaller prototype. The active media consist of Resistive Plate Chambers (RPCs) with digital readout. The prototype is discussed in greater detail in the following chapter. Digital calorimeters experience saturation effects due to the digital readout, as only hits are measured and not the actual energy deposition. This leads to a degraded energy resolution for higher energies. Advantages of the analogue readout are the low cost of the RPC technology and easier calibration than in the case of SiPM readout.

Besides the Digital Hadron Calorimeter there are also other digital or semi-digital hadronic calorimeter prototypes, such as the semi-digital (SDHCAL) or MICROME GAS (Micro-Mesh Gaseous Structure) DHCAL. The SDHCAL features the same RPC technology but with semi-digital [32] readout. It has 48 active layers with steel absorber plates with a total of 440,000 readout channels. The semi-digital readout hopes to reduce the effect of saturation by using multiple thresholds for the readout. First results show that a multiple threshold readout could improve the resolution over a single threshold readout [32]. Several MICROME GAS DHCAL chambers with 1 cm^2 pads featuring a digital readout

have been developed [33]. One advantage is the low voltage needed compared to RPCs (500 V compared to ≈ 3500 V). However the noise rate could be problematic and a larger prototype is needed to judge the performance of the detector.

Chapter 6

DHCAL and Test Beam Set-up

6.1 Design of the DHCAL prototype

The Digital Hadron CALorimeter (DHCAL) uses Resistive Plate Chambers (RPCs) as active elements. The design and functioning of the RPCs is explained below.

6.1.1 RPC Design

RPCs are widely used in calorimetry. Their advantages include a simple and robust design, reliability and low cost [34]. Several designs of the RPC have been developed, the one used in the DHCAL prototype can be seen in figure 6.1. The chamber has two soda-lime glass plates, coated with high surface resistivity paint. The glass plates serve as resistive plates enclosing a 1.15 mm thick gas gap. The area of each RPC, measures $32 \times 96 \text{ cm}^2$ [35]. The cathode and anode plates are 1.15 and 0.8 mm thick respectively. The cathode is chosen to be thicker to enhance the readout signal. The chambers are flushed using a mixture of three gases: tetrafluoroethane (94.5%), isobutane (5.0%) and sulfur hexafluoride (0.5%). The gas mixture was chosen to give a large avalanche signal and quick replenish time. Fishing lines run parallel to the long side of the RPC and are used as gas barriers and to keep the plates parallel. The fishing lines have a casing, with a diameter of 1.15 mm, which runs the entire length but leaves a 5 cm gap to allow gas to

flow through. The RPCs are operated in avalanche mode. An avalanche is initialised by a charged particle ionising the molecules in the gas gap. The free electrons are then accelerated by a high voltage applied across the chamber. The electrons then ionise more electrons on their way. The default high voltage is 6.3 kV.

Besides the standard 2-glassRPC, a different design featuring only one soda lime glass [36] was tested and showed promising results. The advantages include a lower multiplicity [37] and better rate capabilities. However this design is not used in the DHCAL prototype.

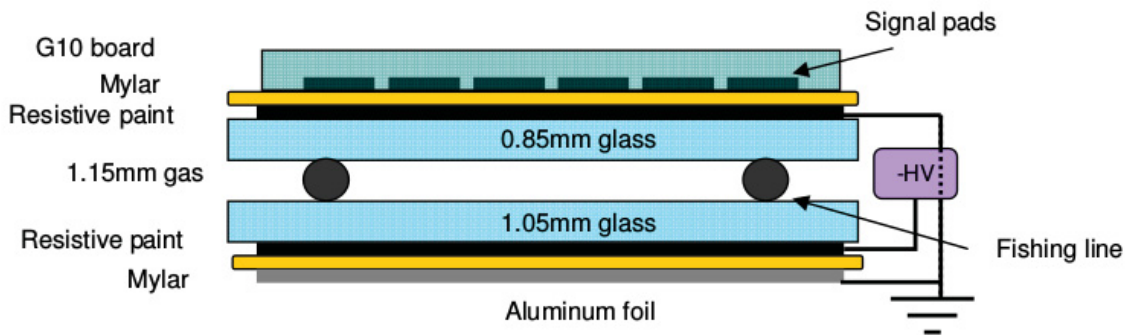


Figure 6.1: Design of the RPCs used in the DHCAL [38].

6.1.2 Readout Electronics and Cassette Structure

The Front-end Electronic Boards (FEB) measures $32 \times 48 \text{ cm}^2$ and therefore contains 1536 $1 \times 1 \text{ cm}^2$ pads. Two boards are used to cover the area of one chamber. Each FEB has 24 application-specific integrated circuits (ASICs), the DCAL III chip [39], providing a single threshold (=1-bit) to the signal from each pad. The threshold can be set individually for each chip, but was set common to all. The Data Acquisition System takes the signals from the RPCs and sends them to a computer. The readout is pulsed with a 10 MHz clock, providing a 100 ns time resolution.

Three RPCs and their six corresponding readout boards are assembled into one cassette to serve as one active layer of the calorimeter. The resulting active area of a cassette is approximately $96 \times 96 \text{ cm}^2$. Each cassette further features a 2 mm copper front-plate and a 2 mm steel rear plate. The whole structure is held together by rectangular bars located on the top and bottom of the structure.

6.2 DHCAL with Minimal Absorber

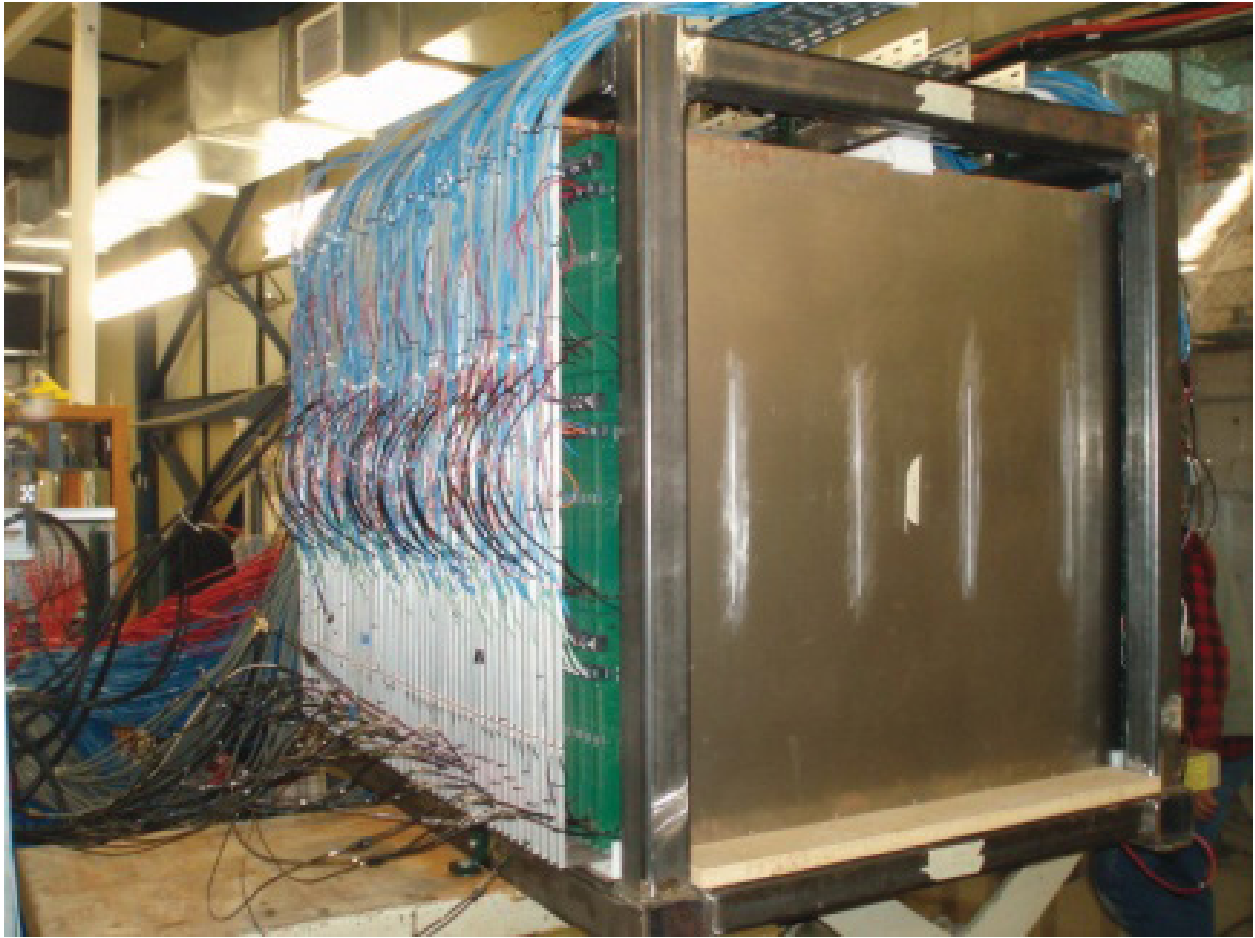


Figure 6.2: The Min-DHCAL at the FTBF in November 2011. [41]

Usually the DHCAL is used as sampling calorimeter. Between every layer there is either a steel or tungsten absorber, which acts as passive material to reduce the particle energies and to induce electromagnetic or hadronic showers. In November 2011 data was taken without additional absorber material interleaved between the cassettes, so that the only absorption comes from the cassettes themselves. The thickness of each cassette was about 12.5 mm, which corresponds to an average of 0.41 radiation length X_0 or 0.037 nuclear interaction lengths λ_I . Each readout chip had a 1.4 mm plastic casing. Plastic has a radiation length of ≈ 30 cm, therefore 1.4 mm of plastic corresponds to 0.004 X_0 or $\frac{1}{100}$ th of one active layer. These inhomogeneities were neglected in the simulation. In this minimal absorber configuration the DHCAL consisted of 50 cassettes each spaced 2.54 cm apart. The total number of readout channels was 460,800, which at the time constituted a world record for calorimetry in High Energy Physics. Figure 6.2 shows a

photograph of the DHCAL with Minimal absorber (Min-DHCAL).

The total thickness of the detector in the DHCAL with Minimal absorber (Min-DHCAL) configuration is $\approx 210 \frac{\text{g}}{\text{cm}^2}$, including the glass, the steel and the copper plates of the cassettes. With a 1 cm steel absorber plate between every layer (see section 8.1) the total thickness of the detector is $\approx 600 \frac{\text{g}}{\text{cm}^2}$. A 1 GeV muon stops in $\approx 565 \frac{\text{g}}{\text{cm}^2}$ [16]. Therefore we can see that a 1 GeV muon will not be stopped in the minimal absorber configuration, while it will be in the configuration with absorber plates.

6.3 Fermilab Test Beam Setup

Data was collected at the Fermilab Test Beam Facility (FTBF) [40]. The facility provides a 120 GeV proton beam and momentum selected secondary beams with energies ranging from 1 to 66 GeV. The secondary beam is a mixture of electrons/positrons, muons and pions. In figure 6.4 a view of the test beam set-up and the DHCAL prototype at the FTBF can be seen. Particles are kept according to their momenta. The main beam is surrounded by a halo consisting of mostly muons with slightly deviating momenta. Electrons are dominant for energies below 5 GeV and taper off above 32 GeV. Pions on the other hand constitute only a small fraction of the beam particles for low energies and dominate the beam above 32 GeV. Muons are present at all beam energies with varying fractions from run to run. Muons are produced in pion decays and constituted most of the particles found in the halo of the beam. Dedicated muon runs are produced by putting a large absorber target in front of the detector effectively stopping positrons and pions so that only muons arrive at the detector. In addition the beam is defocused so that the muon tracks cover the whole detector. Particles arrive in spills with a duration of 4 seconds every minute.

The three gases used in the RPCs (see section 6.1.1) are mixed on site by a custom made gas mixer. The mixed gas is then sent to a gas distribution system. The system has 28 channels which can be individually controlled, typically each channel is split in two to supply gas to two layers. The adjustable flow rate can be used to compensate for the few leaking RPCs.

A sketch of the set-up can be seen in figure 6.3. The set-up include two scintillator

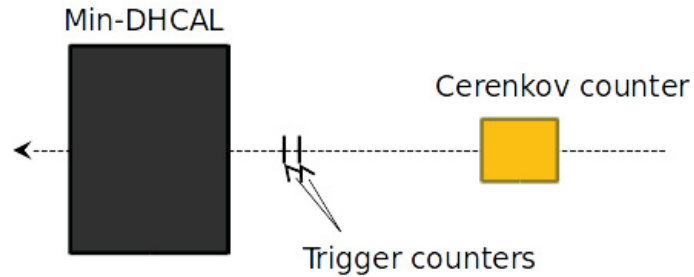


Figure 6.3: Sketch of the test beam set-up including the trigger and the Cherenkov counter.

plates which serve as a trigger and two Cherenkov counters in front of the DHCAL. One Cherenkov counter is used as a muon tagger, however it was not working during the test beam. The information of the Cherenkov counters is integrated into the datastream by the Data Acquisition System (DAQ). The DAQ system can either run in a self-triggered or external-triggered mode. The self-triggered mode was used to record so-called 'noise runs', otherwise for the test beam the scintillators were used as an external trigger. The Cherenkov information is stored in the event header line.

The data taken at the test beam facility is stored in a tuples format, a ordered list of numbers, which contains the timestamp, x, y and z information of all pads that fired in an event. The timestamp, which is in units of 100 ns, is assigned by the trigger and the Timing Module [43]. The x and y coordinates (integers) refer to the pad number in the x and y dimension and the z coordinate refers to the layer in which the pad fired. All hits occurring inside a window of seven time bins are combined into the same event. Further details will be provided in section 7.2.2.



Figure 6.4: View of the test beam set-up at the FTBF [42].

Chapter 7

Analysis

This analysis is done with test beam data taken with the DHCAL with Minimal absorber (Min-DHCAL) (see section 6.2). In this chapter the structure of my analysis is presented. It is done in several steps. First "good" runs, meaning stable beam conditions and a working Cherenkov counter, are identified and the event and hit selection criteria are applied. By studying for example the timing information of the hits, a large fraction of noise hits can be identified and removed from data. As the test beam at Fermilab consists of a mixture of different particles, offline Particle IDentification (PID) has to be done. An equalisation of the response of the detector is done using through-going muons. The equalisation procedure is presented and the efficiency of the equalisation is tested. Results of the analysis with the Min-DHCAL will be presented in the following chapter.

7.1 Collected Data

The Min-DHCAL was exposed to the test beam at the Fermilab Test Beam Facility. This analysis is based on the data collected in November 2011. Runs were taken within a selected momentum range of 1 - 10 GeV/c. In total 814,000 events were recorded, the number of events as a function of the momentum is shown in Table 7.1.

Momentum [GeV/c]	Number of events
1	107k
2	117k
3	62k
4	84k
6	109k
8	109k
10	226k
Total	814k

Table 7.1: Number of events recorded as a function of the momentum for the November 2011 data set.

7.2 Hit and Event Selection

The data files contain not only hits produced by particles interacting with the sensitive detector volume but also noise hits. In this section the procedure of how noise hits are identified and removed is presented, which enables detailed comparisons to simulation.

7.2.1 Noise Hits and Dead Chambers

In some events hits with identical coordinates but different timestamps were recorded. It is very unlikely that these so-called double hits are produced by particles interacting multiple times with the same cell, more probably this kind of hits results from the same interaction, but are recorded several times in the data due to the readout process. These double hits are identified and only counted once.

In between data taking runs, data were collected in trigger-less mode to monitor the status of the detector. During these so-called 'noise runs' it was observed that chambers close to the ground lead tend to fire at a relatively high rate. The ground lead was located at a vertical edge of each RPC. However for the November 2011 period, only a negligible amount of hits was recorded in these areas, corresponding to only 0.02% of the hits

recorded in an event. Nevertheless to reduce the contamination from these hits, any hit in an area of $2 \times 5 \text{ cm}^2$ surrounding the connectors was excluded from both data and simulation. This resulted also in a negligible loss of hits for the simulation, as these areas are far away from the particle beam.

In the Min-DHCAL a small fraction of the ASICs were dead and did not record any hits. No correction was applied to the data but in order to match the Monte Carlo to data, these dead ASICs are identified and all hits produced in the corresponding areas are removed from simulation. Only dead ASICs located in the centre of a layer will cause a significant loss of hits, as most of the hits are recorded here. Only one layer for 6 GeV and above feature a dead ASIC in such a location.

7.2.2 Timing

As explained in section 6.3, hits are recorded in seven consecutive time-bins, each 100 ns long. These time-bins have a time difference of 15 to 21 time-bins to the trigger timestamp. The trigger is processed after the recording of the hits, therefore hits with large time difference to the trigger correspond to hits recorded early in the event. In the following analysis these time-bins will be referred to by their corresponding time difference, hence the 15 to 21 time-bins.

The timing information is used to identify some of the noise hits. Therefore the time-bins containing hits produced by interactions of beam particles with the detector have to be identified. These time-bins will be characterised by a high number of hits compared to the others. A relativistic particle will pass through the detector in $\approx 3 \text{ ns}$, which is small compared to the 100 ns timing resolution. The shower development is therefore not resolved and in most cases all hits of a shower will be recorded in the same time-bin.

Histograms are created showing the number of hits versus the time difference to the trigger. One example of the timing information of all hits in a 10 GeV run can be seen in the left plot of figure 7.1, which is representative for all runs. Most hits are recorded in only two of the 7 time-bins, time-bins 19 and 20. It is assumed that only hits in these time-bins are produced by the particle that triggered the event, whereas the time-bin 21 contains hits recorded before particles entered the detector and the time-bins 15-18 correspond to hits

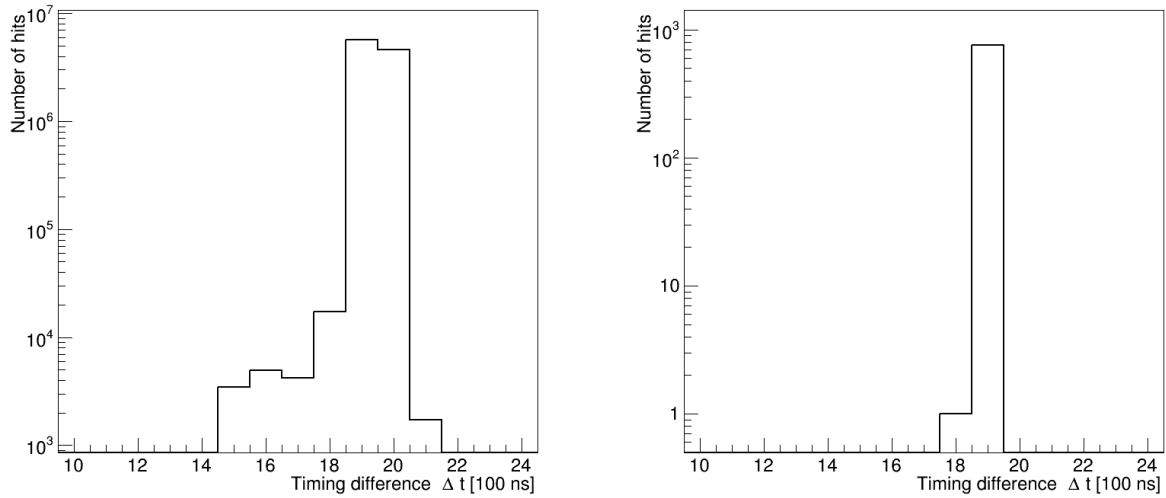


Figure 7.1: The left plot shows the timing information of all hits in a 10 GeV run taken during the November 2011 beam runs at Fermilab [41] and the right plot shows the timing information of a typical positron event the same run.

recorded after the particles left the detector. These hits will be produced nearly exclusively by electronic noise or by multiple particles events, which have not been already eliminated by the requirement on the first layer. As an example, the right plot of figure 7.1 shows the timing information of a typical 10 GeV positron event. All hits except one are recorded in the time-bin 19, the one recorded in time-bin 18 is most probably a noise hit. Therefore all hits not recorded in the 19 and 20 time-bin are removed from the data.

7.2.3 Event Selection

The event selection requires at least five layers with hits in order to eliminate events triggered by noise. The hits are clustered using a nearest-neighbour algorithm (see section 4.10). It is required that every event has exactly one cluster with no more than 4 hits in the first layer. This cut eliminates multiple particle events and events with particles which began showering before entering the detector. Both cases lead to either a large number of hits or several identified clusters in the first layer. In total, this cut removes approximately 10-20 % of the events in the data and less than 3% in simulation.

A small fraction of the events feature most of their hits outside of the two time-bins 19

and 20. An event display is used to analyse these kind of events. One example of an event, where most hits were recorded in the time-bin 21, can be seen in figure 7.2. In this event two distinct tracks can be identified, which are most likely produced by muons. Muons leave straight tracks in the detector as they interact little with the detector material. As these two muons traversed the detector in a narrow time frame they are both stored in the same event. Each track feature a distinct time difference corresponding to the time when the muon passed the detector, one track features hits in the 21 time-bin and one in the 19 time-bin. In this kind of double or multiple particles events, the time-bin with the most hits can correspond to either of these particles. This explains why these kind of events have most of their hits outside the 19 and 20 time-bin. Most of the multiple particle events are excluded with the requirement on the first layer, however if the tracks are very close together they will not be detected. So the timing information can reduce the fraction of multiple particles even further.

In figure 7.3 an event is displayed which had its maximum in the 15 time-bin. This event contains only a few hits with no visible tracks, therefore this is most probably an event triggered by noise and not by a beam particle. Most of the events in the 15-18 time-bin are such events and are therefore removed.

The fraction of events surviving the selection cuts is summarised in table 7.2.

7.3 Particle Identification

The test beam at Fermilab consists of a mixture of muons, positrons and pions, thus making Particle IDentification (PID) necessary. The PID was done offline using the Cherenkov signal and the concept of an interaction layer.

An interaction layer marks the beginning of an electromagnetic or hadronic shower. The interaction layer will therefore be characterised by a sudden increase in the observed number of hits. In this analysis an interaction layer is defined as being the first layer in a pair of two consecutive layers with four or more hits. At the given energies, muons can be considered as minimum ionising particles which will produce straight and narrow tracks in the detector. Muons are identified in this analysis by requiring at least 35 layers with at least one hit, and without an identified interaction layer.

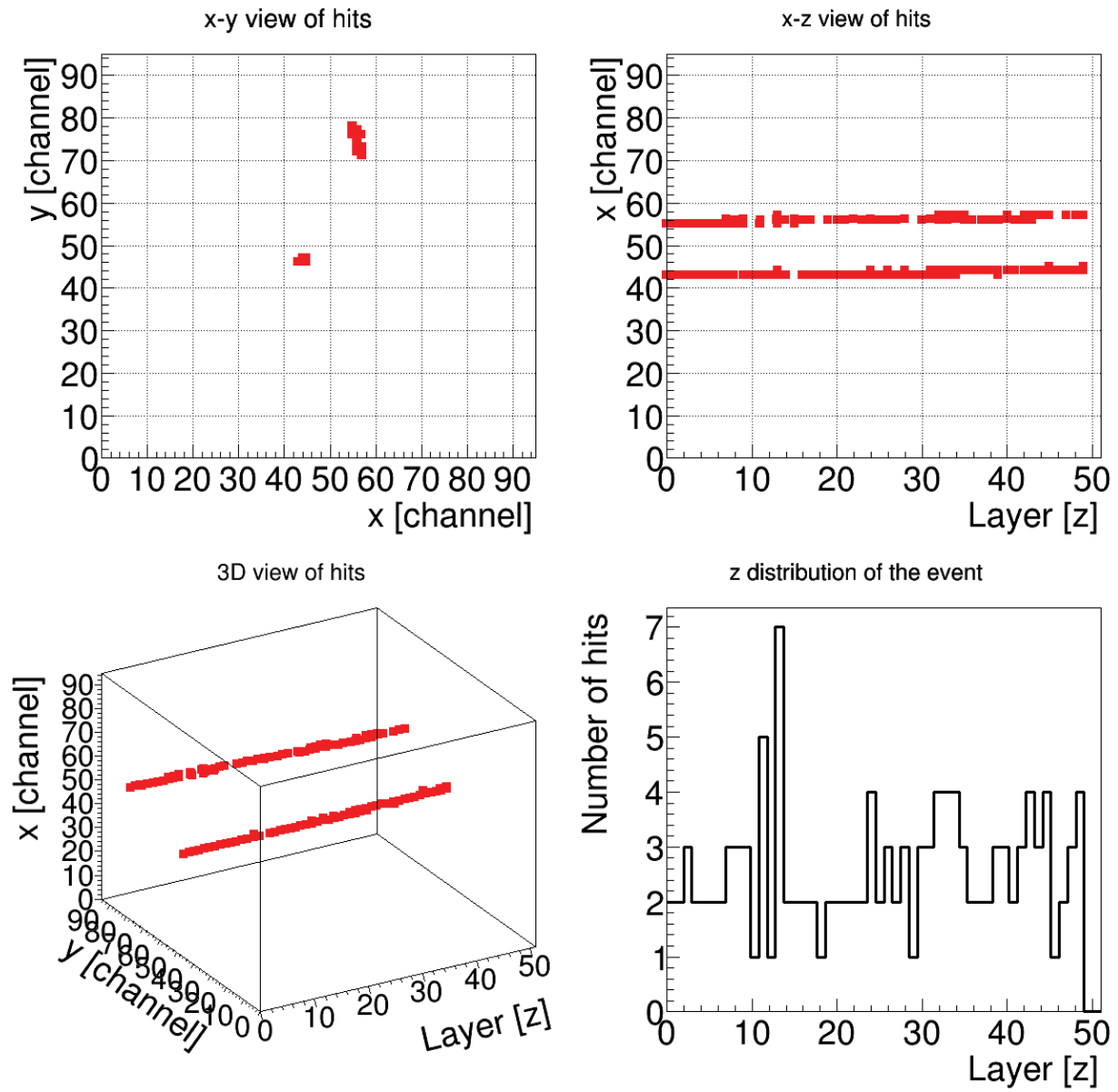


Figure 7.2: Event Display which shows the 2D and 3D distribution of hits for an event recording most of the hits in the 21 time-bin.

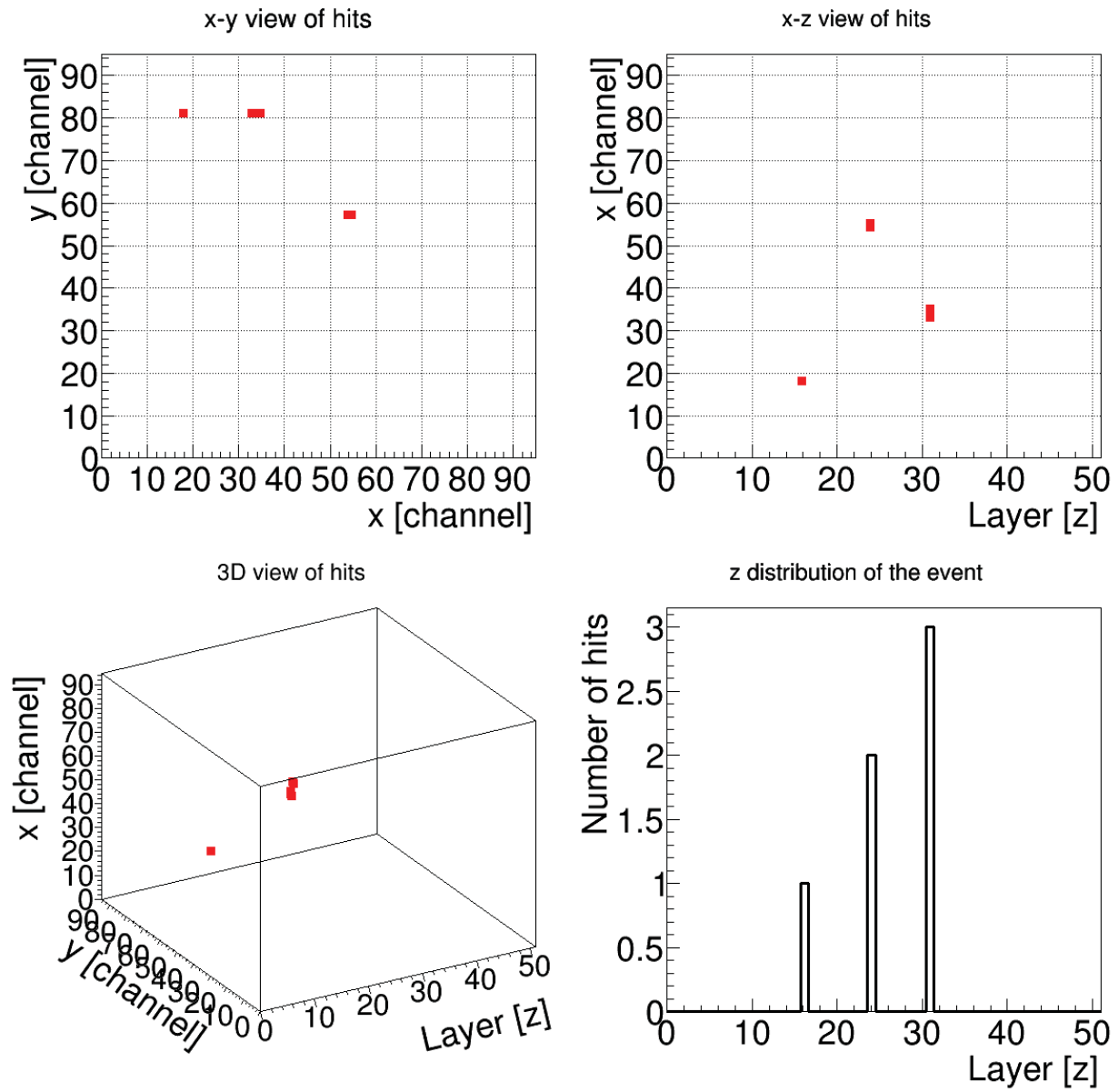


Figure 7.3: Event Display which shows the 2D and 3D distribution of hits for an event which had the most hits in the 15 time-bin.

Momentum [GeV/c]	Cut	1	2	3	4	6	8	10
Data	Timing cuts	99.9	99.8	99.9	99.8	99.95	99.95	99.6
	Requirements on first layer	88.5	87.0	80.3	80.3	88.1	86.65	88.2
	More than 5 active layers	88.1	86.4	80.0	79.8	88.0	86.5	88.1
Simulation	Timing cuts	100	100	100	100	100	100	100
	Requirements on first layer	98.3	97.9	97.9	97.9	97.6	97.2	96.8
	More than 5 active layers	98.3	97.9	97.9	97.6	97.2	97.1	96.

Table 7.2: Percentage of events surviving the various event selection criteria for data and positron simulation.

As pions have a significantly larger mass than positrons, pions and positrons can be easily distinguished in the Cherenkov counter. Positrons are selected by simply requiring a Cherenkov signal. Pions however are required to have no Cherenkov signal and to have an interaction layer. Most pion showers are not entirely contained inside the detector. The leakage is reduced by selecting only pions which start their shower early, therefore requiring the interaction layer to be in the first 10 layers. The majority of positrons start their electromagnetic shower in the first 5 layers. To reduce positron contamination in the pion sample, for events where the Cherenkov is not working, the position of the interaction layer of pions is required to be in layer 5 or later. However, for positron events where the Cherenkov signal is not working, 30 to 40% of the events will be identified as pions. This estimation is based on the positron simulation. Therefore it is important to only select runs where the Cherenkov counter is working efficiently.

In table 7.3 the percentage of particles, that survive the selection cuts, are given for both data and simulation. Nearly all positrons survive the selection cuts, however only 60 to 70% of the muons are selected in the simulation. This is due to the fact that muons can produce enough hits in two consecutive layers to be mistaken for an interaction layer, so only those muons are selected which do not interact much with the detector. The majority

Momentum [GeV/c]	Selected as	1	2	3	4	6	8	10
Data	Positrons	60.3	31.7	40.0	30.7	53.0	41.7	33.0
	Pions	0.2	0.6	0.9	1.2	4.7	5.5	7.2
	Muons	5.1	30.4	17.4	27.5	8.6	11.9	15.4
Positron simulation	Positrons	98.3	97.8	97.9	97.6	97.2	97.1	96.8
Pion simulation	Pions	8.1	12.7	15.4	16.1	17.5	17.7	17.7
	Muons	23.3	21.0	18.1	16.1	14.3	14.8	14.5
Muon simulation	Pions	1.3	1.0	1.7	0.7	0.4	1.3	0.6
	Muons	72.0	65.7	63.4	62.5	61.1	59.5	59.0

Table 7.3: Percentage of events selected as positrons, pions and muons for both data and simulation assuming an efficient Cherenkov counter. For the pion (muon) simulations the fraction of particles misidentified as muon (pion) is given.

of low energy pions (with a momentum below 4 GeV) do not feature an interaction layer. For these energies only a small fraction of pions will be selected. With the requirement to have an interaction layer in layer 5-10 only 10 to 20% of the events are selected in the pion simulation. The pion data sample will therefore suffer from poor statistics for low energies, especially as the beam is dominated by positrons below 5 GeV. The shower analysis of pions will be restricted to energies between 3-10 GeV. Additionally a high fraction of events in the pion simulation will be selected as muons, resulting in a confusion between muons and pions. This is not really problematic as pions without an interaction layer are basically indistinguishable from muons.

To reduce the muon contamination in the pion sample an additional cut is applied. This cut uses the average number of hits per layer, defined as the number of hits divided by the number of active layers. Figure 7.4 shows the average number of hits for both muons and pions for a 10 GeV run. The muons produce few hits per layer and a narrow distribution whereas the pion distribution is broad. By requiring an event to have at least 2.8 hits on average per active layer to be selected as a 10 GeV pion, the muon contamination in the pion sample is reduced considerably (see table 7.3).

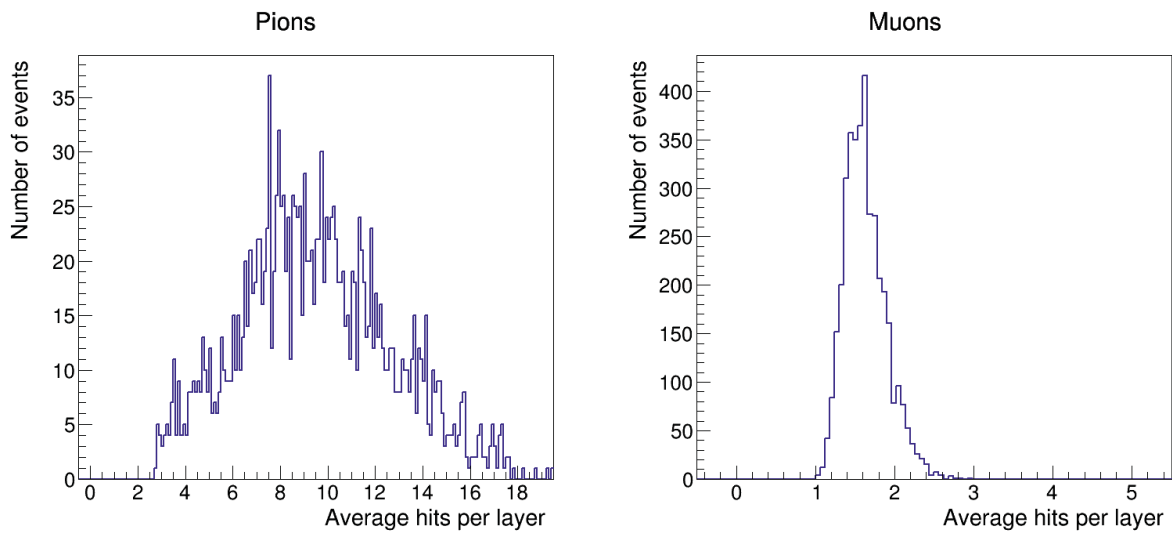


Figure 7.4: The number of hits divided by the number of active layers for both muons (left) and pions (right) for a 10 GeV run after applying the selection cut described in the text.

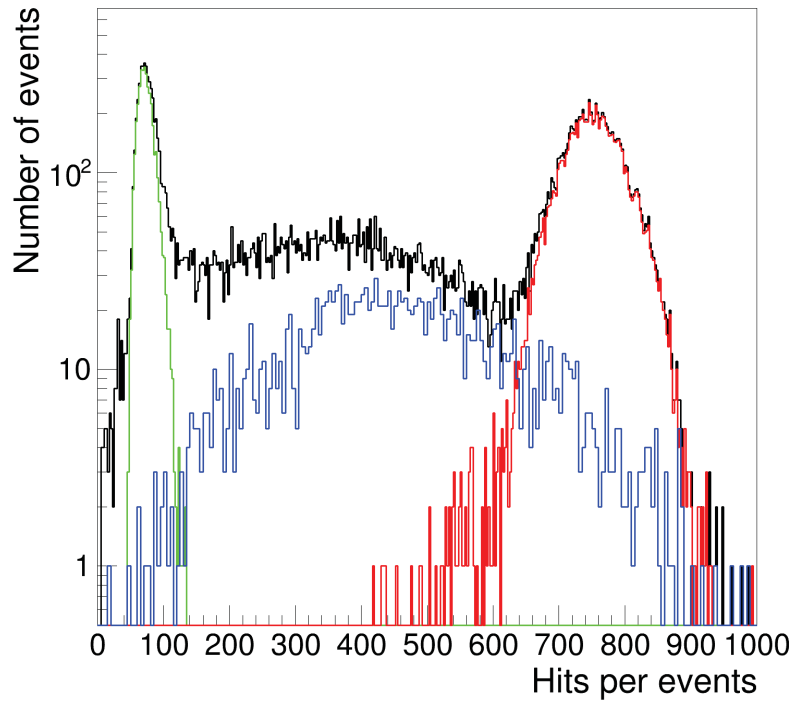


Figure 7.5: Hit distributions for a 10 GeV run. The sum of all event types are shown in black, selected muon events in green, pions in blue and positrons in red.

In figure 7.5 the described cuts are applied to the hit distribution to test the performance of the cuts. As seen the particles are very effectively separated and the hit distributions take their expected form. Muons produce the least hits and a very narrow distribution. Pions have a very large distribution corresponding to the fact that they interact both electromagnetically and hadronically, associated with large fluctuations in the deposited energy. Positrons interact only electromagnetically, they produce dense electromagnetic showers in the detector, therefore producing many hits and a narrow distribution.

7.4 Calibration of the Min-DHCAL

The RPC response depends on factors such as the applied voltage, atmospheric pressure, humidity and temperature during data recording [44]. As the data runs covered several days, environmental conditions and therefore the response were subject to change. In addition the temperature was not homogeneous over the entire stack, resulting in layer by layer variations. Two temperature sensors were put in two different locations inside the detector to monitor the temperature. A one degree average difference between the two was observed and an RMS value of 1.2 degree was recorded for both. The distributions of the temperature of both sensors can be found in figure 7.6. To equalise the response, track fits of through going muons from the runs themselves as well as muons from dedicated muon runs are performed to equalise the response of the 150 RPCs. The procedure itself is presented and a test of the performance is shown.

7.4.1 Equalisation Procedure

The equalisation is done in so-called clean regions as defined in [45]. Clean regions exclude areas near dead or hot cells, cells in line with the fishing lines or cells within one centrimetre along the edges of the RPC. Only the clean regions are used for equalisation as they are supposed to feature a uniform response. Dead cells are removed from data and simulation and the efficiencies at the edge of the detector are correctly reproduced by the simulation, therefore the other areas can be ignored for the equalisation procedure.

To equalise the response of every RPC i , the average pad multiplicity μ_i and efficiency

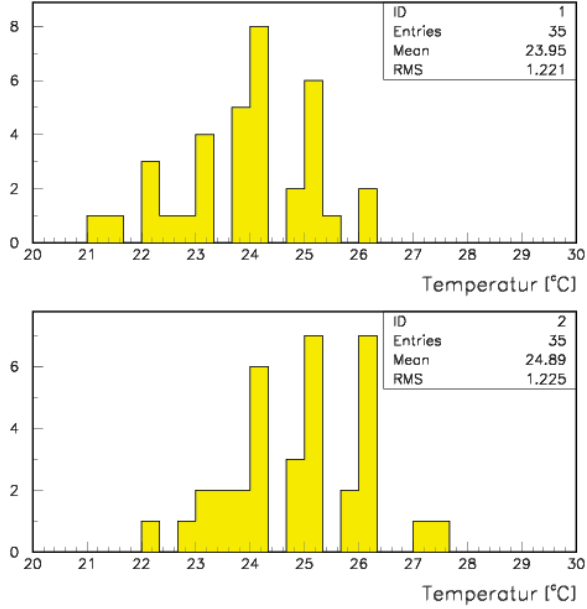


Figure 7.6: Recorded temperature of two sensors located in the detector during the November 2011 test beam.

ϵ_i to MIP-like particles is calculated using so-called track fits. The efficiency ϵ is defined as the ratio of tracks producing at least one hit to the total number of identified tracks. The pad multiplicity μ corresponds to the average number of hits recorded for tracks which generate at least one hit in that chamber. The exact procedure of how track fits are performed is explained in the next section. Once the average pad multiplicity μ_i and efficiency ϵ_i are calculated for every RPC i and every run, the calibration factor c_i is simply defined as:

$$c_i = \frac{\mu_0 \epsilon_0}{\mu_i \epsilon_i} ; \quad (7.1)$$

where μ_0 and ϵ_0 are the averages over all RPCs and all runs in a period. In the Novem-

ber 2011 period the mean efficiency ϵ_0 was 0.92 and the mean multiplicity μ_0 was 1.6 after the application of cleaning cuts described below.

Once all the calibration factors c_i are obtained for all individual RPCs, the corrected number of hits N' is given as the sum of the hits N_i recorded in RPC i times the corresponding calibration factor c_i

$$N' = \sum_{i=0}^{149} N_i \cdot c_i . \quad (7.2)$$

7.4.2 Track Fits

The track fits method uses muons from both the runs themselves as well as muons from dedicated muon runs recorded close to the run under study. To obtain the calibration factors, clusters from each event which are laterally within a distance of 3 cm of each other in different layers are grouped together. Clean muon tracks are required for calibration, therefore if two consecutive layers have more than 4 hits the track is not used for efficiency and multiplicity extraction. Furthermore, tracks are required to go through the whole detector, therefore a cluster is required in each of the first three and last three layers. In addition, none of the layers may contain more than one cluster of hits. The slope of the track is limited to at most 0.5 pads per layer, both horizontally and vertically. Typically 5-10% of the events survive these cuts.

The group of clusters is fitted to a 3D line. In every layer a cluster is then searched within 2 cm of the predicted position. If a cluster is found the multiplicity is the number of hits found in this cluster. Otherwise the layer is counted as inefficient.

In addition to using track fits it is possible to do fits of track segments in hadronic showers. This allows an in situ calibration without taking dedicated calibration runs with muons. More sophisticated equalisation procedures are currently being developed to solve shortcomings of the two methods described here. Details of these alternative methods, for example a calibration based on the density information of hits, can be found in [45].

7.4.3 Test of the Equalisation Procedure

To see if the described equalisation is actually working, several tests are performed. First the normalisation of the calibration is tested. The distribution of all November 2011 calibration factors can be seen in figure 7.7. The core of the distribution is fitted with a Gaussian. The distribution is not exactly Gaussian, but it can still be fitted quite accurately. The mean of the Gaussian is equal to one within the errors with a width of $\sigma = 0.096 \pm 0.002$. Therefore the calibration will not change the mean response significantly.

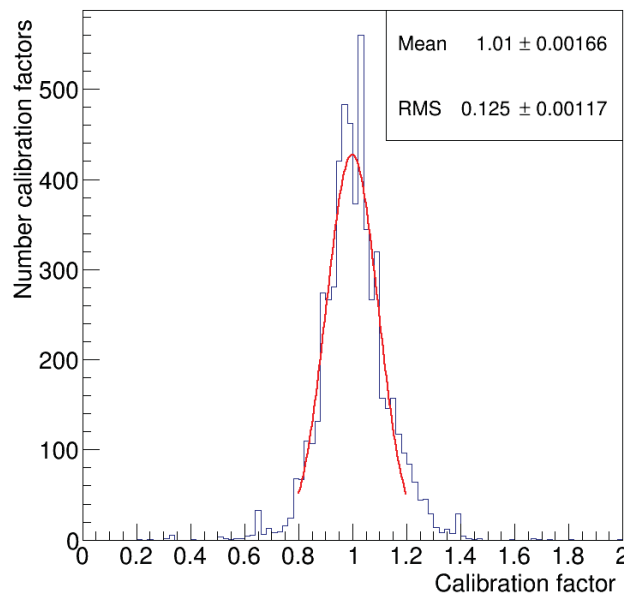


Figure 7.7: Distribution of the calibration factor for all runs. The core of the distribution is fitted to a Gaussian (solid red line).

The main purpose of the equalisation process is to decrease the spread in the response between different runs and RPCs and to improve the resolution of electron and pion events. Hit distributions of the different particles are fitted with a Gaussian in a 2σ range. The important parameters for the Gaussian fit are the mean and width σ . A good working calibration assures that the mean number of hits for different runs at the same energy are close to each other. The energy resolutions, defined as the ratio of the width σ divided by the mean will therefore be smaller than for the uncalibrated data.

In figure 7.8 the hit distribution of both uncalibrated and calibrated 10 GeV positrons are fitted by a Gaussian. The mean of the distributions are taken from the fit. For the

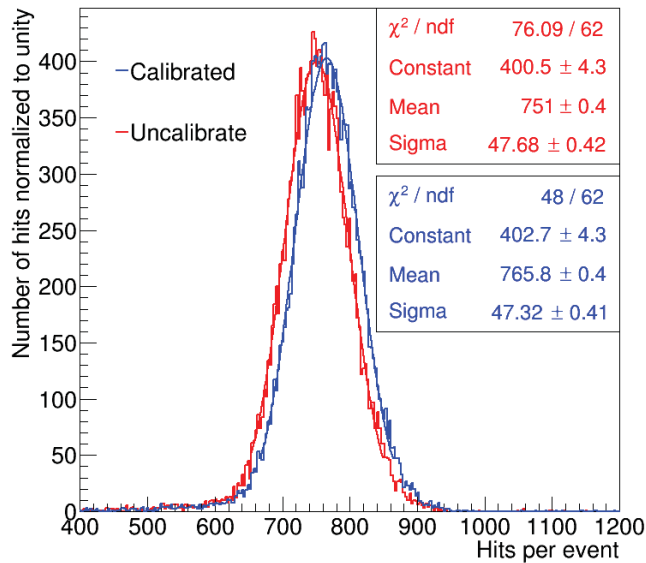


Figure 7.8: Hit distribution of all 10 GeV positron events both uncalibrated (red) and calibrated (blue). The distributions are fitted with a Gaussian in a 2σ range plotted as a solid line.

uncalibrated data the mean of the distribution is 751.0 ± 0.4 and the width $\sigma = 47.7 \pm 0.4$ compared to the mean of the calibrated data of 765.8 ± 0.4 and a width of $\sigma = 47.3 \pm 0.4$. The mean is slightly increased by the calibration and the width is not significantly smaller. This will result into a small improvement in the resolution for the calibrated data can be expected.

More importantly the calibration has to assure that the mean of the hit distributions of the different particles is independent of the operating conditions. In figure 7.9 the mean position of 10 GeV muons and positrons of different runs taken over two days with changing conditions is plotted once before and after equalisation. The mean after equalisation scatters much less than before. The reduced χ^2 of the linear fit is 24.2 (63.1) before and 0.8 (3.1) after equalisation for muons (positrons). The run to run spread in the response is significantly reduced and thus the main goal of the equalisation is achieved. However we can see that the mean of the response is shifted down by 1% for muons and up by 2% for positrons. The equalisation procedure described in section 7.4.1 tends to over correct inefficient layers in dense showers. Therefore the mean of the positron number of hits changes more compared to that of the muons. As the showers become denser with higher energies, their hit distributions will be shifted up and therefore the

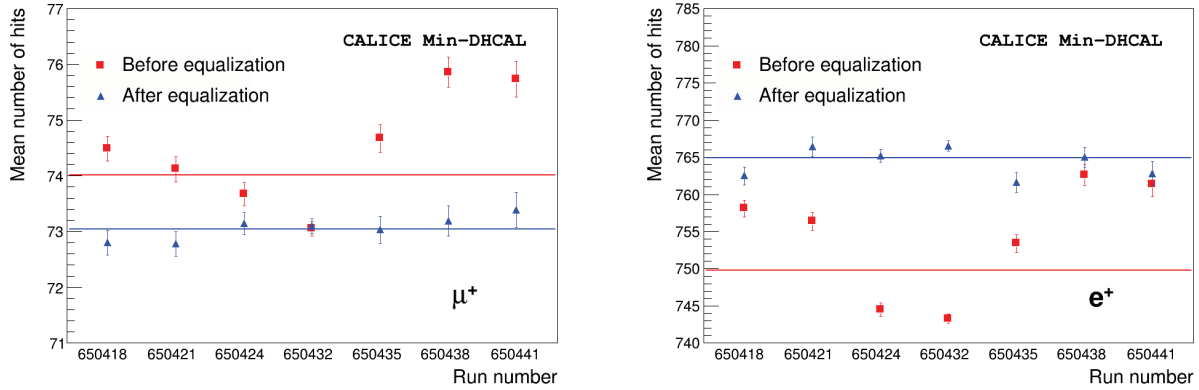


Figure 7.9: Mean hit position of 10 GeV muons (left) and positrons (right) events for different runs before equalisation (red) and after equalisation (blue). Curves are fitted by a constant which is plotted as a solid line. [41]

linearity of the response (see section 8.1) will be different for calibrated and uncalibrated data. This is one of the reasons why alternative equalisation procedures, such as the Density-Weighted Calibration (see [45]), are being developed.

7.5 Monte Carlo Simulation

The simulation of the beam tests is based on the GEANT4 program version 10.p02 [46]. The simulation includes the beam line and the Min-DHCAL stack. The two Cherenkov counters contribute a minimal amount of material to the beam line and are not included in the simulation. Any energy deposition, a so-called point, generated by the simulation in the gas gap of the RPCs is used as a seed for an avalanche (see [47]).

The response of the RPCs is simulated using a standalone program called RPC_sim (see [38]). The latter generates a charge Q , according to measurements of the charge distribution [34], spreads the charge onto the anode plane and defines hits in pads by applying a threshold T on the charge. RPC_sim exists in different versions using various spread functions that simulate the radial charge distribution. For this analysis RPC_Sim 5 is used, which models the charge spread with a double Gaussian function of the form

$$Q(r) = R \cdot e^{-\left(\frac{r}{\sigma_1}\right)^2} + (1 - R) \cdot e^{-\left(\frac{r}{\sigma_2}\right)^2} ; \quad (7.3)$$

featuring three parameters, the widths of the Gaussians σ_1 and σ_2 and their relative weight R . Additional parameters are the charge offset Q_0 and the so-called distance cut d_{cut} . Q_0 is applied to mimic differences in charge generation depending on RPC conditions. The resulting charge Q' is obtained using this offset according to equation 7.4. The d_{cut} function removes energy deposition for points close to one another to mimic local inefficiencies in dense showers. Different functions were tested but the one used here weights the charge as a function of the number of points within 1 cm. The function is plotted in figure 7.10. For 9 or less points the weight is equal to one. If more points are found within 1 cm, then the weight decreases exponentially. This implementation has two parameters, the number of points up to which the full charge is counted, and the rate of the exponential decrease. The hit density distribution of the simulation was seen to depend strongly on the value of the d_{cut} parameter. The value providing the best agreement with the data was chosen as default.

$$Q' = Q + Q_0 \quad (7.4)$$

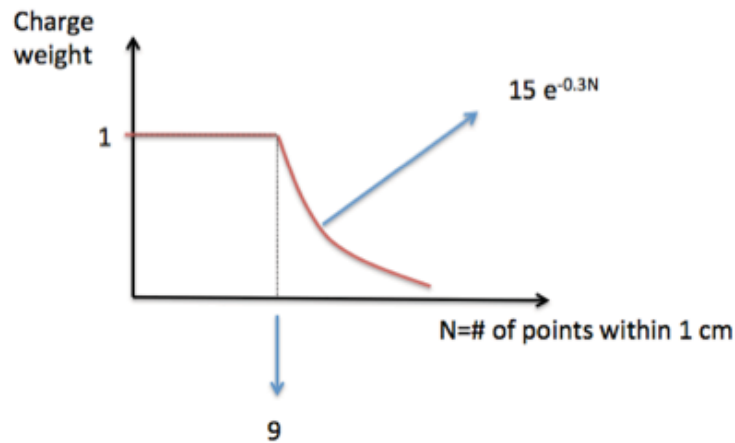


Figure 7.10: The charge weight, called d_{cut} function as used in the Min-DHCAL analysis, as a function of the number of points within 1 cm.

All parameters, except the d_{cut} parameters are tuned using muons. The d_{cut} parameters are used to reproduce the shower response and are tuned with positrons at both 3 and 10 GeV, to get a good agreement over the full energy range. This tuning is based on comparisons of the measured and simulated distribution of numbers of hits, the longitudinal distribution and the distribution of the density of hits (see section 8.2.1). The parameters are optimised by minimising the χ^2 sum of differences between all measured and simu-

lated distributions. As both muons and positrons are used to tune the parameters, the simulation loses their predictive power for both regardless of the energy. Pions however are not used in the tuning process, therefore the pion simulation keeps its full predictive power.

Even though there is an underlying theory (QCD) describing hadronic interactions, actual computations are much more difficult to do than for electromagnetic interactions. GEANT4 provides a general model framework that allows different implementation of processes and models as it has to cover a wide energy range of hadronic interactions [48]. Different models and cross sections are grouped in so-called physics lists and the user decides which physics list to use. The different models have to be validated against data. The highly segmented CALICE prototypes are ideal detectors for this validation. Results obtained with the CALICE Analogue HCAL can be found in [49]. However, further validation for example with the DHCAL prototype is needed.

There are different types of hadronic shower models implemented in GEANT4: data driven, parametrisation driven and theory driven models are used. Data driven models take measurements on e.g. the cross sections and interpolate the data. Parametrisation driven models depend on both data and theory. They take cross section measurements and final states provided by theory. For example the Low Energy Parameterized (LEP) [50] and GHEISHA model [51] are such parametrisation driven models. Theory driven models are dominated by theory and use data mainly for normalisation and validation.

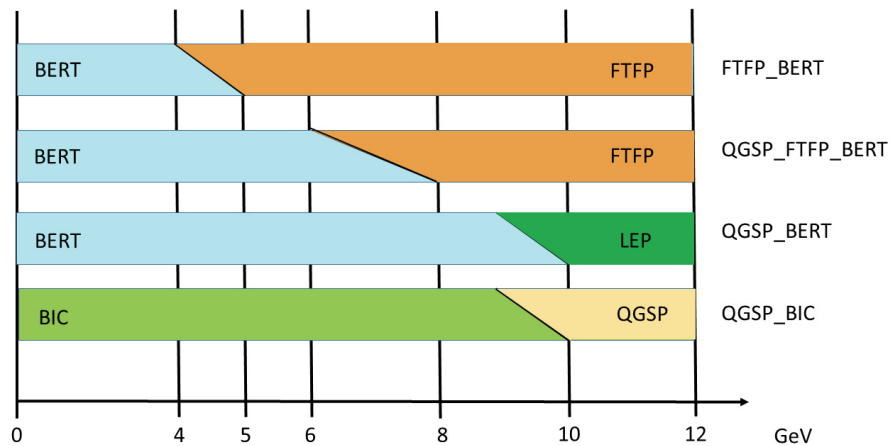


Figure 7.11: Hadronic shower models used by different physics lists implemented in GEANT4 as a function of energy.

The physics lists use different models to cover different energy ranges. Some examples are the "QGS" (Quark Gluon String) model used for data above 20 GeV, "FTF" (Fritiof Model) for interactions above 10 GeV, "BIC" (Binary Cascade Model) and "BERT" (Bertini Cascade Model) for interactions below 10 GeV. The "P" in FTFP and QGSP stands for Precompound model. Precompound models can be extended to higher energies and provide smooth transitions. The standard simulation used here employs the FTFP_BERT physics lists, chosen because it has been proven to show the best results in earlier studies, see e.g. [52]. From the name we can see that it uses both the Fritiof model for high energies (>4 GeV) and Bertini cascades for low energies (0-5 GeV). There is a transition region (4 to 5 GeV) where one model is slowly superseded by the other. Other simulation samples were produced with different physics lists to be compared to data. These are: QGSP_FTFP_BERT, QGSP_BERT and QGSP_BIC. Figure 7.11 shows the model used by these lists as a function of energy.

7.6 Systematic Errors

The following section discusses the systematic errors associated with uncertainties of the measurements as well as uncertainties of the simulation of the setup.

The uncertainties of the measurements lead to the following systematic errors:

- In figure 7.12 the longitudinal shower profile of 10 GeV positrons is shown before and after equalisation. The profile is smoothed out, however the calibration is not perfect and layer to layer variations persist. A systematic error of half the average difference between the results obtained before and after equalisation has been assigned to measurements at each energy. For most measurements this error is applied in both directions (positive and negative). However, for the resolution the error is only applied in the negative direction, since a imperfect calibration always results in a worse resolution than a perfect calibration.
- For high incident particle rates, RPCs demonstrate a loss of efficiency [53]. At the FTBF test beam, the chambers were able to recover their full efficiency in the ≈ 56 second time gap between spills. During the spill however, the efficiency has been measured to first drop exponentially and then to remain constant at a lower

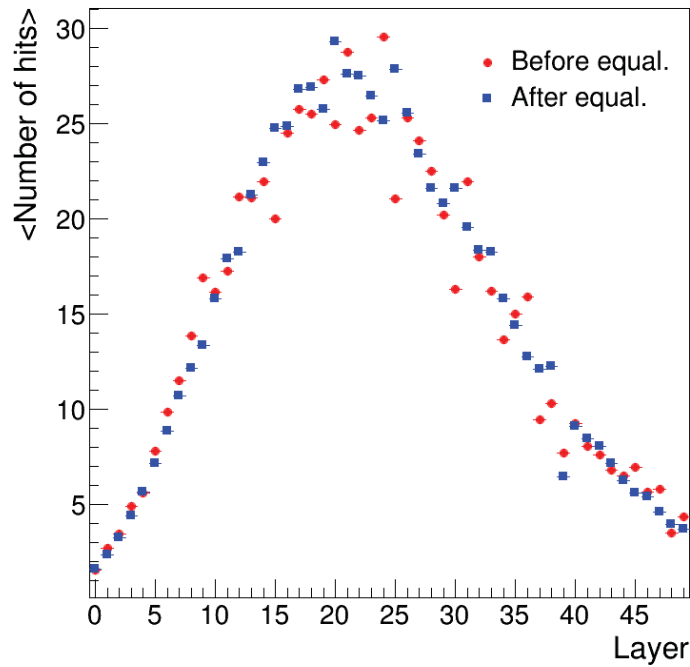


Figure 7.12: Longitudinal shower profile of 10 GeV positrons before (red) and after (blue) equalisation.

value [53]. Figure 7.13 shows the response of the Min-DHCAL to 10 GeV positrons as a function of the spill time. A new spill is identified in the data by looking for large time difference between two consecutive events. The response is fitted to an exponential plus constant term. A 1-2 % decrease over the spill is observed. The same effect is visible in figure 7.14, showing the number of hits as a function of the layer number. The non-statistical scattering is mostly due to calibration uncertainties (see section 7.6). The response decreases with increasing spill time, especially for layers recording most hits and therefore the highest rate. To reduce this effect, only events in the first half second are taken for the longitudinal shower profiles, as here the effect is especially important. A systematic error corresponding to the average difference between the first half second and the rest of the events was assigned to the longitudinal profiles and half the difference to all other measurements. This error is only assigned in the positive direction, since a loss of efficiency can only result in a loss of hits.

- The contribution from accidental noise hits after applying all the selection cuts is estimated to be negligible, as, on average, the noise rate was found to correspond to 0.2 hits per event in the entire stack. Nevertheless the noise was included also

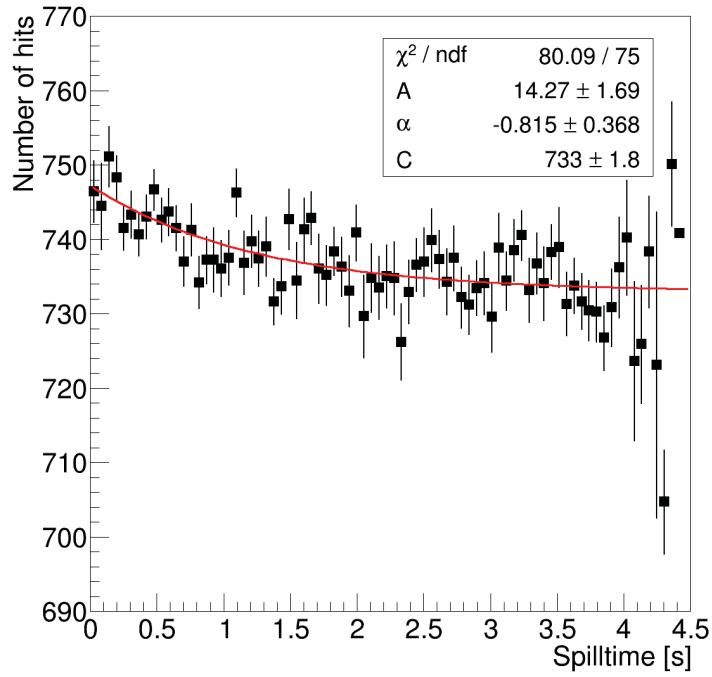


Figure 7.13: Mean number of hits for 10 GeV positrons as a function of the spill time. The response is fitted with an exponential plus constant ($A \cdot e^{\alpha \cdot t} + C$). The fit is plotted in a solid red line.

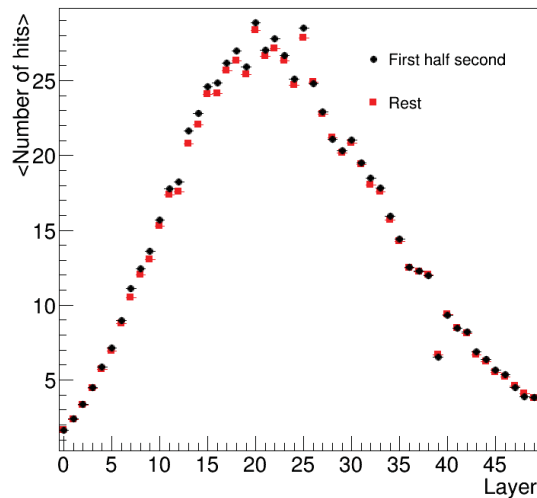


Figure 7.14: The number of hits as a function of layer for 10 GeV positrons. The histogram is normalised to one event. In red are all positrons measured in the first half second of each spill and in black all other positron events.

in the simulation by merging the events of accidental noise runs (see section 7.2.1) taken in the same period with events of the simulation, as noise can for example change the shape of the transverse profiles for muons.

- As discussed in section 7.3, positrons are identified using the Cherenkov signal. Only runs where the Cherenkov counter was working were selected. The contamination from muons and pions in the positron sample was estimated to be less than 1%. Contamination of muons and pions would distort the hit distributions and would be visible as tails or additional peaks. The pion sample sees low contamination from muons, as only 1% of the muons will be identified as pions (see table 7.3). With the requirements on the position of the interaction layer the positron contamination for pions is very small and in fact negligible. Muons have a high contamination from pions, but since pions without an interaction layer and muons are basically indistinguishable there is no systematic error assigned to the muon sample.
- Muons and pions have a systematic error due to their selection based on the interaction layer. For both data and simulation 4 or more hits are required in two consecutive layers. When 4 pads fire in a given layer, the calibrated number of hits can be either smaller or bigger than 4. As there is no equalisation for the simulation, the selection will be different for data and simulation. To estimate the systematic error associated with this selection effect, the required number of hits was varied by 5% in the data, roughly corresponding to the spread of the calibration factors in the data. The average difference was taken as a systematic error. One example of a longitudinal shower profile of 6 GeV pions, where the requirement on the number of hits for the interaction layer was varied can be found in figure 7.15.
- For the positron simulation the only uncertainties originate from the emulation of the RPC response as the accuracy of the simulation of electromagnetic showers in GEANT4 is very high. However, since the muon and positron measurements were used to tune the parameters of the RPC_sim program, no systematic errors have been assigned to the positron and muon simulations. A conservative estimate of the systematic error of the pion simulation is calculated for each measurement by taking the average difference between positrons of data and simulation.

All systematic errors are calculated separately for every energy and measurement and are assumed to be independent. Therefore all errors are added in quadrature. A summary of the different errors for a few measurements is given in table 7.4.

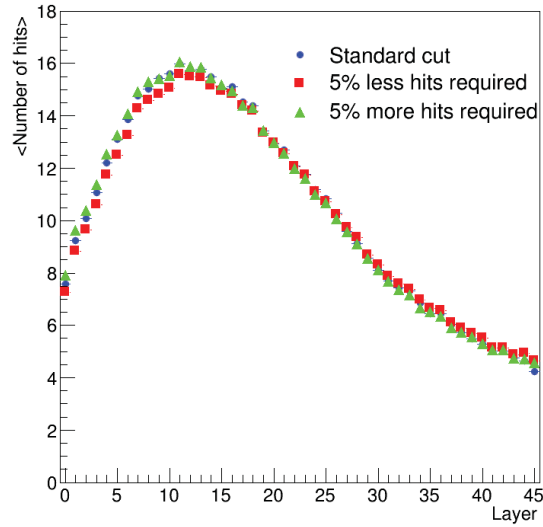


Figure 7.15: The number of hits as a function of layer for 10 GeV pions, in blue is shown the standard cut, in red (green) 5% less (more) hits are required. The profiles are normalised to one particle.

Particle	Systematic error	Longitudinal profiles [6 GeV]	Transverse profiles [6 GeV]	Mean Response [all energies]
Pion	Calibration uncertainty	$\pm 3.1\%$	$\pm 1.2\%$	$\pm 2.1\%$
	Loss of efficiency	+1.3%	+0.6%	+0.6%
	Interaction point	$\pm 1.3\%$	$\pm 2.3\%$	$\pm 3.5\%$
Positron	Calibration uncertainty	$\pm 4.1\%$	$\pm 1.2\%$	$\pm 2.8\%$
	Loss of efficiency	+1.3%	+0.6%	+0.6%
	Interaction point	n/a	n/a	n/a
Muon	Calibration uncertainty	$\pm 2.1\%$	$\pm 1.2\%$	$\pm 0.8\%$
	Loss of efficiency	+1.3%	+0.6%	+0.6%
	Interaction point	$\pm 1.2\%$	$\pm 5.6\%$	$\pm 1.0\%$
Pion simulation	Emulation error	$\pm 6\%$	$\pm 10\%$	$\pm 1.0\%$

Table 7.4: Systematic errors in percent for data and the pion simulation. The errors for the longitudinal and transverse profiles are given as an example for 6 GeV.

Chapter 8

Results

In the first section of this chapter a brief summary of the DHCAL with steel absorber (Fe-DHCAL) test beam data analysis is presented.

This thesis analysis is based on test beam data taken with the DHCAL with minimal absorber at Fermilab in November 2011. The results of my analysis are presented separately for the different particle types present in the beam data. First the positron analysis is presented, followed by muons and pions. A general description of the calorimeter response to the various particles is given, followed by a detailed shower and hit density analysis. Results of this analysis are presented and compared to the results of the usual configuration with absorber as well as to simulation based on GEANT4. A linearisation method is presented which uses the hit density of positrons to linearise the electromagnetic response of the detector. Different physics lists are tested by comparing them to the pion data. Energy and momentum units are used interchangeably throughout the text.

8.1 DHCAL Test Beam with Steel Absorber Structure

In 2010 and 2011 test beam data was taken at Fermilab. In total ≈ 14 million secondary beam events over five test beam periods were recorded with particle energies ranging from 2 to 60 GeV. The common configuration consisted of 38 detector layers with 1.75 cm thick steel absorber plates plus a 14-layer structure called 'tail catcher', featuring 2

cm thick steel plates for the first 8 layers of the catcher followed by 10 cm thick steel plates. Details of the equalisation procedure can be found in section 7.4.1. PID was done either by utilising the Cherenkov counter in the beamline or applying a topological PID for runs with inefficient Cherenkov counters. The topological PID efficiencies range from 95% to 100% both for pions and positrons depending on the beam energy. Details of the particle selection cuts can be found in [45]. All results and figures in this Fe-DHCAL section originate from two previous CALICE notes [45] and [20].

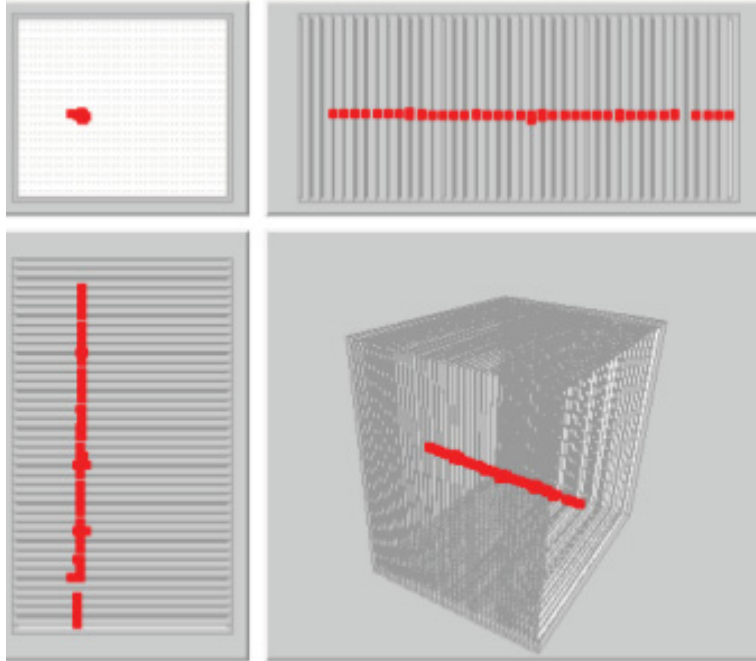


Figure 8.1: A muon track featuring some delta ray production in a few layers [20].

Muons act as Minimum Ionising Particles (MIPs), apart from some delta ray production, in the given energy range and most of them pass through the whole detector (see section 6.2). A typical muon track is shown in figure 8.1. Most muons leave a straight and narrow track in the detector, however some muons are also scattered and change direction inside the detector. In this figure we can also see that the Noise rate is very low in the DHCAL, no hits away from the track are recorded in the event. In dedicated noise measurements the noise rate in the Fe-DHCAL was measured to be 0.1 hits per event on average [54].

Figure 8.2(top) shows a 8 GeV pion event. Pions generally feature a MIP-like segment before the interaction layer, which marks the beginning of the hadronic shower. In this configuration, positrons are stopped very early in the detector. A typical 8 GeV positron event is shown in figure 8.2(bottom). Positrons produce short and narrow showers.

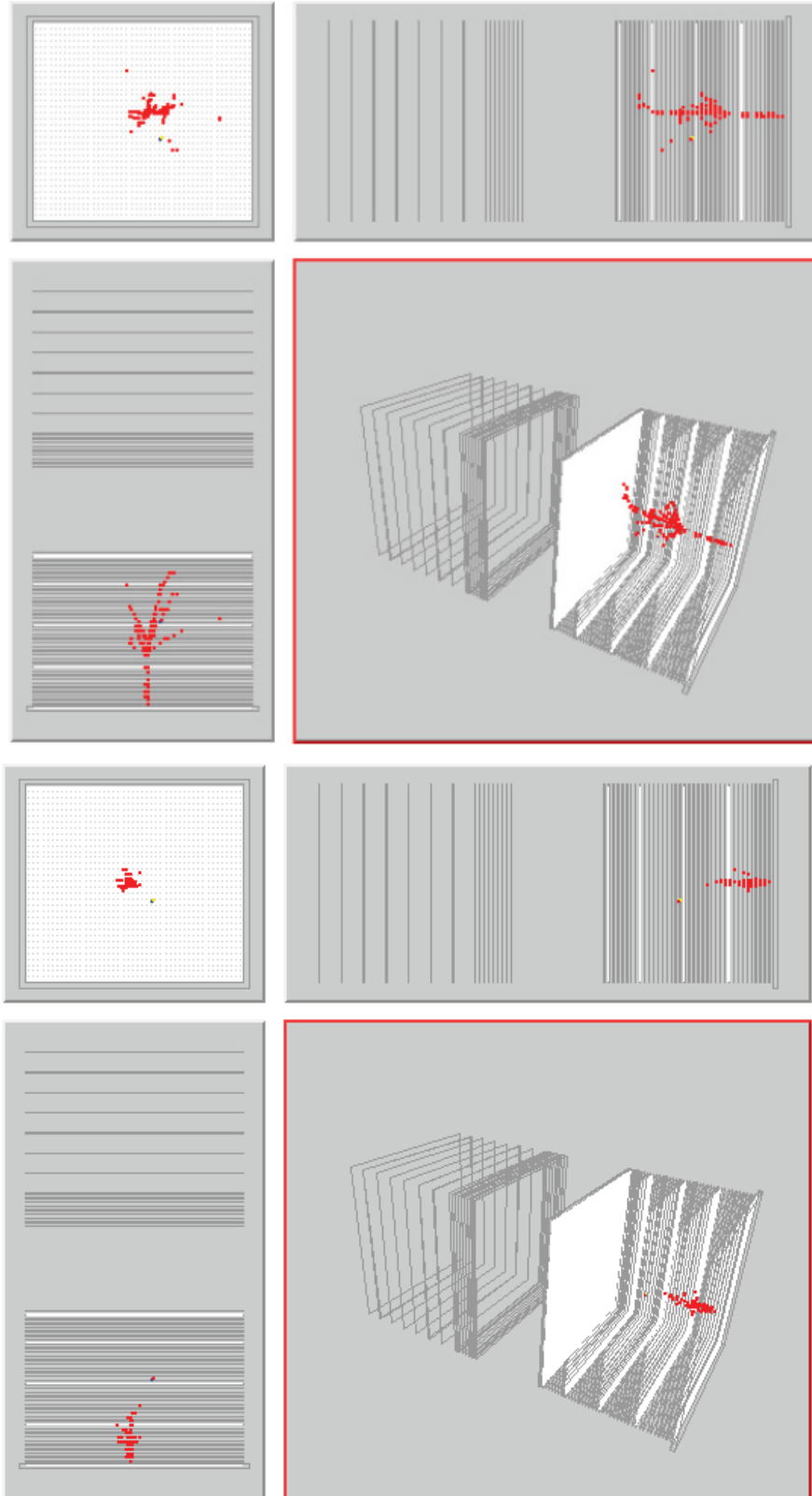


Figure 8.2: A typical 8 GeV pion (top) and positron (bottom) event recorded with the Fe-DHCAL. The event displays include the tail catcher.

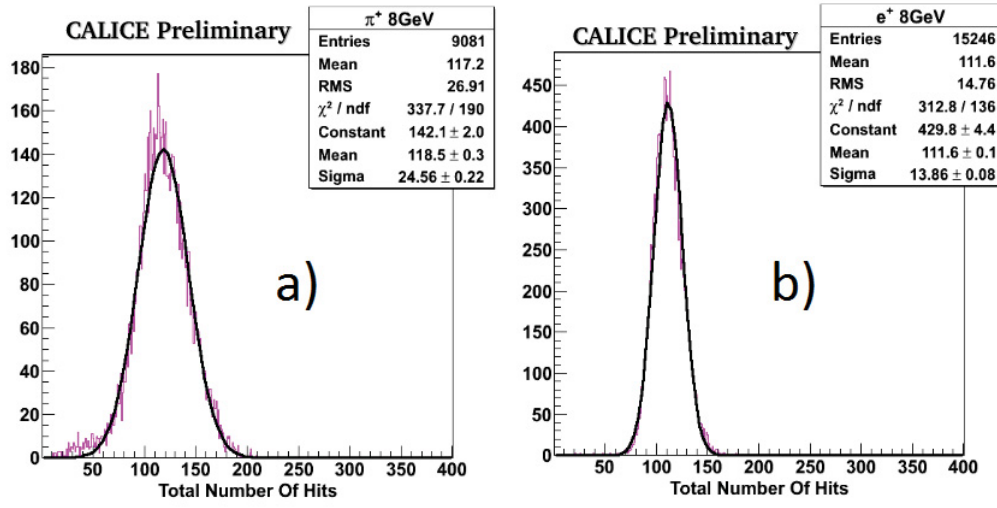


Figure 8.3: The hit distributions of 8 GeV pions (a) and positrons (b) event recorded with the Fe-DHCAL [20].

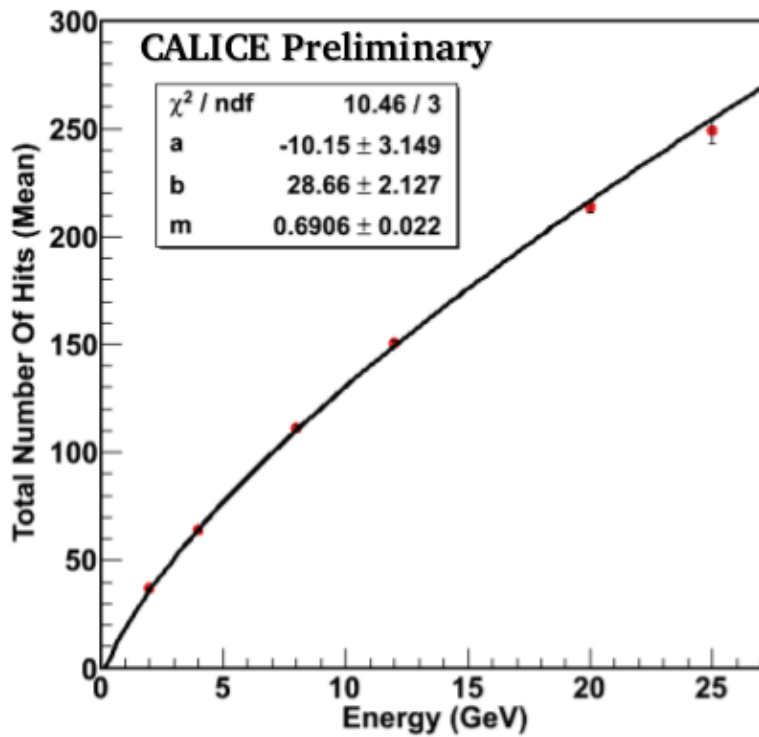


Figure 8.4: Mean response of the Fe-DHCAL to positrons [20].

The mean response of the Fe-DHCAL to positrons and pions is obtained by fitting the hit distributions to Gaussian fits and taking the maximum of the Gaussians. Figure 8.3 shows the hit distributions of 8 GeV pions and positrons as well as the fits. The mean response as a function of the beam energy can be found in figure 8.4. Points are fitted with a power law fit of the form

$$N_{hit} = a + bE_{beam}^m . \quad (8.1)$$

The exponent m of this power law is a measure of the non-linearity (saturation) of the response. When m is equal to one, the response is linear. If the exponent is smaller than one, then saturation occurs. In the heart of showers, more than one particle will pass through a cell but due to the digital readout and the limited granularity only one hit is recorded, leading to a saturation of the response. The fit describes the data well. An exponent of $m = 0.69$ indicates a large saturation. The inverse of the fit is used to reconstruct the energy and meanwhile correct for non-linearity. The reconstructed energy distributions are fitted once again to a Gaussian. The width of the distributions as a function of the beam energy can be found in figure 8.5, showing both the resolution for the response corrected for non-linearity and without this correction. The resolution curves are fitted with the standard parametrisation, see equation 4.16. The instrumental error summarised in parameter b is very small for the DHCAL and therefore neglected. The linearisation improves both the stochastic and constant term.

The mean response and resolution of pions can be seen in figure 8.6. The DHCAL shows a nearly linear response to pions and a stochastic term of $\alpha = 0.63$. Only energies below 25 GeV are used for the fit as saturation effects become important for higher energies. Saturation deteriorates the resolution despite the correction using the power law fit.

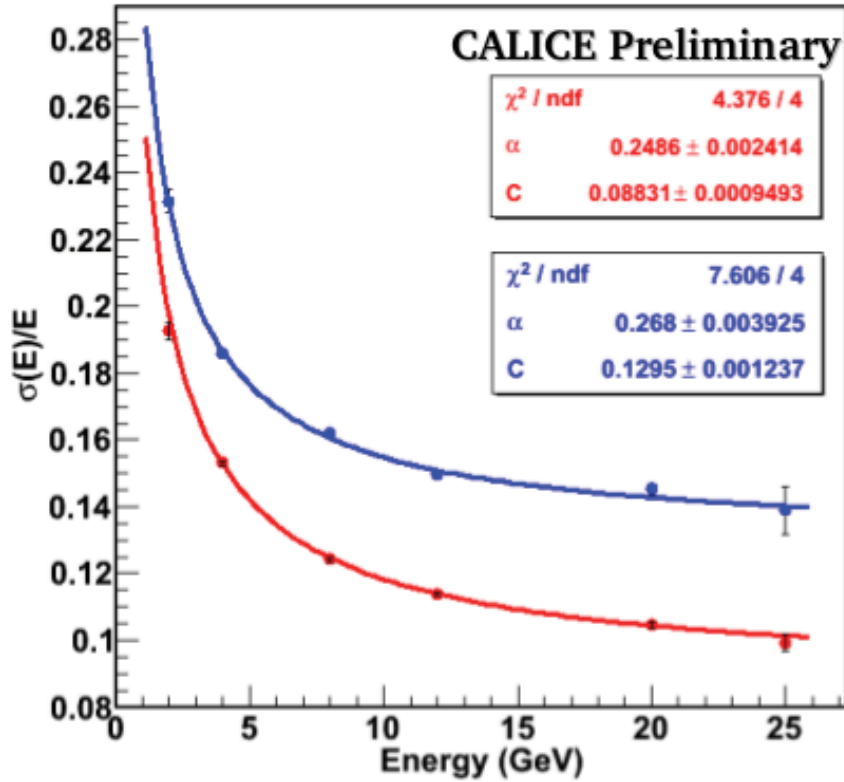


Figure 8.5: Corrected (blue) and uncorrected (red) electromagnetic energy resolution for the Fe-DHCAL [20]. The standard fits, according to equation 4.16 where b is set to zero due to the low instrumental noise, are shown as solid lines.

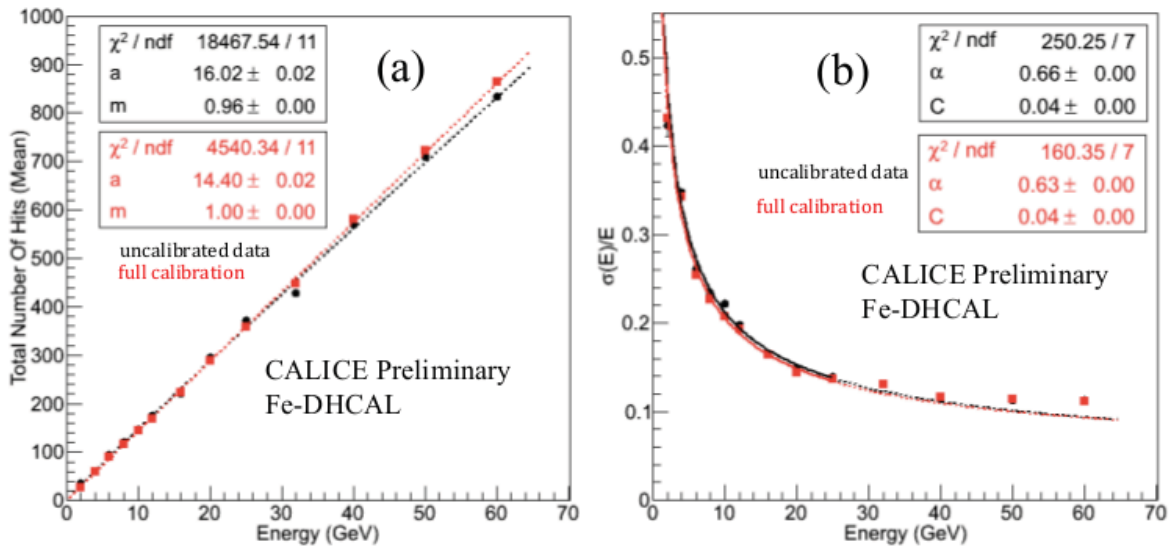


Figure 8.6: Mean response (a) and resolution (b) for the uncalibrated pion data (black) and the calibrated (red). The resolution fits are made up to 25 GeV (solid) and are extrapolated to 60 GeV (dashed). [45]

8.2 Results of the Min-DHCAL analysis

DHCAL with Minimal absorber (Min-DHCAL) allows particle interactions to be observed in two orders of magnitude larger topological details compared to conventional calorimeters or the Fe-DHCAL. In figure 8.7 an 8 GeV positron event recorded with the Min-DHCAL is shown. In this figure the advantages of the minimal absorber configuration are obvious as the electromagnetic shower is spread over the entire detector prototype, compared to only a few layers as seen in figure 8.2(right). Therefore the present data set is ideal for detailed comparisons to GEANT4-based simulations.

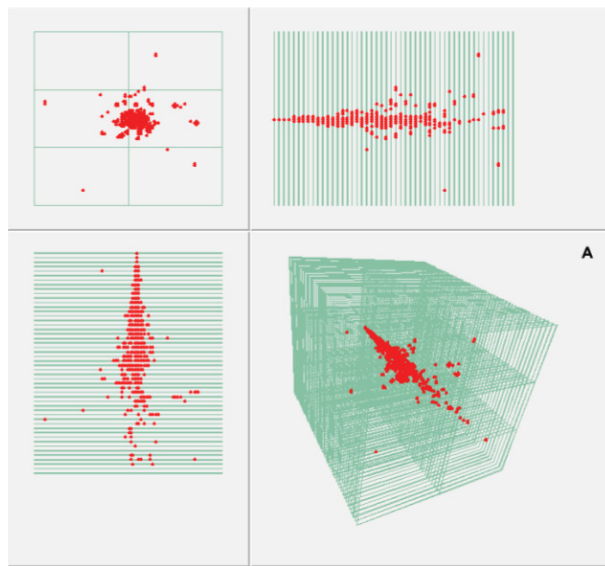


Figure 8.7: A 8 GeV positron event recorded with the Min-DHCAL, featuring a front, side, top and perspective view. [41]

8.2.1 Response to Positrons

Figure 8.8 shows the distribution of the number of hits for all selected positron events and for all different beam momenta. Each response distribution has been normalised to unity and is shown in individual colours. The response curves feature only small tails, at the level of 10^{-3} in height, mostly towards lower numbers of hits. These tails are also present but smaller in simulation. The tails in data might include contamination from other particles. The curves are fitted to Gaussian functions, which fit the responses well, in the range of $\pm 2\sigma$ around the most probable value.

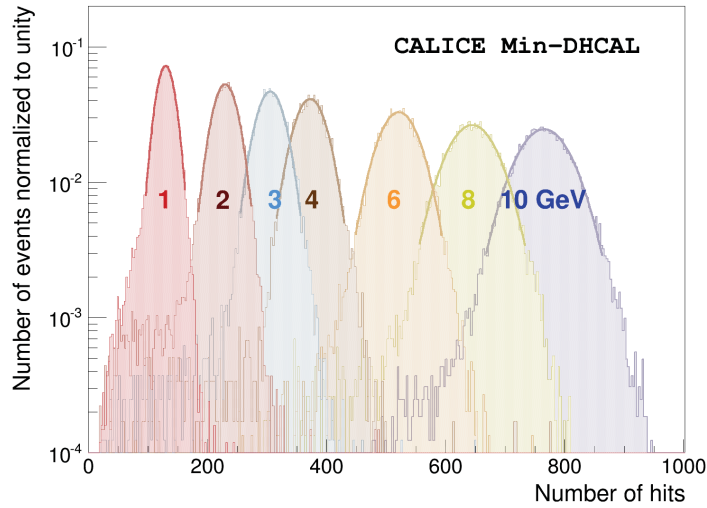


Figure 8.8: Distribution of the number of hits for all selected positron events. The distributions for each beam momentum setting are plotted separately and their areas are normalised to unity. In the range of ± 2 standard deviations, the data have been fitted with a Gaussian function. The results of the fits are shown as solid lines. [41]

The mean values obtained from the Gaussian fits are shown as a function of beam energy in figure 8.9. The error bars include both statistical and systematic errors, see section 7.6. The largest errors originate from uncertainties included by the equalisation procedure, see section 7.4.1. The statistical errors are in general very small. The results of the simulation are also included in the figure, both responses seem to be in reasonable agreement. Both are fitted to a power law function, see equation 8.1, where the parameter a was set to 0. The fit values can be found in the figure. There is a good agreement between data and simulation as the fit values agree within the errors. The 1 and 2 GeV responses seem slightly too low for the simulation. This mismatch for 1 and 2 GeV is probably linked to other discrepancies observed between simulation and data for many measurements, which are described later in this section. These two points have been excluded from the fit, as otherwise they would deteriorate the fit significantly. The impact of this exclusion on the resolution is discussed in section 8.2.1.

Leakage and Saturation of Positron Showers

Figure 8.9 showed a non-linear hit response to positrons due to saturation and leakage. Without absorber plates present, many particles pass through the detector without losing

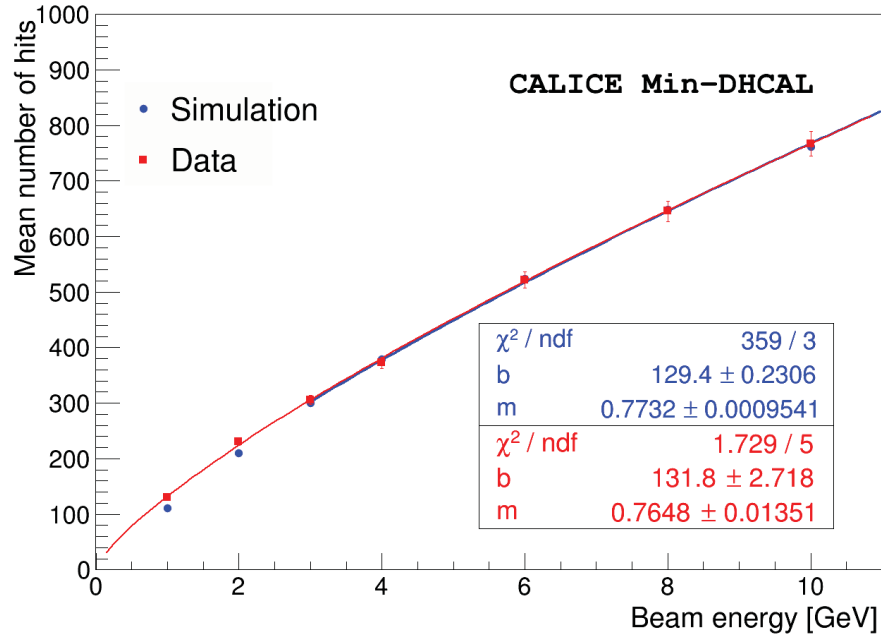


Figure 8.9: Mean response of positrons versus beam energy for both data (red) and simulation (blue). Both data sets are fitted with a power law (see equation 8.1) shown as solid lines where a is set to 0 [41].

all of their energy. Even though positrons usually interact early, with most of their energy deposited inside of the detector, some energy leakage occurs. The amount of hits lost due to leakage out of the back of the detector can be estimated by fitting the longitudinal shower profiles with a gamma function (see equation 4.13). The gamma function gives a good description of the energy deposition and in first approximation this is equivalent to the number of hits recorded per layer.

	m	b
Before leakage correction	0.76 ± 0.2	131.8 ± 2.9
After leakage correction	0.77 ± 0.2	132.2 ± 2.9
After linearisation	0.95 ± 0.01	100.2 ± 1.2

Table 8.1: Fit parameters for the exponent m and the constant b of the power law fit (see equation 8.1) for the positron response before and after leakage correction (see section 8.2.1) and after linearisation (see section 8.2.2).

The shower profile of all positron events with 6 GeV can be seen in figure 8.10. The gamma function fit is extended beyond the actual depth of the DHCAL to estimate leakage. Integration of the curve provides an estimate of lost hits. The response can then

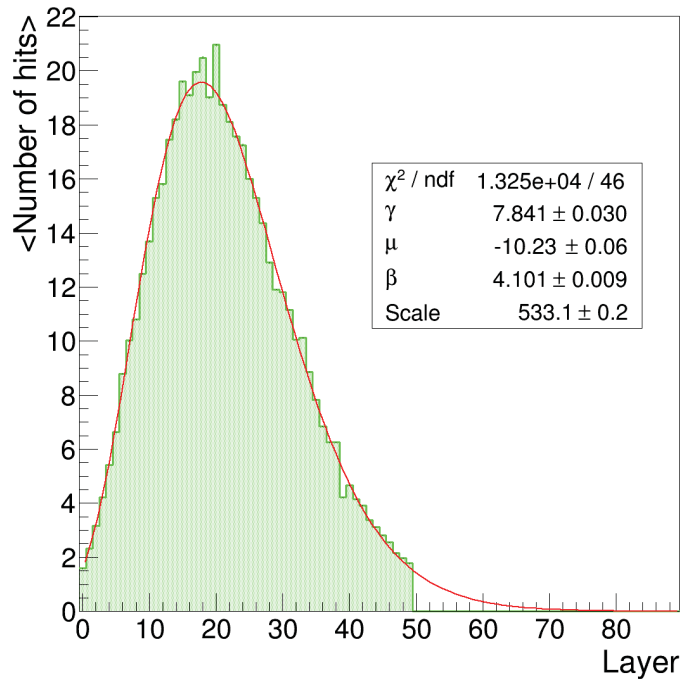


Figure 8.10: Longitudinal shower profile of all positrons at 6 GeV. The red line is a Gamma function fit (see equation 4.13, where E_0 is replaced by a scale parameter).

be corrected in average for leakage out of the back of the detector using this number. In figure 8.11 the responses before and after correction are shown. Both are fitted with a power law function and the fit parameters are summarised in table 8.1. The impact of leakage on the response of positrons is negligible for low energies and at maximum a 3% effect for 10 GeV.

The remaining non-linearity is mostly due to saturation, which is caused by the digital readout and limited granularity of $1 \times 1 \text{ cm}^2$. As the only information available is binary, the energy and number of particles passing through a single pad is not known. For higher energies, electromagnetic showers are more dense and more energy is deposited in a single pad compared to lower energies. The hit response is therefore saturated.

Compared to the results obtained with steel absorber material (see figure 8.4), the saturation effects in figure 8.9 are, as expected, smaller in this minimal absorber configuration, as showers are less dense.

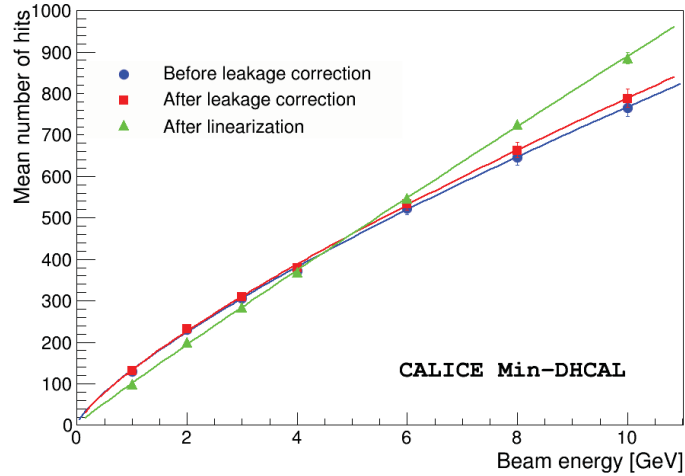


Figure 8.11: Mean number of hits for positrons as function of beam energy: before any correction (blue), after leakage corrections (red) and after linearisation (see later section 8.2.2) of the response based on the hit densities (green). [41]

Resolution of Positrons

The inverse of the power law fit function is used to reconstruct the energies of the positrons event by event. The resulting energy distributions for both data and simulation is shown in figure 8.12. All energy distributions are normalised to unity. The energy distributions are fitted once again by a Gaussian.

Using the width σ and the most probable value E_{mean} obtained from Gaussian fits of energy distributions from figure 8.12, the resolution is given by the ratio $\frac{\sigma}{E_{mean}}$. The statistical error e_{stat} is calculated using the statistical errors on σ and E_{mean} values via the formula:

$$\frac{e_{stat}(\frac{\sigma}{E_{mean}})^2}{(\frac{\sigma}{E_{mean}})^2} = \frac{e_{stat}(\sigma)^2}{\sigma^2} + \frac{e_{stat}(E_{mean})^2}{E_{mean}^2} . \quad (8.2)$$

The resulting energy resolution as function of the beam energy for both data and simulation is shown in figure 8.13. There is a $\approx 2.5\%$ spread in the beam momentum, as stated by the Fermilab website [40], this uncertainty was removed from the measured resolution. The resolution is fitted by the standard parametrisation with a constant and a stochastic term (see equation 4.16), in this formula b can be neglected in the DHCAL as the noise rate is small. The fit parameters are summarised in table 8.2. Whereas the

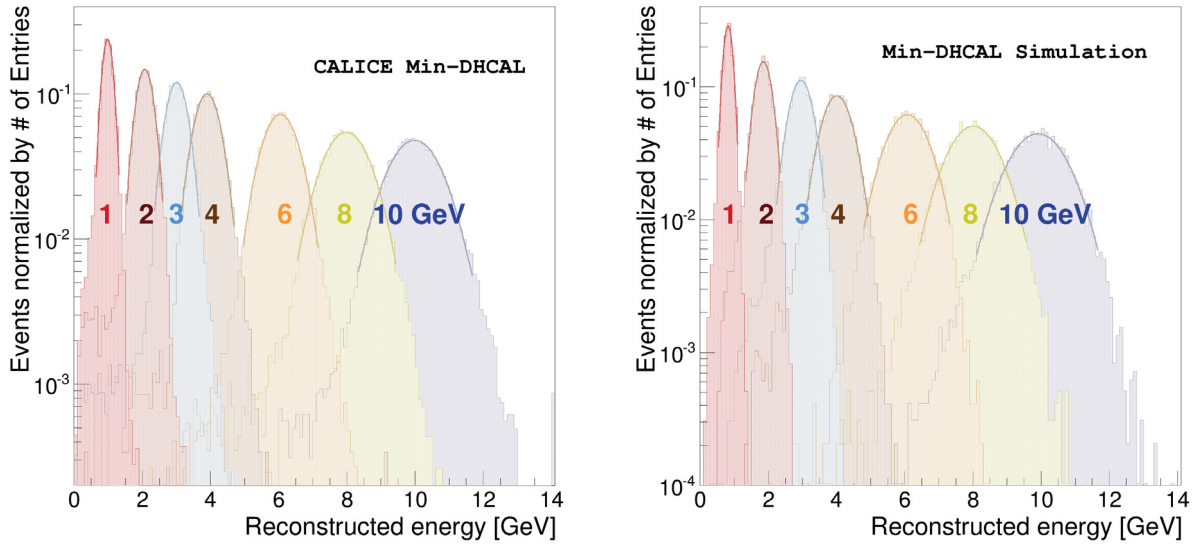


Figure 8.12: Energy distributions for positrons of data (left) and simulation (right). The different beam energies are indicated with different colours. The area of the distribution at each beam energy was normalised to unity and fitted to a Gaussian function in the range of ± 2 standard deviations [41].

stochastic term agrees well for both data and simulation, the measured energy resolution is approximately 15% better than the one obtained by simulation. This results in a smaller constant term for the data. The reasons for this difference are not understood. As the 1 and 2 GeV points were excluded from the power law fit for the simulation (see figure 8.9), these two points are not perfectly corrected for non-linearity which results in worse energy resolution for them. This does not explain however the differences observed for 4 to 10 GeV. The constant term in both curves is comparatively large due to the above mentioned saturation effects. When compared to the steel absorber configuration (see figure 8.5), the positron resolution of the Min-DHCAL shows an 11% improved stochastic term and a $\approx 2\%$ smaller constant term.

	α [%]	C [%]
Data without leakage correction	14.3 ± 0.4	6.3 ± 0.2
Data with leakage correction	14.2 ± 0.4	5.8 ± 0.2
Simulation	14.2 ± 0.2	8.2 ± 0.1

Table 8.2: Fit parameters for the constant and stochastic terms of the energy resolution (equation 4.16) for positrons for data and simulation.

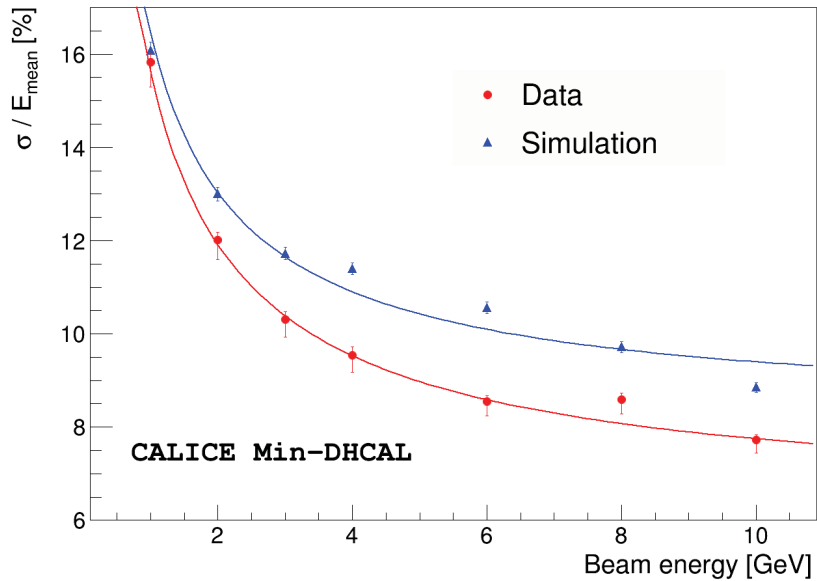


Figure 8.13: Energy resolution for positrons in the energy range from 1 to 10 GeV for data (red) and simulation (blue) before leakage correction. The standard fits, according to equation 4.16 where b is set to zero due to the low instrumental noise, are shown as solid lines. [41]

In figure 8.14 the energy resolution is shown before and after leakage correction. Once again the curves are fitted with the standard parametrisation. Table 8.2 shows the parameters obtained from the fits. There is a 1% improvement in the resolution and the constant term is 8% smaller. Conclusively it is shown that leakage correction can be used to improve both the linearity and resolution of the positrons (see table 8.2 and table 8.1).

Longitudinal and Transverse Shower Profiles

The high number of readout channels of the DHCAL provide an unprecedented tool for a detailed study of shower shapes. As an example the longitudinal shower profile of 6 GeV positrons for both data and simulation are shown in figure 8.15 (left). The data and its fit are identical to figure 8.10. Once again the shower profiles are fitted using Gamma distributions, see equation 4.13. The shower maximum is observed around layer 18, where the fit to data seems to show a slight deficiency compared to the simulation. However the fit only gives a good description of the energy loss per layer and not necessarily for the number of hits, a perfect fit is not expected. The same mismatch of the fit is observed when fitting the simulation (see figure 8.15 (right)).

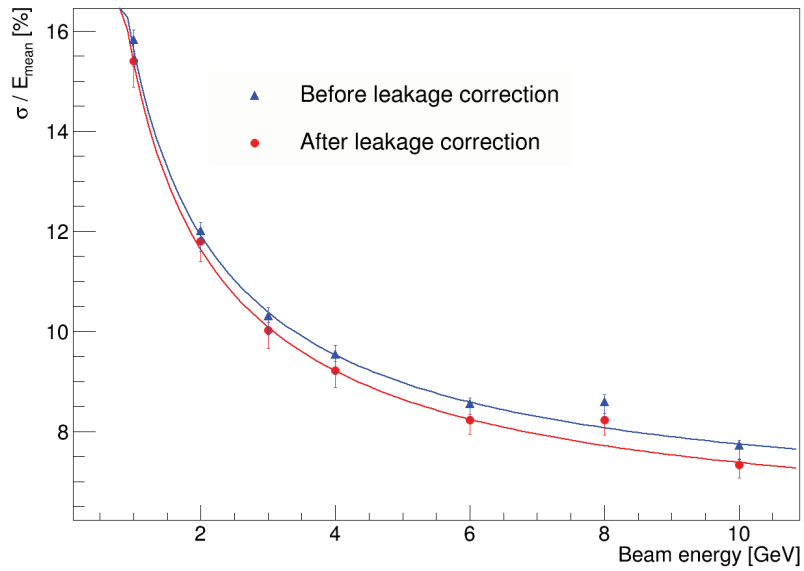


Figure 8.14: Energy resolution for positrons in the energy range from 1 to 10 GeV for both before (blue) and after (red) leakage correction. The standard fits are shown as solid lines.

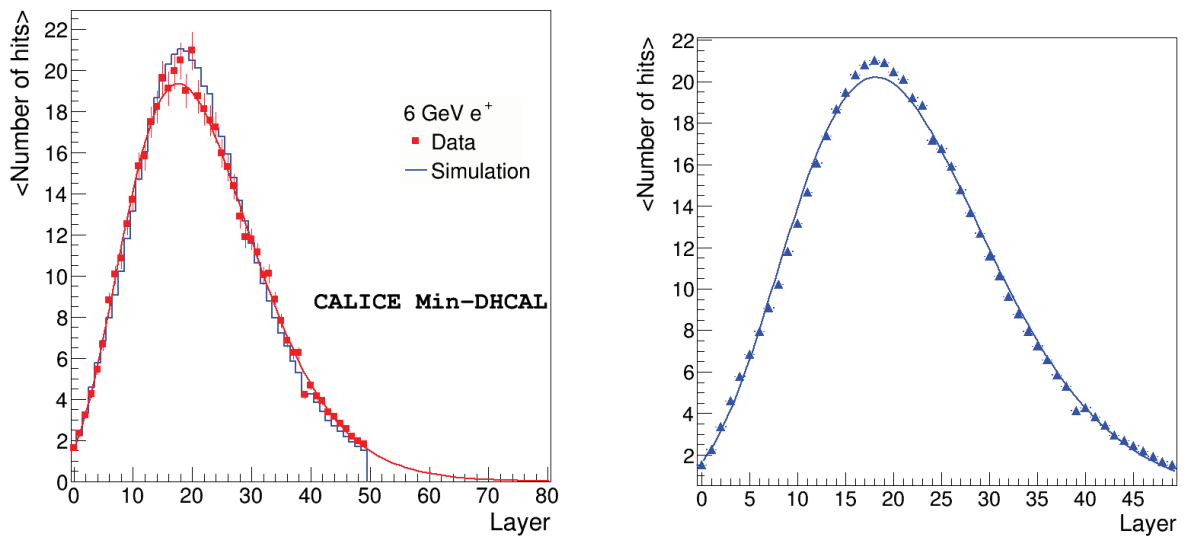


Figure 8.15: The left (right) plot shows the measurement of the longitudinal distribution for 6 GeV positrons for data (simulation), i.e. the average number of hits as a function of layer number. The data (red) in the left plot is compared to simulation (blue histogram) [41]. The red line in the left plot is the Gamma distribution fit to data (see 4.13). In the right plot the simulation (blue) is fitted with a Gamma distribution, also shown in blue.

The gamma distribution fit can be used to calculate the shower maximum, see equation 4.14. Figure 8.16 shows the shower maximum as a function of the beam energy for both data and simulation. The error bars includes statistical and systematic errors and are smaller than the dot size. A significant difference between data and simulation can be observed but the agreement is still fairly good.

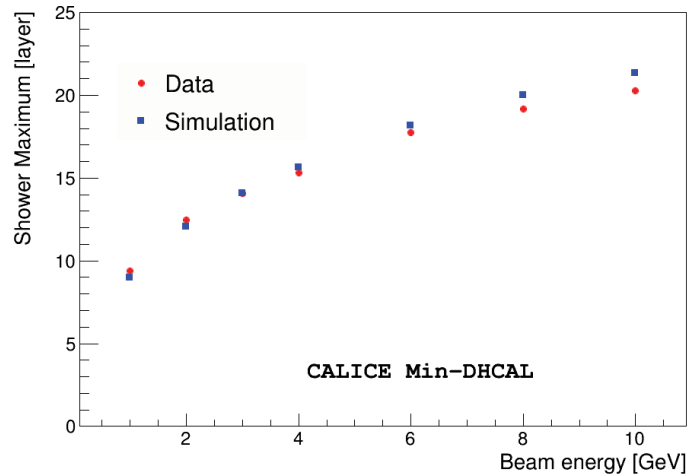


Figure 8.16: Average position of the shower maximum for positrons of both data and simulation [41].

The mean dispersion is another important parameter for comparisons. The longitudinal dispersion for each event can be calculated as

$$D_z = \sqrt{\frac{\sum z_i^2}{N} - \left(\frac{\sum z_i}{N}\right)^2}; \quad (8.3)$$

where the sum is over all hits i in an event, z_i is the layer of each hit and N the total number of hits. The mean dispersion as a function of the beam energy is shown in figure 8.17. The agreement between data and simulation is satisfactory.

In order to measure the transverse shower shape, for each event straight line fits are performed independently to the hits in the x/z and y/z planes. These lines define the mean axis of the shower. All hits in the first 5 layers, independently of the position of the interaction layer, are used for this fit. It is required that the reduced χ^2 value of the fit is smaller than one, that there are at least one hit in three of the first 5 layers and that

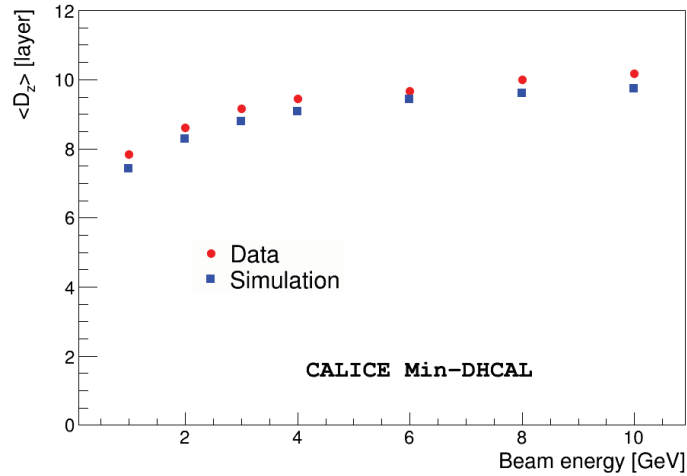


Figure 8.17: Dispersion of hits in longitudinal direction for positron induced events: data is plotted in red and simulation in blue. [41]

the angle of the fit compared to the mean axis is smaller than 0.1 radians ($\approx 6^\circ$) in both horizontal and vertical directions. One example of such a fit can be seen in figure 8.18.

Once the shower axis is identified, the radius R is given by the perpendicular distance to the axis. In figure 8.19 the transverse profile of 6 GeV positrons is shown for both data and simulation. The accelerated decrease in entries above a radius of 50 cm is an artifact of the square shape of the detector planes with dimensions of $96 \times 96 \text{ cm}^2$. Good agreement between data and simulation is observed in the transverse shower shape over the entire range of radii. However, compared to the simulation, the data show less hits close to the shower axis and an excess at large distances. Both the statistical and systematic uncertainties are small.

To compare the transverse profiles of data and simulation over the whole energy range a mean distance is calculated by averaging over all events and hits at a given energy. The result is shown in figure 8.20. The average radial distance is seen to be larger in data than in simulation. The effect of noise in the data can be excluded as a cause of this effect, as noise was added to the simulated events.

The radial dispersion of hits in an event is calculated similar to the longitudinal dispersion as:

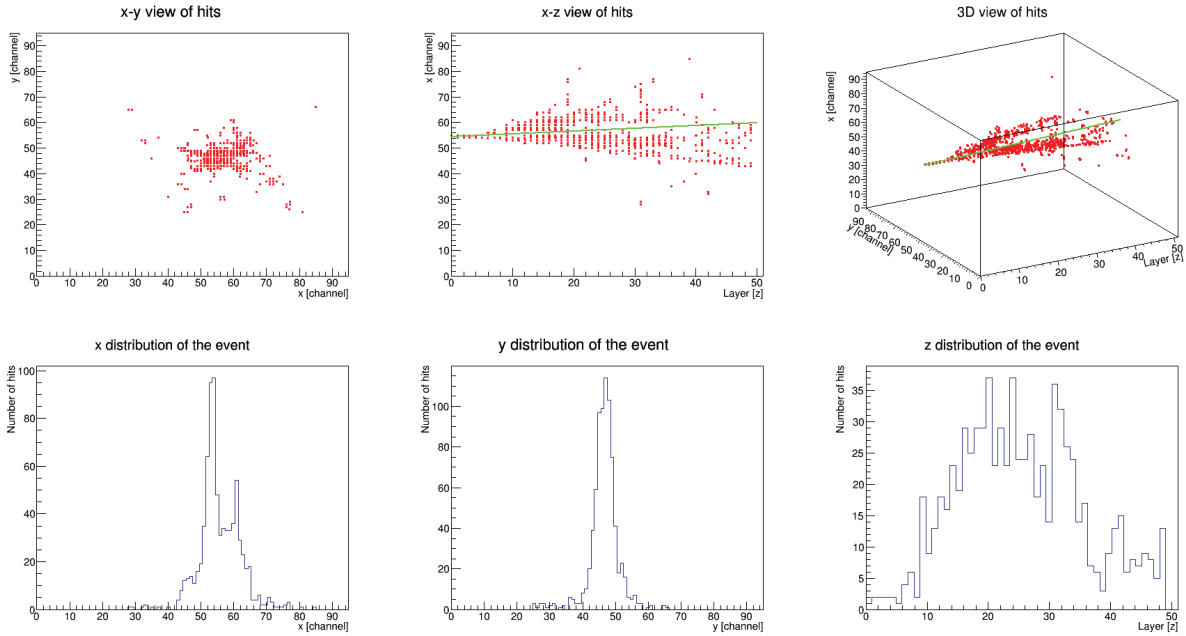


Figure 8.18: Example of a 10 GeV pion shower, the calculated shower axis is plotted in green.

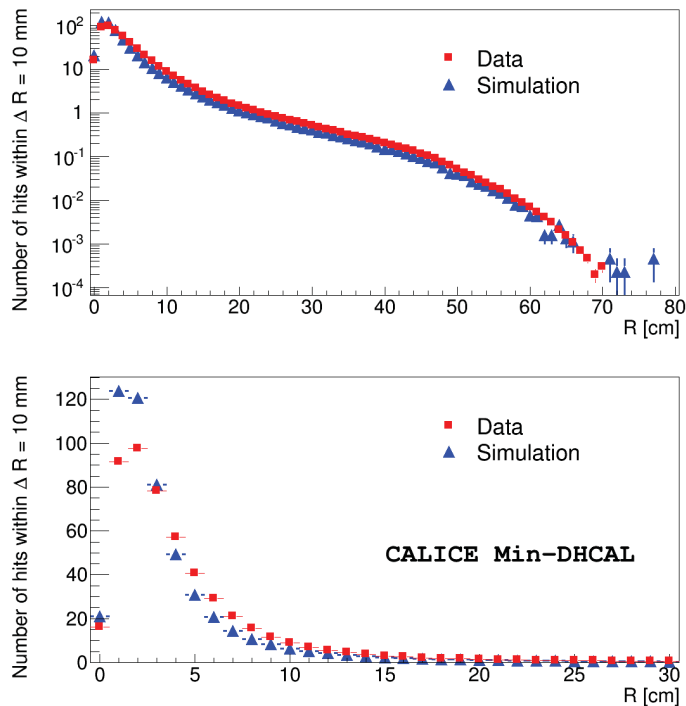


Figure 8.19: Distribution of the radial distance of hits from fits to straight lines to the ensemble of hits in an event for 6 GeV positrons. The upper (lower) plot uses a logarithmic (linear) y-scale. The histograms are filled with all events and normalised by the number of events. [41]

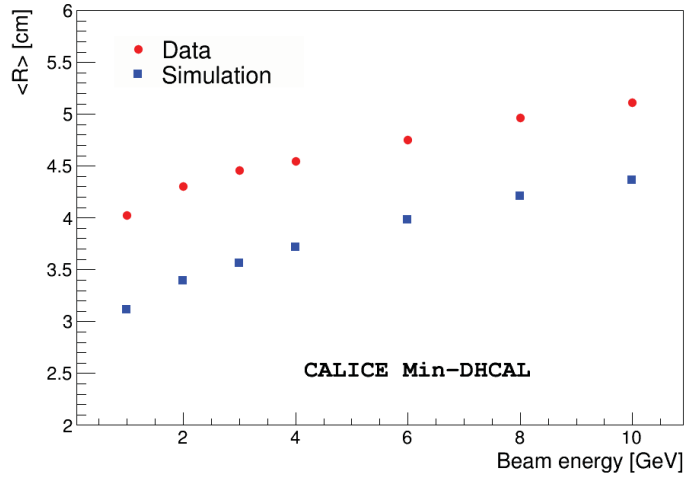


Figure 8.20: Mean distance of hit in an event to the fitted shower axis for both data (red) and simulation (blue). [41]

$$D_R = \sqrt{\frac{\sum R_i^2}{N} - \left(\frac{\sum R_i}{N}\right)^2}; \quad (8.4)$$

where R_i is the radius of every hit and N the total number of hits in an event.

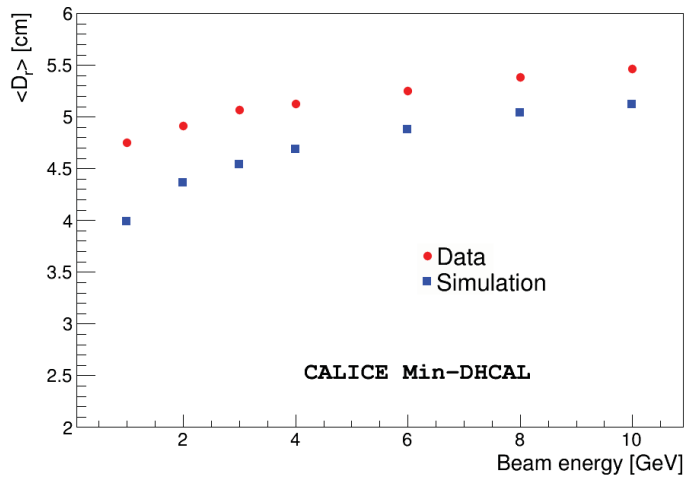


Figure 8.21: Dispersion of hits in longitudinal direction for positron induced events: data (red) and simulation (blue). The dispersion is averaged over all events at a given beam energy and is plotted as function of beam energy. [41]

The average radial dispersion as a function of the beam energy is shown in figure 8.21.

As was expected by looking at the average radius, the dispersion of positron showers is larger in data than in simulation. Thus the size of showers is underestimated in the simulation. Possible explanations for this discrepancy will be given in the next section.

The Density of Hits

The density of a given hit is defined as the number of hits within a volume of $3 \times 3 \times 3$ pads surrounding the hit. Figure 8.22 shows the distribution of the density of hits for 6 GeV positrons for both data and simulation. The hits in the simulation show a higher density than the hits in data. This was expected looking at the comparison of the mean radius and dispersion of hits (see figure 8.20 and 8.17) as these measures are correlated. As explained in section 7.5 the density histograms were one of the measurements used to tune the d_{cut} parameters of the RPC_sim program, however despite the tuning no better agreement was found. Therefore there is a problem in the simulation of the RPC response. Probably more sophisticated models are needed to simulate the RPC response. Remaining differences in the density distributions for data and simulation due to the imperfect tuning also explain the differences observed in the transverse shower profiles, as both measures are related.

8.2.2 Linearisation of the Electromagnetic Response

As explained in section 4.5, in general positrons and pions with the same energy will not produce the same number of hits and hit densities due to the invisible energy in hadronic showers. In imaging calorimeters software compensation algorithms can be applied to improve the energy resolution of hadrons [31]. The algorithms use information from the shower substructures to compensate fluctuations in the electromagnetic content of the hadronic showers. This has demonstrated significant improvement of the energy resolution [31].

Here a similar method is applied to the Min-DHCAL, where the detailed spatial information available is used to apply corrections to the measured number of hits. The method is designed to optimise the resolution and to linearise the positron response using a χ^2 function, see equation 8.5. The same method can then be applied to pions to re-weight

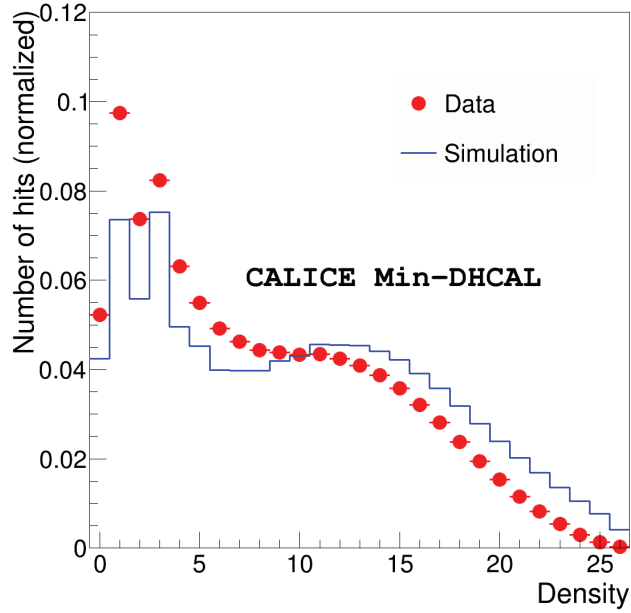


Figure 8.22: Distribution of the density of hits in events induced by 6 GeV positrons, data is plotted in red and simulation in blue. The error bars are smaller than the plotted data points. [41]

hits depending on their origin (electromagnetic or hadronic). This method is applied on top of leakage corrections described in chapter 8.2.1.

For the optimisation of the positron linearity a subsample is used, consisting of 8000 random events per beam energy. Every hit in this sample is weighted depending on their local density. The weights were determined by minimising the following χ^2 function:

$$\chi^2 = \sum_{i=1}^7 \left(\sum_{Events} \frac{\left(\sum_{j=0}^{26} w_j D_{ij} - \alpha E_i^{beam} \right)^2}{E_i^{beam}} \right); \quad (8.5)$$

where the first sum is over the different beam energies i . Each hit D_{ij} , collected at beam energy E_i^{beam} with a hit density j , is weighted by a factor w_j . α is an arbitrary hit to energy factor, here chosen as 90 hits/GeV, so that the linearised response intersects the unweighted response at 6 GeV. Choosing different values for the hit to energy factor resulted in similar results. The weights obtained by the linearisation procedure are shown

in figure 8.23 and can be seen to be large both for isolated hits and high densities. The large values of the weights related to higher densities compensates for the saturation effects introduced by the high density of electromagnetic showers and the finite pad size. The result of this linearisation procedure is shown in figure 8.11. The parameters of the various fits to power laws are summarised in table 8.1. The linearisation procedure significantly improves the linearity but still does not achieve a perfectly linear response.

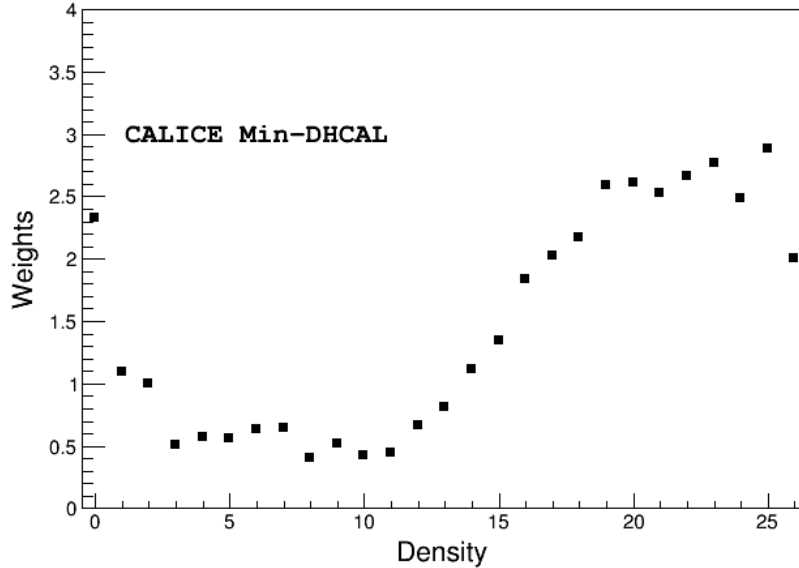


Figure 8.23: The electro-magnetic linearisation weights as a function of the number of neighbours in 3D for a given hit. [41]

Once the electromagnetic response is linearised, these weights can be applied to the pions and remaining positrons to improve the energy resolution. A significant improvement in the pion resolution, and to a lesser extent in the positron resolution, is expected using these weights.

In figure 8.24 the positron resolution is calculated for the subsample both before and after applying the linearisation weights. In table 8.3 the fit parameters are summarised. After linearisation the stochastic term α is reduced to 13.0%. The 6 GeV point seems anomalously high: this is attributed to statistical fluctuations.

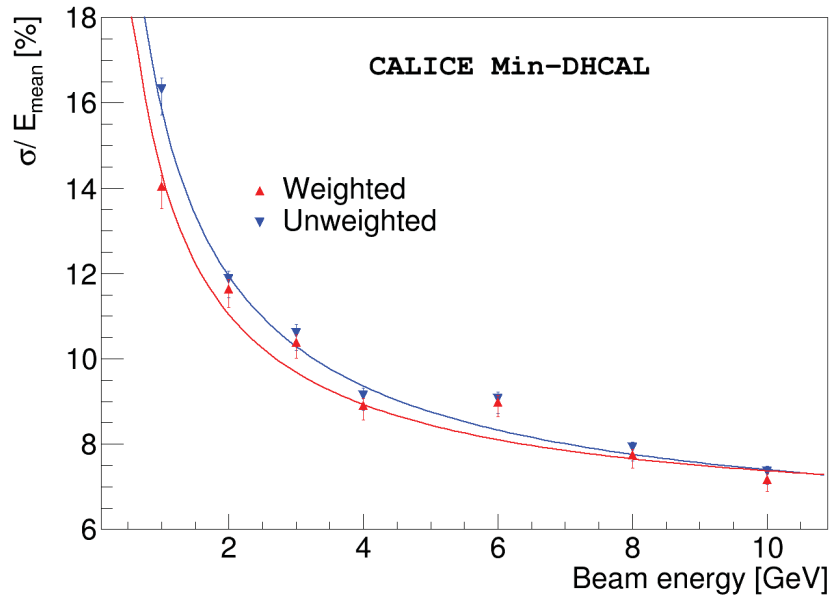


Figure 8.24: The positron resolution before (blue) and after (red) applying the linearisation weights. [41] Systematic errors are calculated according to section 7.6.

	α [%]	C [%]
Before linearisation	14.8 ± 0.4	5.7 ± 0.3
After linearisation	13.0 ± 0.4	6.2 ± 0.2

Table 8.3: Fit parameters for the constant and stochastic terms of the energy resolution for the positron subsample before and after linearisation.

8.2.3 Response to Muons

Muons at low energies act as minimum ionising particles, producing straight tracks in the detector, see also figure 7.2 which features 2 muon tracks. The comparison of the hit distributions of 10 GeV muons from data and simulation can be seen in figure 8.25. The asymmetric responses are not as well fitted by a Gaussian as for the positrons, therefore both responses are fitted by a so-called Novosibirsk function [55] in a 3σ range. It is defined as

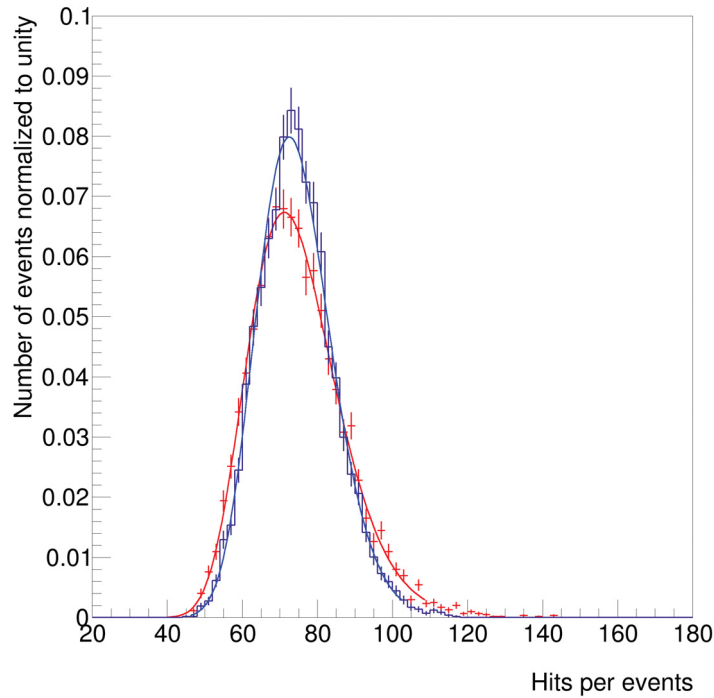


Figure 8.25: Hit distribution for both data (red) and simulation (blue) of 10 GeV muons. The distributions are fitted with a Novosibirsk function (see equation 8.6) plotted as a solid line.

$$F(x) = A \cdot e^{-0.5 \cdot \left(\frac{(\ln q)^2}{\Lambda^2} + \Lambda^2 \right)}, \quad (8.6)$$

where q is defined as:

$$q = 1 + \frac{\sin(\Lambda \sqrt{\ln 4})}{\sigma} \cdot \frac{\Lambda(x - x_0)}{\sigma}. \quad (8.7)$$

A , Λ , x_0 and σ are free parameters of the fit for the empirical function. Λ describes the tail of the distribution, x_0 gives the peak position, σ the width of the distribution and A the normalisation.

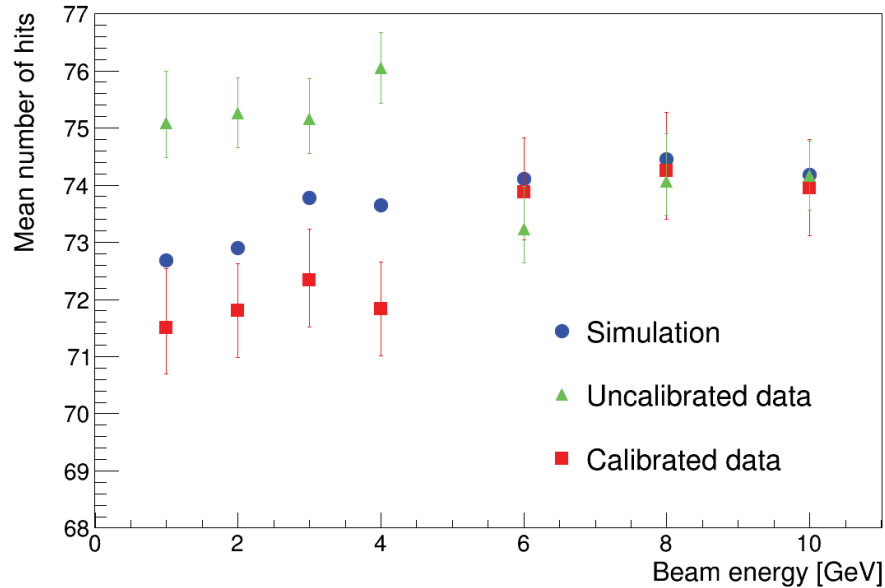


Figure 8.26: Mean response of muons versus beam energy for both calibrated data (red) uncalibrated data (green) and simulation (blue).

This function fits both the data and simulation distribution very well. To extract the mean response of muons, a histogram defined by the Novosibirsk fit is filled randomly and the mean and RMS of this distribution are calculated. With this method, tails in the distribution are included while outliers are disregarded [56]. In figure 8.26 the mean muon responses as a function of the beam energy of both data and simulation are shown. No systematic errors are assigned to the simulation (see section 7.6). The responses do not change significantly within the energy range analysed here. From figure 4.1, we expect a small rise in the energy loss of muons due to radiation effects. A 1% increase is expected going from 1 to 10 GeV, which is confirmed by the simulation. In the data there is a jump in the muon response between 4 and 6 GeV. The jump is observed both in the uncalibrated and calibrated data. The uncalibrated response is slightly higher for lower energies, whereas the calibrated data is significantly lower. A possible explanation is that operating conditions were slightly different for the lower energies and that the calibration is over compensating. In addition the pion contamination at low energies might shift the mean response. No satisfactory simple fix for this problem has been found yet, short of re-visiting the whole calibration procedure [57]. Apart from the differences observed at

low energies, the response for calibrated data and simulation agree reasonably well for higher energies.

Density of Muon Hits

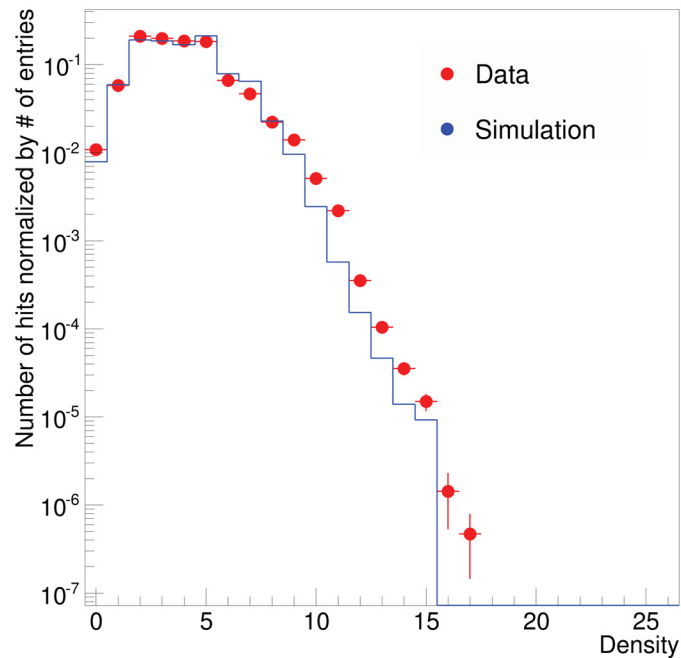


Figure 8.27: Distribution of the density of hits in events induced by 10 GeV muons, data is plotted in red and simulation in blue.

The density is determined the same way as for the positrons (section 8.2.1). The comparison between data and simulation is shown in figure 8.27. There is a good agreement between data and simulation, which is expected since most of the parameters are tuned using muons, and the agreement is much better than for the positrons.

Longitudinal and Transverse Shower Profiles

The shower axis is identified in the same way as for the positrons and the transverse distribution of hits is calculated. As the muons leave very clean and straight tracks in the detector, apart from occasional scattering, all layers can be used to determine the shower

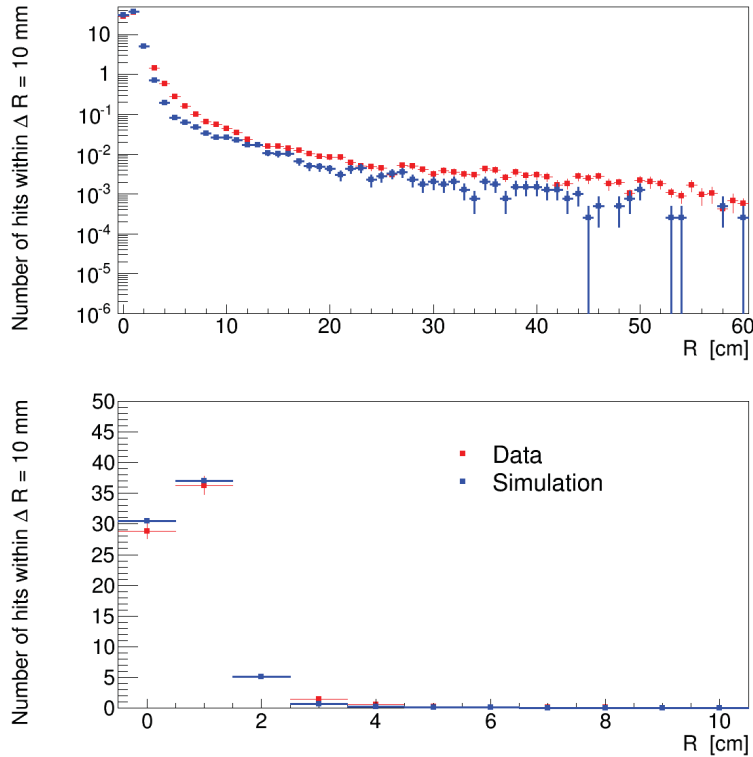


Figure 8.28: Distribution of the radial distance of hits for 10 GeV muons. The upper (lower) plot uses a logarithmic (linear) y-scale. The entries in both plots are normalised to unity.

axis, however only the first 20 layers are used, as this proved to be sufficient to obtain a good fit. The distribution of the radial distance of hits for 4 GeV muons is shown in figure 8.28. The first few bins, which contain the vast majority of hits are very well reproduced by the simulation. As muons produce no showers, the radial profiles decrease very rapidly. Hits with $R > 20$ cm are mostly isolated noise hits. The number of hits with $R > 20$ cm is consistent with the estimated noise rate of 0.2 hits/per event. Noise was added to the simulation to reproduce the tail. With the simulated noise, data and simulation agree reasonably well. Hits with $R > 20$ are observed at a slightly higher rate in the data, suggesting that the noise rate was not perfectly simulated. Remaining differences in the transverse profiles can also originate from pion contamination. However, the pion contamination does not seem to change the shower shape significantly, as differences between data and simulation are measured to be small for all energies.

The longitudinal shower profile of 6 GeV muons can be seen in figure 8.29, the response is flat over all layers, with about 1.5 hits per layer in average. This shows that muons act as MIPs and leave without being completely stopped. A very good agreement between data and simulation is observed. Layer 39 features a dead ASIC sitting in the middle of

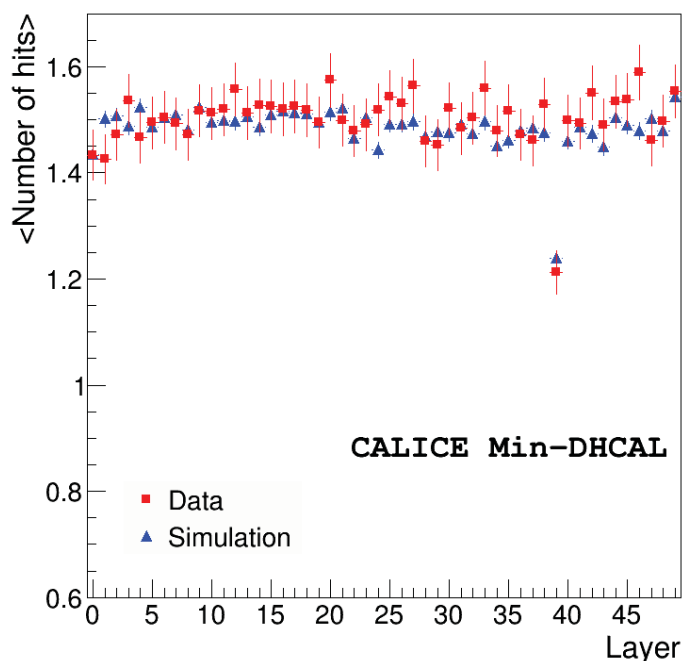


Figure 8.29: Measurement of the longitudinal distribution for 6 GeV muons, i.e. the average number of hits as a function of layer number. The data (red) are compared to the results of simulation (blue histogram).

the detector, where most particles cross. This causes a lack of recorded hits compared to other layers. As the corresponding areas were also removed in the simulation a good agreement is also obtained for this layer despite the dead area. The calibration of data and the tuning of the simulation seem to work well for muons.

8.2.4 Response to Pions

Pions travel through several layers ionising the gas before interacting hadronically, creating large hadronic showers. Before the interaction layer, the pion response is very similar to a Minimum Ionising Particle (MIP), they produce narrow minimum ionising tracks featuring only a few hits per layer. Energy leakage is important for pions in the minimal absorber configuration despite selecting pions which have their interaction layer in the first 10 layers. Two examples of the pion response at 6 and 10 GeV are shown in figure 8.30. The hit distributions are broad as there is a large fluctuation in the deposited energy due to the nature of hadronic interaction and leakage. A simulation using the FTFP_BERT physics list is also included in the figures. The simulation shows a larger tail towards

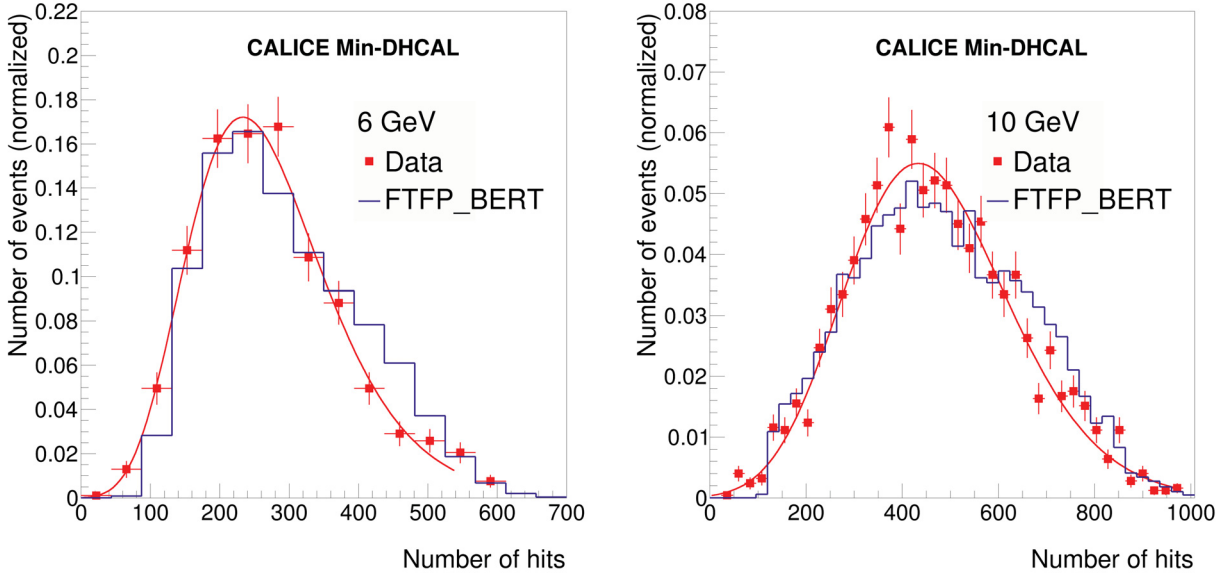


Figure 8.30: Hit distributions for both data (red) and simulation (blue) for 6 GeV (left) and 10 GeV (right) pions. The distributions are fitted with a Novosibirsk function (see equation 8.6) plotted as a solid line. [58]

larger number of hits.

As the responses are not very well fitted by a Gaussian function, the same Novosibirsk fit as in the case of muons is used (see equation 8.6). This function fits the responses well. Once again the fit is used to determine the mean response. The resulting mean as a function of the beam energy for both data and simulations can be seen in figure 8.31.

	m	b
Fe-DHCAL Data	1.00 ± 0.01	14.4 ± 0.1
Min-DHCAL Data	1.02 ± 0.04	43.3 ± 3.2
Simulation	1.03 ± 0.01	43.6 ± 0.1

Table 8.4: Fit parameters for the exponent m and the constant b of the power law fit (see equation 8.1) measured in the Fe-DHCAL (taken from figure 8.6a)), the Min-DHCAL and in simulation.

As described in section 7.5, different shower models can be tested by using different physics lists implemented in GEANT4. The standard FTFP_BERT simulation with its associated systematic errors are shown in blue along with other simulations using different physics lists. These are QGSP_FTFP_BERT (turquoise), QGSP_BIC (black) and

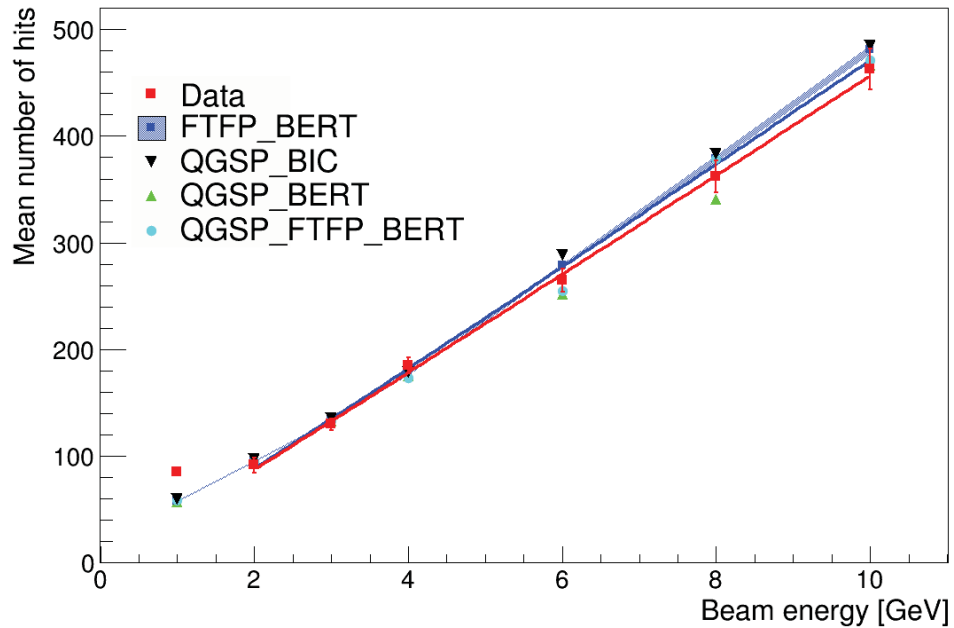


Figure 8.31: Mean response of pions versus beam energy for both data (red) and simulations are shown. Different physics lists are shown along the standard FTFP_BERT in blue which features the systematic errors of the simulation (blue area). Data and the FTFP_BERT simulation are fitted in the range of 2-10 GeV with a power law shown as solid lines. [58]

QSPS_BERT (green). A good agreement is observed between data and simulations for all energies except 1 GeV. The beam at this energy has only a very small fraction of pions in it, as can be seen in table 7.3. Therefore even if the contamination from muons and positrons is small in general, it will dominate the response at 1 GeV, shifting up the response. Both data and the FTFP_BERT simulation responses are fitted with a power law function. The 1 GeV point is excluded from the fit due to the high level of contamination. The fit parameters are summarised in table 8.4, a good agreement between data and simulation is observed. The response is nearly linear for the given energy range, as the exponent m is equal to one within the errors. Compared to the Fe-DHCAL, which also showed a linear response, a factor of 2.7 more hits per GeV are measured with the Min-DHCAL.

To compare different hadronic shower models, the ratio of data and simulation is calculated. The results are summarised in figure 8.32. For 2, 3, and 4 GeV all physics lists use the Bertini Cascade model except QGSP_BIC which uses Binary cascades (BIC) for all energies below 10 GeV. The difference between these two seems to be small and

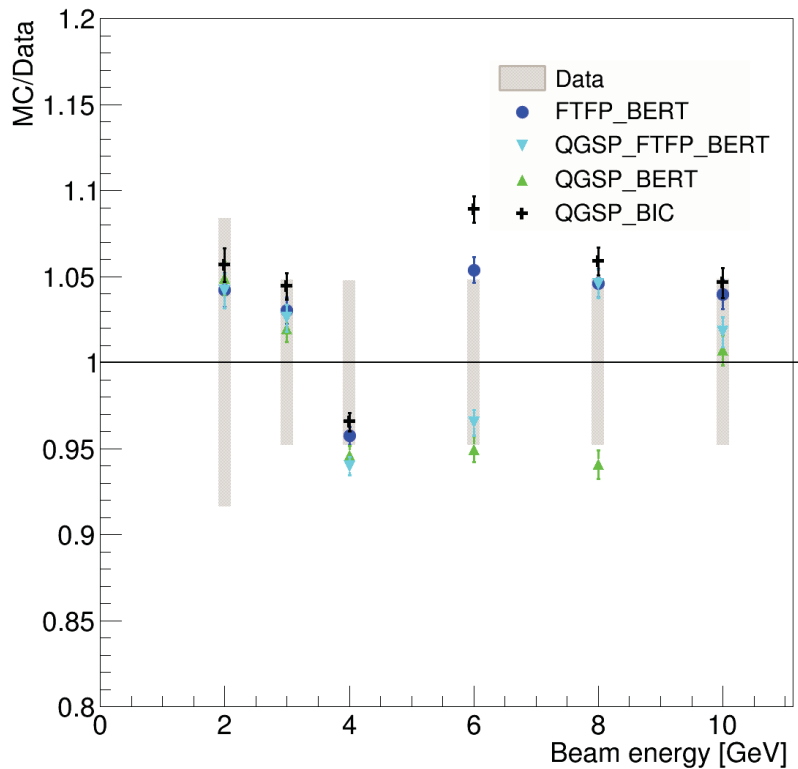


Figure 8.32: The ratio of the pion responses for simulations with different hadronic shower models and data shown for energies of 2 to 10 GeV. Systematic and statistical errors of the data are shown as grey bands. [58]

all simulation are inside the systematic error of the data. The response of 4 GeV pions in data is slightly above the fit, which will shift the simulations down in the ratio plot. However at 6 GeV some physics lists transition to another model describing the hadronic interaction (see section 7.5). QGSP_FTFP_BERT and QGSP_BERT uses Bertini whereas FTFP_BERT transitions to FTFP (see figure 7.11). A significant difference between these two models is observed. FTFP and BIC produce too many hits (5 to 10 % more than data) whereas Bertini produces too few (about 5 %). No model seems to perfectly match the data. BIC shows the biggest difference and Bertini is closer to the data than FTFP. At 8 GeV QGSP_FTFP_BERT and FTFP_BERT uses FTFP, QGSP_BERT uses Bertini. Both the BIC and FTFP model are inside the systematic errors whereas Bertini produces less hits than observed in the data. At 10 GeV all physics lists uses FTFP except QGSP_BERT which uses the LEP model. All models are inside the systematic error at this energy.

Using the inverse of the fit function of the pion response, see figure 8.31, the energy

can be reconstructed. The reconstructed pion energy distributions with beam energies of 4, 6, 8 and 10 GeV are shown in figure 8.33. Simulations using different physics lists are included as well as a Novosibirsk fit to the data. As for the hit distribution, the energy distributions are broad due to the nature of hadronic interactions. The energy distributions for the pion data have relatively low statistics for 4 GeV. QGSP_BERT does not reproduce the simulated distributions very well for 8 and 10 GeV, it shows a large tail towards higher energies which is not present in the data.

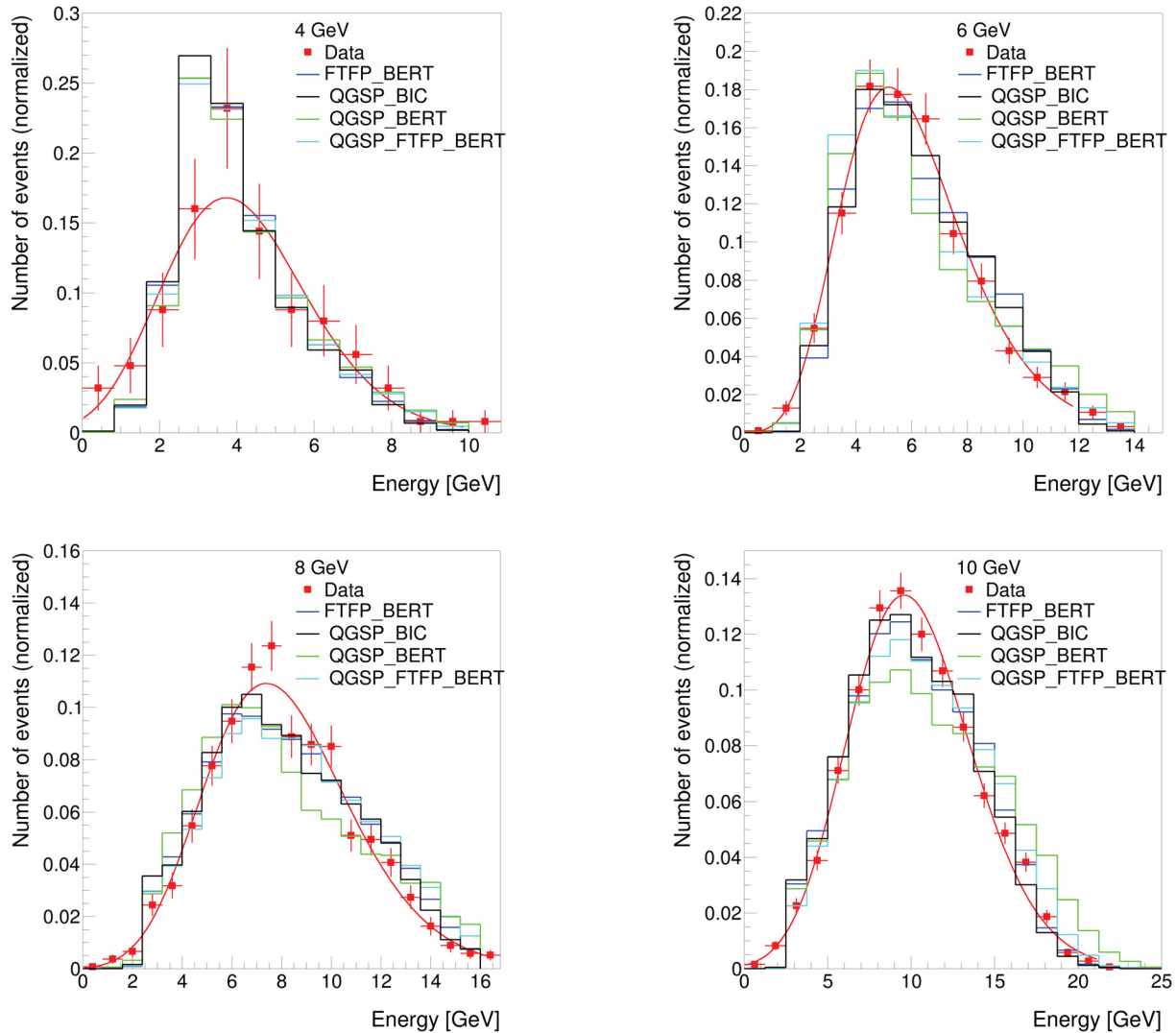


Figure 8.33: Reconstructed pion energy distributions for both data (red) and simulation generated using different physics lists for pions with beam energies of 4, 6, 8 and 10 GeV. The data distributions are fitted with a Novosibirsk function plotted as a solid line. [58]

Figure 8.34 shows the resulting resolution using the RMS and mean value of the fit as function of beam energy for both data and simulation using different physics lists. The

resolution is degraded by the large fraction of energy loss due to leakage, which is not corrected for pions. The resulting energy resolution is therefore nearly flat when plotted against the beam energy. There is a reasonable agreement between data and simulations except for 4 GeV. The FTFP_BERT simulation results in a better energy resolution than observed in the data and the other physics lists. Because of the large degradation due to leakage no improvement was observed when applying the linearisation weights obtained in section 8.2.2. The leakage can be corrected in average as for the positrons, however the amount of leakage is subject to large fluctuations. Those fluctuations degrade the resolution so the leakage would have to be corrected event by event, which is hardly possible.

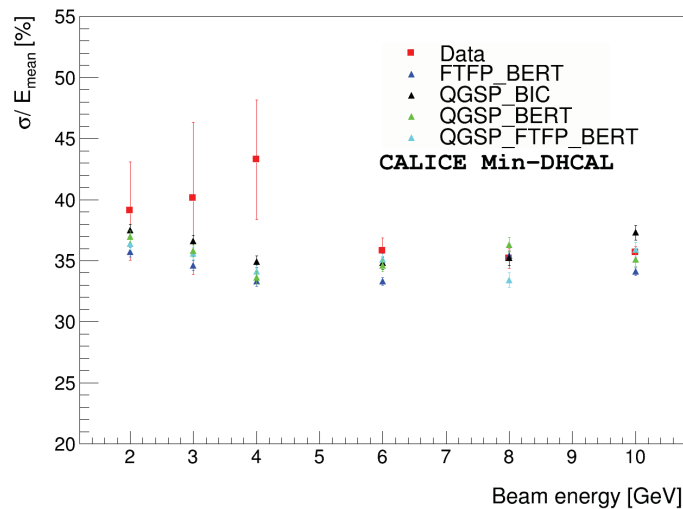


Figure 8.34: Pion energy resolution as a function of the beam energy for data and simulation generated using different physics lists.

Density of Pion Hits

The hit density is determined in the same way as for the other particles. The results for 3, 6 and 10 GeV pions are shown in figure 8.35, data points in red, the FTFP_BERT simulation in blue dots with their associated systematic error shown as blue shades. Simulations with different physics lists are also included. The systematic errors associated with the pion simulation are big as large differences between the positron data and simulation were observed despite the tuning (see section 8.2.1). The error associated with the simulation is given by the average difference between these two. Differences between models are small and well inside the systematic errors of the simulation (see section 7.6). There is a

good agreement observed for 3 GeV but not for 6 and 10 GeV. The shape of the density distribution changes significantly for higher energies. The tail for higher densities rises in simulation. The data does not show the same behaviour. None of the different physics lists describes the data well for 6 and 10 GeV.

Longitudinal and Transverse Shower Profiles

To define the shower axis, all hits in the layers before the interaction layer, corresponding to the MIP track, are used to apply a linear fit. The same requirements on the fit as for the positrons are also applied to pions (see section 8.2.1). Three examples of transverse shower profiles for 3, 6 and 10 GeV are shown in figure 8.36 for both data and simulations. In the bottom part of the plots the ratio between data and simulations is shown. A good agreement is observed for all physics lists at 3 GeV, the differences are within the systematic errors associated with the simulations. For 6 GeV small differences are visible between the FTFP and BERT models, however again none of the models matches the data at 6 and 10 GeV.

Apart from these comparisons to simulations, the transverse profiles of the different particle types can also be compared. The transverse profiles of muons, positrons and pions can be found in figure 8.37. The particles have distinct shower shapes. Pion showers are broader and less dense than positron showers. Muons mostly do not shower and have narrow distributions.

The position of the interaction layer varies from event to event. In order to analyse the longitudinal shower profile, the average number of hits is plotted against the number of layers from the interaction layer. In figure 8.38 the longitudinal shower profiles for 3, 6 and 10 GeV pion events is shown. Pions act as MIPs before the interaction layer. The response in the MIP-section is actually slowly rising, which is also seen in the simulation. For the first few layers the response of the pions is equivalent to the muon response producing ≈ 1.5 hits per layer. The response rises up to 2 hits per layer close to the interaction layer. Beginning with the interaction layer a sharp rise in the average number of hits is observed. Similar to the gamma distribution fit for electromagnetic shower profiles (see equation 4.13), the longitudinal profiles of pions are fitted with a sum of two gamma distributions [59], see equation 8.8. The parametrisation has a "short" and "long" component, corresponding to the electromagnetic (short) and hadronic (long) interaction:

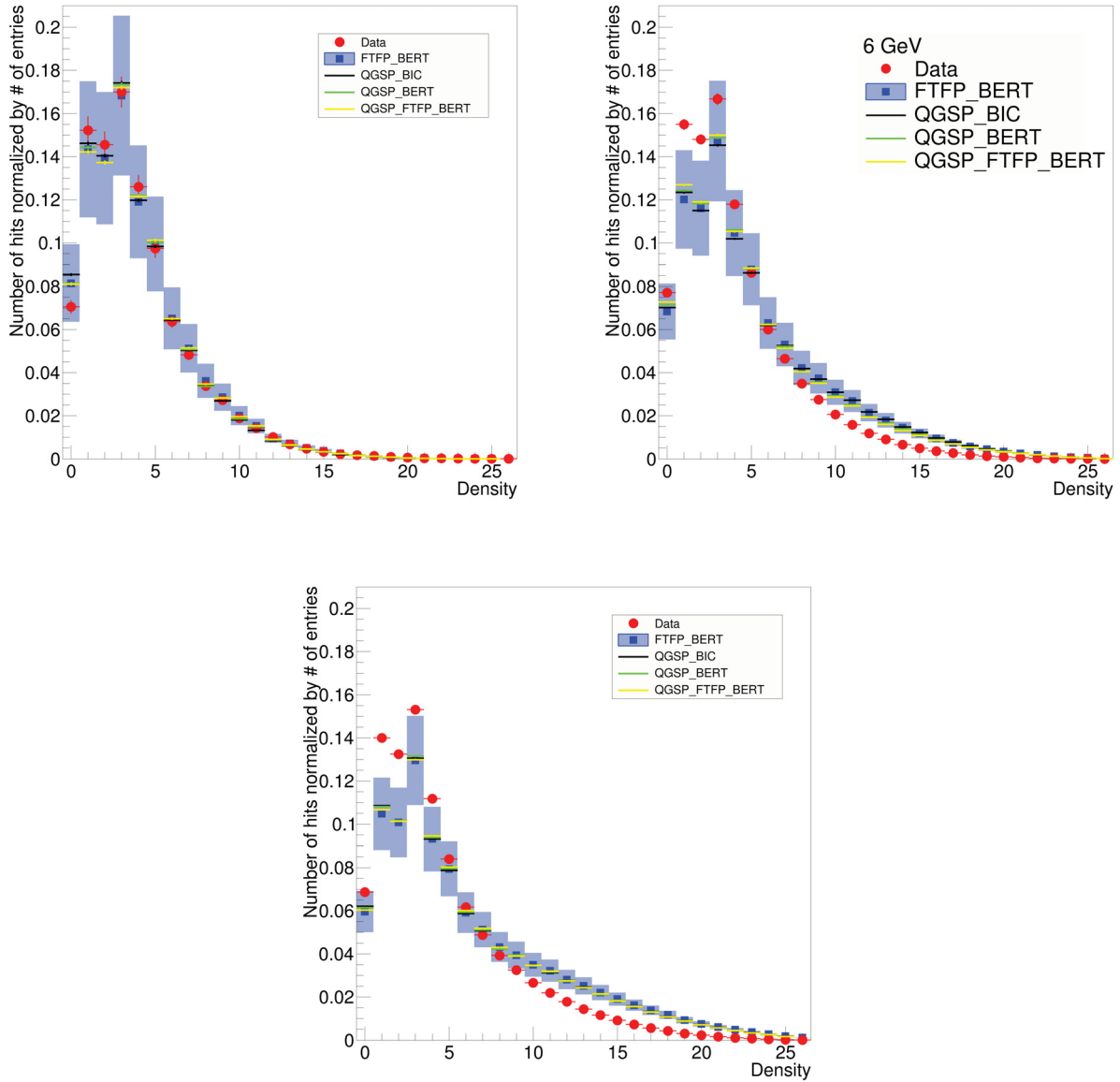


Figure 8.35: Distribution of the density of hits in events induced by 3 GeV (left) and 10 GeV (right) pions, data is plotted in red and simulation in blue. The error bars are smaller than the plotted data points, systematic errors of the simulation are shown as blue boxes. [58]

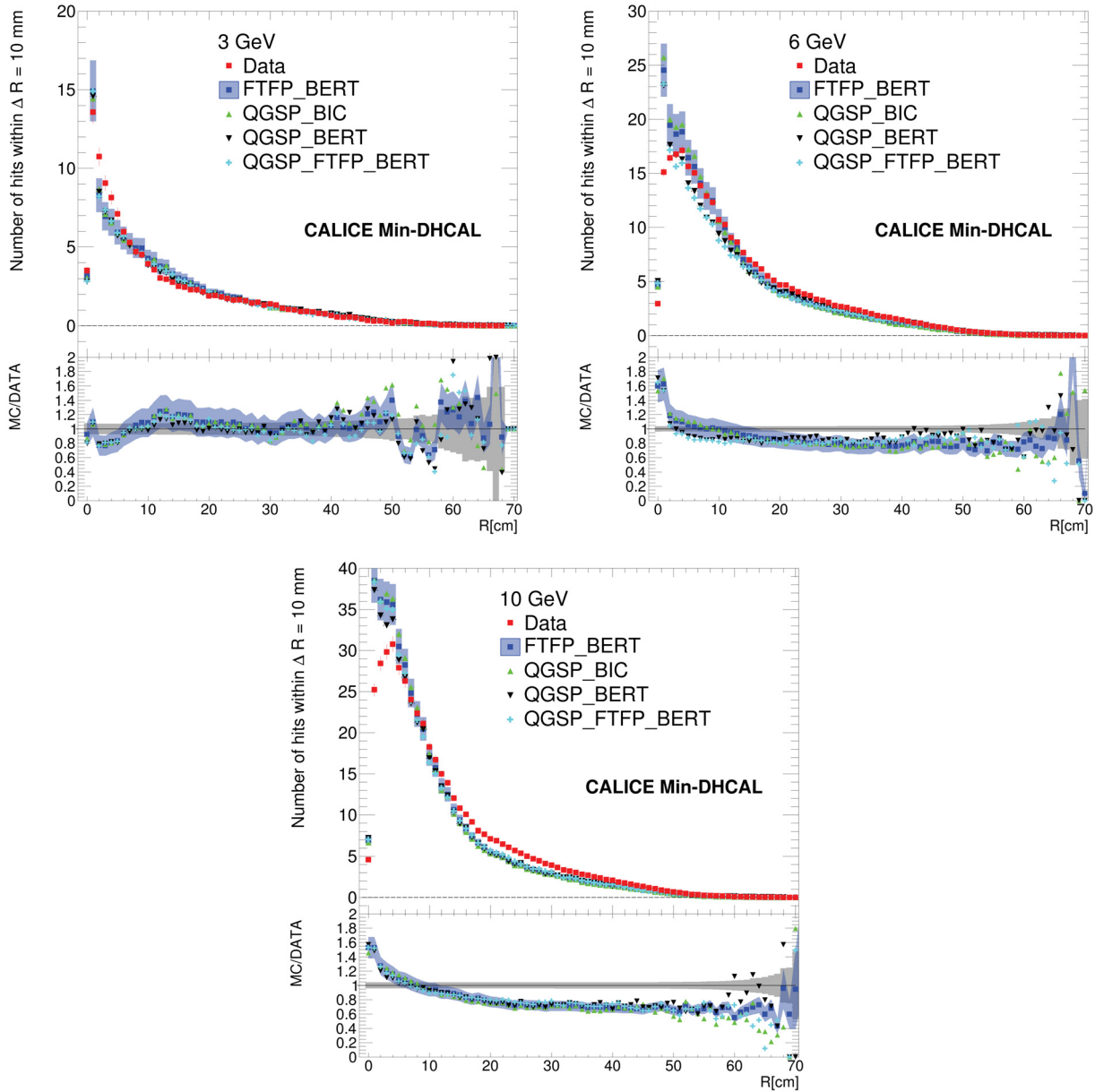


Figure 8.36: Distribution of the radial distance of hits from the shower axis for 3 GeV (top left), 6 GeV (top right) and 10 GeV (bottom) pions. The profiles are shown in a linear scale (top) and as a ratio between data and simulations (bottom). The areas in both plots are normalised to one event. Data and simulation using different physics lists are shown. The standard FTFP_BERT simulation is plotted in blue featuring the systematic error of the simulation (blue area). In the ratio plot the systematic errors of the data are shown in grey. [58]

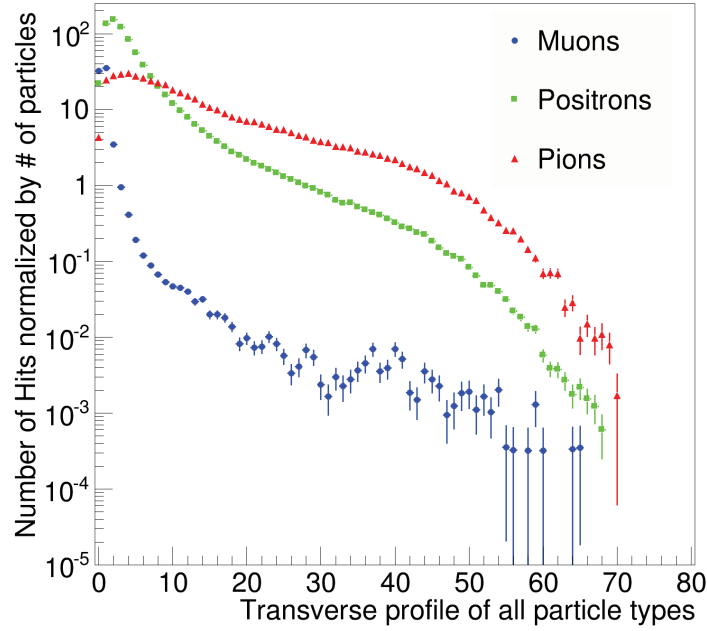


Figure 8.37: Distribution of the radial distance of hits from the shower axis for 10 GeV muons (blue), positrons (green) and pions (red).

$$\frac{dE}{dt} = A \cdot \left(f \cdot \beta_{short} \frac{(\beta_{short} t)^{\alpha_{short}-1} e^{-\beta_{short} t}}{\Gamma(\alpha_{short})} + (1 - f) \cdot \beta_{long} \frac{(\beta_{long} t)^{\alpha_{long}-1} e^{-\beta_{long} t}}{\Gamma(\alpha_{long})} \right) ; \quad (8.8)$$

where A is a scaling factor, f the fractional contribution of the "short" component and $\alpha_{short (long)}$ and $\beta_{short (long)}$ are the slope parameters of the short (long) component.

The fit in figure 8.38 describes both the data and the simulation well. Once again there is a good agreement at 3 GeV but some significant differences for 6 and 10 GeV. In the simulation there are hits in the last layers. The shower maximum is calculated using the fit. The values for both data and simulation are summarised in table 8.5. Only for beam energies 4 to 10 GeV is a shower maximum observed after the interaction layer. Except for 4 GeV, where the position for the shower maximum agrees for data and simulation, the shower maximum seems to occur around 1-2 layers later for the simulation.

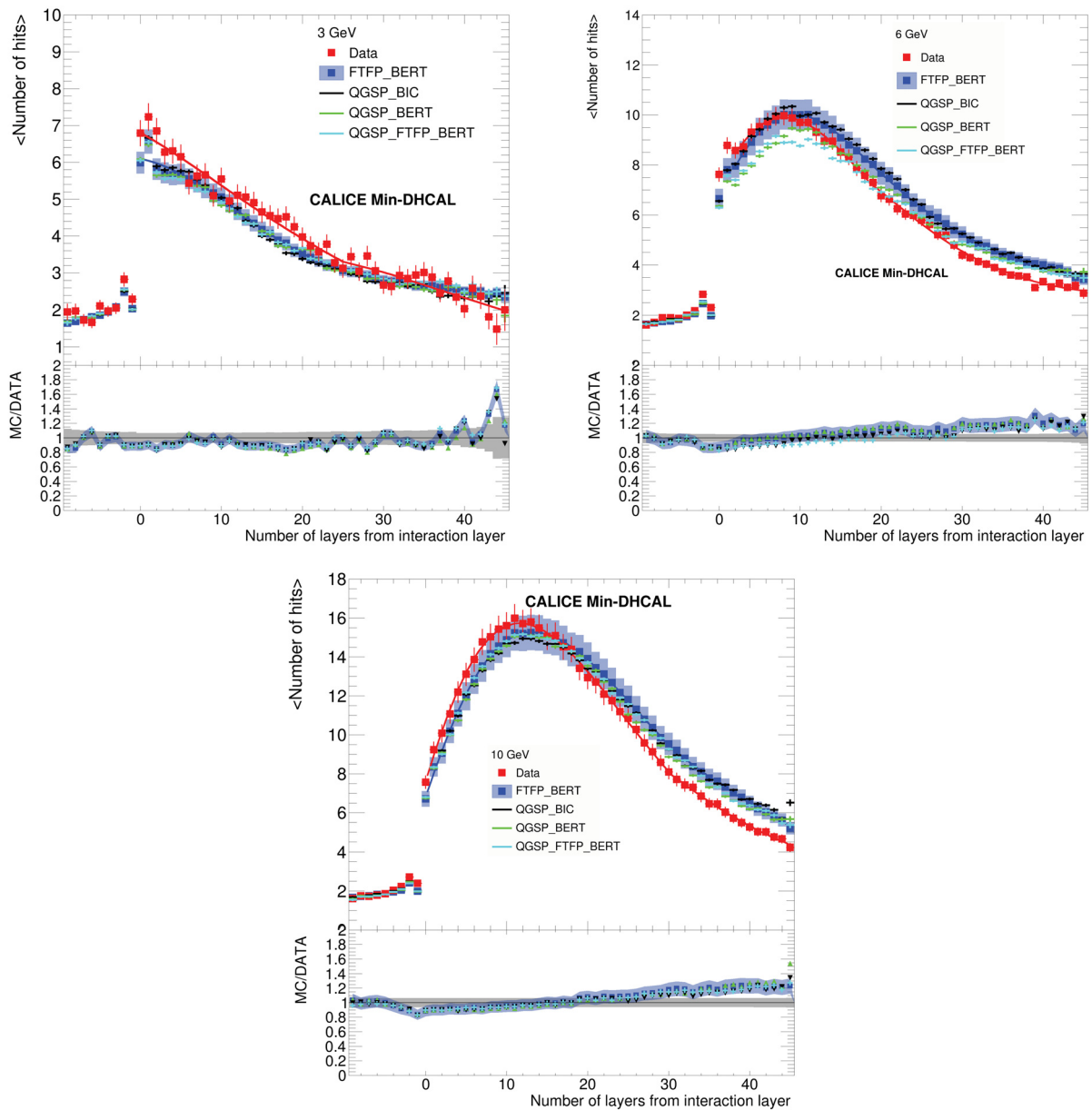


Figure 8.38: Measurement of the longitudinal distribution for 3 GeV (top left), 6 GeV (top right) and 10 GeV (bottom) pions. The data (red) are compared to the results of simulations. Different physics lists are shown along the standard FTFP_BERT in blue which features the systematic error of the simulation (blue box). Both profiles are fitted to a double gamma distribution function plotted as a solid line. [58]

Momentum [GeV]	4	6	8	10
Shower max. data [layer]	5.3±0.1	7.7±0.1	9.9±0.1	11.6±0.1
Shower max. simulation [layer]	5.1±0.1	9.0±0.0	11.6±0.1	13.2±0.1

Table 8.5: Shower maximum of pions obtained from the fits in figure 8.38.

Nuclear Interaction Length

Using the position of the interaction layer, the nuclear interaction length can be calculated for both data and simulation. In figure 8.39 the position of the interaction layer for 6 to 10 GeV pion events is shown. Both are fitted to an exponential similar to equation 4.9 of the form

$$F(x) = N_0 e^{-\lambda_l x} . \quad (8.9)$$

The exponent λ_l of this fit is an approximation for the nuclear interaction length per layer, x is the layer number. Values obtained are $\lambda_l = 0.037 \pm 0.001$ per layer and $\lambda_l = 0.043 \pm 0.001$ per layer for data and simulation respectively. A rough estimation of the nuclear interaction length using the known absorber structure predicted a value of $\lambda_l = 0.037$ per layer, which agrees well with the data. The large scattering observed for the data is caused by uncertainties in the equalisation of the response. Disagreements can be caused by a wrong implementation of the absorber structure, by deficiencies in simulating the RPC response or by amplification of the fluctuations of the equalisation procedure. The Cherenkov counters and the scintillator pads are not included in the simulation. However, the Cherenkov counters only add a negligible amount of material and the scintillator pads add about 1 cm of plastic, which is negligible compared to the whole detector, which features in total 5 cm of both copper and steel plates. The only inhomogeneities in the RPCs come from the DCAL chips. The effect is small as the additional material adds only 1% to the radiation length of one layer (see section 6.2). However the effect is somehow accentuated by the fact that all chips are aligned in x and y . These inhomogeneities are currently not implemented in the simulation and explain some of the differences observed between data and simulation.

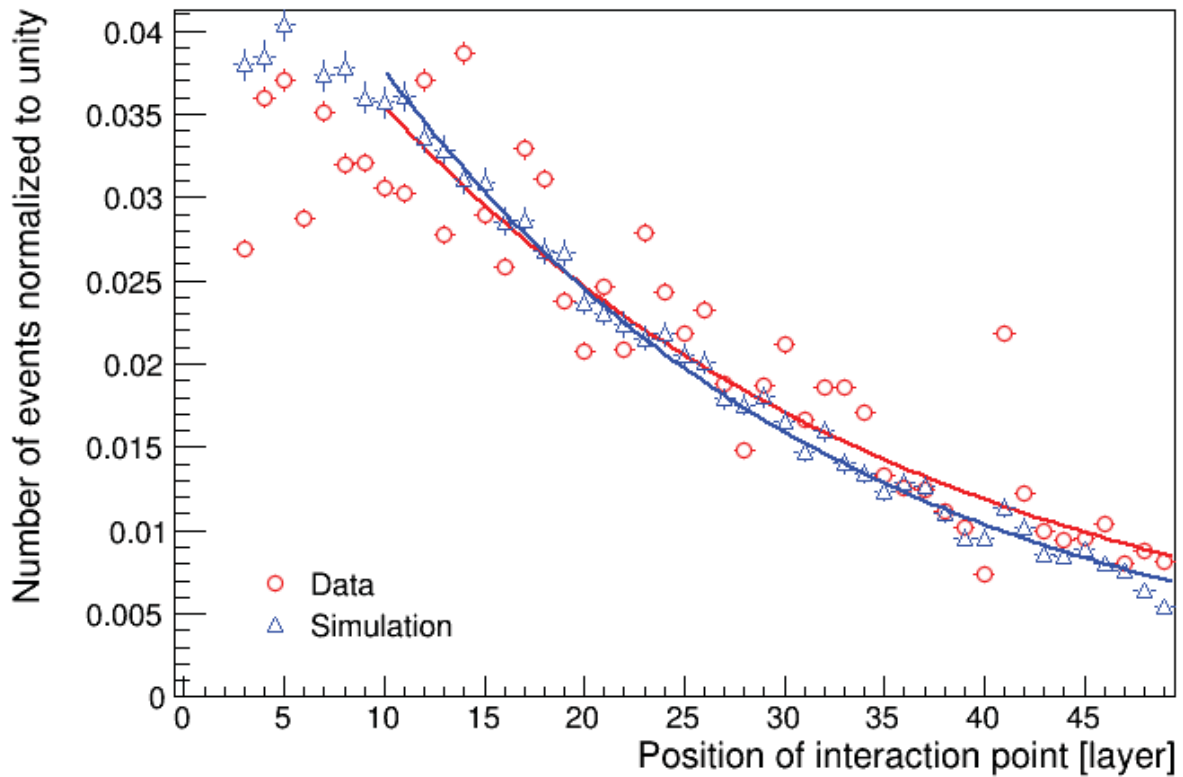


Figure 8.39: Position of the interaction layer for 6 to 10 GeV pions for both data (red) and simulation (blue). Both are normalised to unity. Points are fitted to an exponential (see equation 8.9).

Chapter 9

Discussion and Conclusion

Test beam data taken in November 2011 at Fermilab with the DHCAL with minimal absorber structure was analysed. The equalisation method based on muon data was explained and tested. More sophisticated equalisation methods are currently being developed, which might improve the response of the detector. The energy resolution of positrons and pions in this minimal absorber configuration is determined and compared to results obtained with steel absorber structure. A very good energy resolution is obtained for positrons. Pions however suffer from high leakage which limits the resolution in the minimal absorber configuration. Positron and pion showers are spread over the whole detector allowing detailed shower analysis and comparisons to simulation. The highly segmented calorimeter allows leakage correction which improves both the linearity and the resolution. With the leakage correction a stochastic term of 14.2% for positrons is obtained using the standard parametrisation of the resolution.

Some issues are seen in the tuning process of the simulation. Some properties of the positrons, e.g. the hit density, can not be reproduced properly in the simulation, even though the parameters are specifically tuned to minimise differences between simulation and data for these measurements. More work is required in developing more sophisticated programs simulating the Resistive Plate Chamber response. Muons are easier to simulate and most of the parameters are tuned to the muon data. A good agreement between data and simulation is observed as expected.

The pions are compared to different physics lists implemented in GEANT4. It is shown

that generally the differences between different models are quite small compared to the general discrepancy between data and simulation. Significant changes in the simulations are seen going from low (3 GeV) to higher energies (10 GeV), which are not validated by the data. Good agreement is obtained with the Bertini model for energies below 4 GeV. For higher energies, no model describes the data well, 10 % deviations are seen for example in the pion hit density distributions for 10 GeV.

It is shown that the density information of the hits can be used as a software compensation to linearise the electromagnetic response of the detector. Once the response is linearised an energy resolution relatively improved by 10% for positrons is observed. However, due to low energies and low statistics no improvement of the hadronic energy resolution was observed yet, which should be the ultimate goal of the software compensation method.

It has been demonstrated that the DHCAL with minimal absorber structure is ideal to test the detector and to validate current hadronic shower models. More data and work are required to optimise the tuning process, which would allow definitive answers on the performance of the various hadronic shower models. This would provide necessary feedback for the developers of the simulation software GEANT4.

Bibliography

- [1] S. Weinberg: *Conceptual foundations of the unified theory of weak and electromagnetic interactions*, Rev. Mod. Phys. 52, 515, 1 July 1980
- [2] MissMJ: *Standard Model of Elementary Particles*, (2006), date retrieved (2014), available from: http://en.wikipedia.org/wiki/File:Standard_Model_of_Elementary_Particles.svg
- [3] M.C. Gonzalez-Garcia, Michele Maltoni: *Phenomenology with Massive Neutrinos*, arXiv:0704.1800v2, 16 Oct 2007
- [4] C. Burgess and G. Moore: *The Standard Model: A Primer*, Cambridge University Press, revised first edition (2013), page 393 onwards
- [5] V.C. Rubin, W.K. Ford Jr.: *Rotation of the Andromeda Nebula from a Spectroscopic Survey of Emission Regions*, Astrophysical Journal, vol. 159 (1970), page 379 onwards
- [6] S. Dodelson and L. M. Widrow: *Sterile neutrinos as dark matter*, Phys. Rev. Lett. 72, 17, 3 January 1994
- [7] P. J. E. Peebles, B. Ratra: *The Cosmological Constant and Dark Energy*, arXiv:astro-ph/0207347v2, 20 Nov 2002
- [8] C. Burgess and G. Moore: *The Standard Model: A Primer*, Cambridge University Press, revised first edition (2013), page 436 onwards
- [9] H. Pagels and J. R. Primack: *Supersymmetry, Cosmology, and New Physics at Teraelectronvolt Energies*, Phys. Rev. Lett. 48, 223, 25 January 1982
- [10] S. Raby, Particle Data Group, *Hypothetical particles and Concepts*, data retrieved: (2014), available from: <http://pdg.lbl.gov/2014/reviews/rpp2014-rev-guts.pdf>

- [11] T. Behnke et al.: *The International Linear Collider: Technical Design Report 2013*, (2013), available from: <http://www.linearcollider.org/ILC/Publications/Technical-Design-Report>
- [12] The CMS Collaboration: *The CMS Particle Flow Algorithm*, arXiv:1401.8155, April 2013
- [13] B. Levesy et al.: *CMS Solenoid Assembly*, IEEE, Volume 16, Issue 2, pp. 517 - 520, June 2006
- [14] T. Behnke et al.: *GEM module design for the ILD TPC*, JINST 8 C10010, doi:10.1088/1748-0221/8/10/C10010 (2013)
- [15] C. Grupen and B. Shwartz: *Particle Detectors*, Cambridge University Press, Second Edition, Chapter 1 pages 1-49 (2008)
- [16] Particle Data Group: *Passage of particles through matters*, (2014), date retrieved (2014), available from: <http://pdg.lbl.gov/2014/reviews/rpp2014-rev-passage-particles-matter.pdf>
- [17] C. Grupen and B. Shwartz: *Particle Detectors*, Cambridge University Press, Second Edition (2008), pages 231 onwards
- [18] K.A. Olive et al. *Particle Data Group*, Chin. Phys. C. 38, 090001 (2014), Section 32, p. 27
- [19] C. Grupen and B. Shwartz: *Particle Detectors*, Cambridge University Press, Second Edition (2008), pages 242 onwards
- [20] The CALICE Collaboration: *DHCAL Response to Positrons and Pions*, CALICE Analysis Note CAN-032, March 2011
- [21] B. Bilki, J. Repond, L. Xia: *Development of Imaging Calorimetry*, arXiv:1308.5929, 27 Aug 2013
- [22] M. A. Thomson: *Particle Flow Calorimetry and the PandoraPFA Algorithm*, arXiv:0907.3577, 21 Jul 2009
- [23] J. C. Brient and H. Videau: *The calorimetry at the future e^+e^- linear collider*, Proceedings of the APS/DPF/DPB Summer Study on the Future of Particle Physics (Snowmass 2001), arXiv:hep-ex/0202004 v1 2001, Second Edition (2008)

- [24] <https://twiki.cern.ch/twiki/bin/view/CALICE/WebHome>
- [25] J-C Brient et al., *CALICE Report to the Calorimeter R&D Review Panel*, (2007), arXiv:0707.1245
- [26] The CALICE collaboration et al: *Design and electronics commissioning of the physics prototype of a Si-W electromagnetic calorimeter for the International Linear Collider*, JINST 3 P08001, doi:10.1088/1748-0221/3/08/P08001 (2008)
- [27] C. Adloff et al.: *Response of the CALICE Si-W electromagnetic calorimeter physics prototype to electrons*, Nucl. Instrum. Meth, Volume 608, Issue 3, 21 September 2009, pages 372383
- [28] K. Francis et al: *Performance of the first prototype of the CALICE scintillator strip electromagnetic calorimeter*, Nucl. Instrum. Meth, Volume 763, 1 November 2014, pages 278289
- [29] T. Price et al.: *First radiation hardness results of the TeraPixel Active Calorimeter (TPAC) sensor*, JINST 8 P01007, doi:10.1088/1748-0221/8/01/P01007 (2013)
- [30] The CALICE collaboration et al.: *Construction and commissioning of the CALICE analog hadron calorimeter prototype*, JINST 5 P05004, doi:10.1088/1748-0221/5/05/P05004 (2010)
- [31] The CALICE Collaboration: *Hadronic energy resolution of a highly granular scintillator-steel hadron calorimeter using software compensation techniques*, JINST 7 P09017 (2012)
- [32] The CALICE collaboration et al.: *Results of the SDHCAL technological prototype*, arXiv:1403.8097 (2013)
- [33] C. Adloff et al.: *Beam test of a small MICROMEGAS DHCAL prototype*, JINST 5 P01013, doi:10.1088/1748-0221/5/01/P01013 (2010)
- [34] G. Drake et al.: *Resistive Plate Chambers for hadron calorimetry: Tests with analog readout*, Nucl. Instrum. Meth, Volume 578, Issue 1, 21 July 2007, pages 88-97
- [35] The CALICE Collaboration *Construction of the Digital Hadron Calorimeter*, arXiv:1202.6080 (2012)
- [36] B. Bilki, B. Freund et al.: *Tests of a Novel Design of Resistive Plate Chambers*, JINST 10 P05003 (2015)

- [37] B. Bilki et al.: *Tests of a Digital Hadron Calorimeter*, J. Phys.: Conf. Ser. 293 012075 (2011)
- [38] The CALICE Collaboration: *Analysis of DHCAL Muon Data*, CALICE Analysis Note CAN-030, March 17 (2011)
- [39] J. Hoff et al.: *DCal: A Custom Integrated Circuit for Calorimetry at the International Linear Collider*, IEEE Nucl. Sci. Symp., Puerto Rico, 2005, FERMILAB-CONF-05-509
- [40] <http://ppd.fnal.gov/ftbf/beam/energies.html>, date retrieved May
- [41] B. Bilki, B. Freund et al.: *DHCAL with Minimal Absorber: Measurements with Positrons* (paper in preparation)
- [42] B. Bilki: *The CALICE DHCAL: Results from Fermilab Data*, (2013), date retrieved (2014), available from: <https://twiki.cern.ch/twiki/bin/view/CALICE/CHEF2013> 2015
- [43] D. Trojand: *A Novel Digital Hadron Calorimeter: Analysis and Calibration with Muons*, Master of Science Thesis, McGill University (2012)
- [44] B. Bilki et al.: *Environmental dependence of the performance of resistive plate chambers*, JINST 5 P02007, doi:10.1088/1748-0221/5/02/P02007 (2010)
- [45] The CALICE Collaboration: *The DHCAL Results from Fermilab Beam Tests: Calibration*, CALICE Analysis Note CAN-042, May 2013
- [46] S. Agostinelli et al.: *GEANT4-a simulation toolkit*, Nucl. Instrum. Meth, Volume 506, Issue 3, 1 July 2003, Pages 250303
- [47] B. Bilki et al.: *Measurement of positron showers with a digital hadron calorimeter*, JINST 4 P04006 (2009)
- [48] http://geant4.cern.ch/support/proc_mod_catalog/physics_lists/referencePL.shtml, data retrieved June 2015
- [49] C. Adloff et al.: *Validation of GEANT4 Monte Carlo models with a highly granular scintillator-steel hadron calorimeter*, JINST 8 P07005 (2013)
- [50] J. Apostolakis et al.: *GEANT4 Physics Lists for HEP*, IEEE Nucl. Sci. Symp., Dresden 2008, pages 833 - 836

- [51] H.Fesefeldt: *The Simulation of Hadronic Showers -Physics and Applications-*, Report Aachen PITHA 85/02 (February 1985)
- [52] B. Bilki et al.: *Pion and proton showers in the CALICE scintillator-steel analogue hadron calorimeter*, JINST 10 P04014 (2015)
- [53] B. Bilki et al.: *Measurement of the rate capability of Resistive Plate Chambers*, JINST 4 P06003 (2009)
- [54] The CALICE Collaboration: *CALICE DHCAL Noise Analysis*, CALICE Analysis Note CAN-031, March 2011
- [55] H. Ikeda et al.: *A detailed test of the CsI(Tl) calorimeter for BELLE with photon beams of energy between 20-MeV and 5.4-GeV*, NIM A441 (2000), p. 401 (Belle Collaboration)
- [56] The CALICE Collaboration: *Analogue, Digital and Semi-Digital Energy Reconstruction in the CALICE AHCAL*, CALICE Analysis Note CAN-049, May 2014
- [57] C. Neubüser: PhD thesis in progress, University of Hamburg
- [58] B. Bilki, B. Freund et al.: *DHCAL with Minimal Absorber: Measurements with Pions* (paper in preparation)
- [59] The CALICE Collaboration: *Parametrisation of hadron shower profiles in the CALICE Sc-Fe AHCAL*, CALICE Analysis Note CAN-048, April 2014

Acronyms

AHCAL Analogue Hadron CALorimeter. 30

ASIC Application-Specific Integrated Circuit. 34, 41, 87

ATLAS A Toroidal LHC ApparatuS. 4, 10

CALICE CALorimeter for LInear Collider Experiment. ii, iii, 1, 2, 29, 30, 56

CMS Compact Muon Solenoid. 4, 10, 11, 14, 27

DAQ Data Acquisition System. 34, 36

DCAL Digital CALorimetry chip. 34, 99

DHCAL Digital Hadron CALorimeter. ii, iii, 1, 2, 31, 33, 34, 35, 36, 56, 62, 63, 66, 70, 72, 74, 101, 102

ECAL Electromagnetic CALorimeter. 14, 15, 26, 27, 29

Fe-DHCAL DHCAL with steel absorber. 62, 63, 66, 68, 89

FEB Front-end Electronic Boards. 34

FTBF Fermilab Test Beam Facility. 34, 36, 37, 57

HCAL Hadronic CALorimeter. 14, 15, 26, 27, 29, 30

ILC International Linear Collider. ii, iii, 1, 8, 9, 10, 11, 12, 26, 27, 29

ILD International Large Detector. 14, 15, 29

LEP Large Electron-Positron Collider. 3

LHC Large Hadron Collider. 3, 10, 12

LINAC A linear accelerator. 8, 9

MAPS Monolithic Active Pixel Sensors. 30

MICROMEGAS Micro-MEsh Gaseous Structure. 31

Min-DHCAL DHCAL with Minimal absorber. vi, 34, 35, 36, 39, 41, 49, 54, 55, 57, 68, 72, 80, 89

MIP Minimum Ionising Particle. 17, 49, 63, 87, 88, 94

PFA Particle Flow Algorithm. 11, 14, 26, 27, 29

PID Particle IDentification. 39, 43, 62

PMT Photomultiplier Tubes. 30

RPC Resistive Plate Chamber. 25, 31, 33, 34, 36, 40, 49, 50, 51, 52, 54, 57, 60, 80, 99, 101

ScECAL Scintillator strip Electromagnetic CALorimeter. 30

SDHCAL Semi Digital CALorimeter. 31

SiD Silicon Detector. 12, 14, 29

SiPM Silicon Photomultiplier. 30, 31

SiW ECAL Silicon Tungsten Electromagnetic CALorimeter. 29, 30

SM Standard Model of particle physics. 1, 3, 4, 5, 6

TPC Time Projection Chamber. 14, 15